

The state of carbon and the piezoresistive effect in silicon oxycarbide ceramics

A dissertation approved by the Department of Materials and Earth Sciences in fulfilment of the requirements for the degree of Doctor-Ingenieur (Dr.-Ing.)

Dipl.-Ing. Felix Rosenberg

Born on 02.07.1984 in Mainz, Germany
01.06.2018 – Darmstadt – D-17

First assessor: Prof. Dr. Dr. h.c. Ralf Riedel

Second assessor: Prof. Dr.-Ing Roland Werthschützky



TECHNISCHE
UNIVERSITÄT
DARMSTADT



The state of carbon and the piezoresistive effect in silicon oxycarbide ceramics

Genehmigte Dissertation von Dipl.-Ing. Felix Rosenberg geb. Roth aus Mainz

Fachbereich Material- und Geowissenschaften, Technische Universität Darmstadt

Jahr der Veröffentlichung der Dissertation auf Tprints: 2018

1. Gutachter: Prof. Dr. Dr. h. c. Ralf Riedel

2. Gutachter: Prof. Dr.-Ing. Roland Werthschützky

Tag der Einreichung: 13.10.2017

Tag der Prüfung: 08.03.2018

Darmstadt D-17

URN: urn:nbn:de:tuda-tprints-75175

Veröffentlicht unter CC BY-SA 4.0 International
<https://creativecommons.org/licenses/>



Declaration of Authorship

I hereby declare that the thesis submitted is my own unaided work. All direct or indirect sources used are acknowledged as references.

I am aware that the thesis in digital form can be examined for the use of unauthorized aid and in order to determine whether the thesis as a whole or parts incorporated in it may be deemed as plagiarism. For the comparison of my work with existing sources I agree that it shall be entered in a database where it shall also remain after examination, to enable comparison with future theses submitted. Further rights of reproduction and usage, however, are not granted here.

This thesis was not previously presented to another examination board and has not been published.

Ehrenwörtliche Erklärung

Ich erkläre hiermit ehrenwörtlich, dass ich die vorliegende Arbeit selbständig angefertigt habe. Die aus fremden Quellen direkt und indirekt übernommenen Gedanken sind als solche kenntlich gemacht.

Ich weiß, dass die Arbeit in digitalisierter Form daraufhin überprüft werden kann, ob unerlaubte Hilfsmittel verwendet wurden und ob es sich – insgesamt oder in Teilen – um ein Plagiat handelt. Zum Vergleich meiner Arbeit mit existierenden Quellen darf sie in eine Datenbank eingestellt werden und nach der Überprüfung zum Vergleich mit künftig eingehenden Arbeiten dort verbleiben. Weitere Vervielfältigungs- und Verwertungsrechte werden dadurch nicht eingeräumt.

Die Arbeit wurde weder einer anderen Prüfungsbehörde vorgelegt noch veröffentlicht.

Darmstadt, den 1. Juni 2018

(Felix Rosenberg)

One of the greatest tragedies in life is the murder of a beautiful theory by a gang of brutal facts.

A cursive signature of Benjamin Franklin, written in black ink. The signature is fluid and elegant, with a prominent 'B' and 'F'.

Benjamin Franklin

Results from the present work were partly disseminated in the following journals:

- [1] **F. Rosenberg**, E. Ionescu, N. Nicoloso, R. Riedel, High-temperature Raman spectroscopy of nano-crystalline carbon in silicon oxycarbide, *Materials*, **2018**, 11, 93. DOI: 10.3390/ma11010093
- [2] L. Tang, **F. Rosenberg**, N. Nicoloso, R. Werthschützky, Dehnungsmessung an piezoresistiver polymerabgeleiteter Keramik, *tm – Technisches Messen*, **2017**, 84, 93-97. DOI: 10.1515/teme-2017-0044
- [3] **F. Roth**, P. Waleska, C. Hess, E. Ionescu, N. Nicoloso, UV Raman spectroscopy of segregated carbon in silicon oxycarbides, *J. Ceram. Soc. Japan*, **2016**, 124, 1042-1045. DOI: 10.2109/jcersj2.16100
- [4] **F. Roth**, C. Schmerbauch, E. Ionescu, N. Nicoloso, O. Guillon, R. Riedel, High-temperature piezoresistive C/SiOC sensors, *J. Sens. Sens. Syst.*, **2015**, 4, 133-136. DOI: 10.5194/jsss-4-133-2015
- [5] **F. Roth**, C. Schmerbauch, E. Ionescu, N. Nicoloso, O. Guillon, R. Riedel, Piezoresistive Ceramics for High-Temperature Force and Pressure Sensing, *Sensor und Messsystem 2014*, Beiträge der 17. ITG/GMA Fachtagung Nürnberg. (*ITG-Fachbericht 250*), Düsseldorf: VDE-Verl. 2014, ISBN 978-3-8007-3622-5

Other publications:

- [6] C. Stabler, **F. Roth**, M. Narisawa, D. Schliephake, M. Heilmaier, S. Lauterbach, H.-J. Kleebe, R. Riedel, E. Ionescu, High-temperature creep behaviour of a SIOC glass ceramic free of segregated carbon, *J. Eur. Ceram. Soc.*, **2016**, 36, 3747-3753. DOI: 10.1016/j.jeurceramsoc.2016.04.015
 - [7] S. Vowinkel, C. G. Schäfer, G. Cherkashinin, C. Fasel, **F. Roth**, N. Liu, C. Dietz, E. Ionescu and M. Gallei, 3D-ordered carbon materials by melt-shear organization for tailor-made hybrid core-shell polymer particle architectures, *J. Mater. Chem. C.*, **2016**, 4, 3976-3986. DOI: 10.1039/C5TC03483C
 - [8] C. Rüttiger, V. Pfeifer, V. Rittscher, D. Stock, D. Scheid, S. Vowinkel, **F. Roth**, H. Didzoleit, B. Stühn, J. Elbert, E. Ionescu and M. Gallei, One for all: Cobalt-Containing Polymethacrylates for Magnetic Ceramics, Block Copolymerization, Unexpected Electrochemistry, and Stimuli-Responsiveness, *Polym. Chem.*, **2016**, 7, 1129-1137. DOI: 10.1039/C5PY01845E
-

Table of Content

TABLE OF CONTENT	I
ABSTRACT	III
ZUSAMMENFASSUNG	V
1 MOTIVATION AND AIM OF THE STUDY	1
2 STATE OF THE ART AND BASICS OF PIEZORESISTIVE CERAMICS	3
2.1 POLYMER DERIVED CERAMICS.....	3
2.1.1 The SiOC/C system	4
2.1.2 The microstructure of SiOC/C.....	6
2.1.3 Percolation within SiOC/C.	7
2.2 ELECTRICAL CONDUCTIVITY IN SiOC/C	10
2.2.1 The allotropes of carbon and their unique electrical properties	10
2.2.2 Electrical conductivity in semiconductive carbon structures.....	14
2.2.3 Graphitization of carbon.....	18
2.3 THE PIEZORESISTIVE EFFECT	19
2.3.1 Piezoresistivity in crystalline semiconductors	20
2.3.2 Piezoresistivity in carbon	22
2.3.3 Piezoresistive carbon-containing inorganic nanocomposites	23
3 EXPERIMENTAL PROCEDURE	29
3.1 SAMPLE PREPARATION	29
3.2 MATERIALS CHARACTERIZATION	31
3.2.1 Elemental analysis	31
3.2.2 Density and porosity measurements	32
3.2.3 Raman spectroscopy	32
3.2.4 Thermogravimetric analysis.....	33
3.2.5 X-ray diffraction	33
3.2.6 X-ray photoelectron spectroscopy	34
3.2.7 Scanning Electron Microscope	34
3.3 ELECTRICAL INVESTIGATIONS	34
3.3.1 Electrical contacting of the samples	34
3.3.2 Temperature dependent impedance spectroscopy.....	35
3.3.3 Piezoresistive measuring chamber	35
3.3.4 High-temperature piezoresistive setup	36
3.3.5 Hall measurements.....	37
4 RESULTS AND DISCUSSION	38

4.1	STRUCTURAL CHARACTERIZATION AND THERMAL STABILITY OF SiOC/C	38
4.1.1	Phase composition.....	38
4.1.2	Densification process	42
4.1.3	Crystallization and bonding situation.....	44
4.1.4	Impact of oxidation on the electrical conductivity	49
4.1.5	Summary.....	50
4.2	RAMAN SCATTERING IN CARBON MATERIALS	51
4.2.1	Monitoring the graphitization process in SiOC/C.....	53
4.2.2	Characterization of the segregated carbon phase by Vis Raman	57
4.2.3	Summary.....	63
4.3	ELECTRICAL PROPERTIES OF SiOC/C.....	64
4.3.1	Resistance change with graphitization.....	65
4.3.2	Percolation in SiOC/C.....	65
4.3.3	Conduction mechanism in SiOC/C	68
4.3.4	Hall measurements of SiOC/C.....	72
4.3.5	Summary.....	74
4.4	THE PIEZORESISTIVE EFFECT IN SiOC/C	75
4.4.1	Effect of carbon concentration on the piezoresistive behavior.....	77
4.4.2	Effect of temperature on the piezoresistive behavior	82
4.4.3	Origin of the piezoresistive effect in SiOC/C	85
4.4.4	Comment on giant gauge factors in PDCs reported in literature	85
4.4.5	Development and application of a SiOC/C based prototype	87
4.4.6	Summary.....	90
5	CONCLUSION & OUTLOOK	91
6	REFERENCES	93
	ACKNOWLEDGMENT	101
	LIST OF ABBREVIATIONS.....	102
	LIST OF SYMBOLS.....	104
	LIST OF FIGURES	106
	LIST OF TABLES.....	108
	CURRICULUM VITAE	109

Abstract

The present work reports on the morphology of carbon, the electrical properties and the piezoresistive effect in polymer-derived silicon oxycarbides (SiOC/C nanocomposites) within carbon concentrations of $1 < \phi_C < 45$ vol.%. The nanocomposites have been prepared by pyrolysis of poly-organosilicon precursors or preceramic polymers and a subsequent densification step using spark plasma sintering ($1000 < T < 1800$ °C; $P = 50$ MPa, Argon). The obtained samples are characterized by the means of spectroscopic (Raman, TGA-FTIR, XRD, XPS) and electrical (dc conductivity, impedance, Hall effect) investigations. The SiOC/C composites consist of a glassy matrix (silica, $\text{SiO}_x\text{C}_{4-x}$), silicon carbide and segregated carbon and is simplified as a two phase system (glass/carbon) for the description of the electrical and piezoresistive properties. The state of carbon within SiOC/C depends on the carbon content of the precursor and the thermal treatment. According to UV Raman the microstructure of carbon changes from a disordered (amorphous) to nano-crystalline state within $1000 < T < 1800$ °C. The progressive ordering or graphitization, respectively, is illustrated by the increasing lateral crystal size ($7.5 < L_a < 20$ nm) and the corresponding decrease of the density of defects as derived from the intensity ratio A_D/A_G of the Raman D- and G-band. Vacancies have been identified as main type of defects.

The electrical and piezoresistive properties of SiOC/C mainly depend on the state of carbon with the exception of samples with very low carbon content ($\phi_C < 1$ vol.%). For samples treated at $T = 1600$ °C the resistivity decreases by several orders of magnitude at a critical carbon concentration of about 6 vol.%. For samples treated at 1400 and 1100 °C the percolation threshold shifts from 8 to 20 vol.% of carbon because of the lower degree of graphitization. Beyond the percolation threshold weakly activated transport ($E_a < 0.1$ eV) occurs in conjugated sp^2 bonds within a continuous 3D network. The charge carrier mobility ($\mu \approx 3$ cm²/Vs) and density ($N = 10^{18} - 10^{20}$ cm⁻³) of carriers are comparable to those of glassy carbon. A change from band-like transport to conduction in localized states at the percolation threshold is indicated by an increase in $E_a \approx 0.3$ eV and presumably arises from electron/hole confinement when the localization length approaches a lateral crystal size of $L_a \lesssim 10$ nm (L_a decreases from about 8 to 4 nm within $1 < \phi_C < 10$ vol.% carbon).

SiOC/C changes its resistivity with strain and, accordingly, the piezoresistive effect also relies on the carbon content and its degree of graphitization. Within $1 < \phi_C < 6$ vol.% the gauge factor (GF) increases up to the percolation threshold ($GF \approx 45$) and appears to arise from charge carrier tunneling. The extremely high GF values (> 1000) at the percolation threshold suggest either divergence of the GF vs. carbon concentration function or local strain concentration with

ϵ_{local} deviating from ϵ_{bulk} by an enhancement factor. Above the percolation threshold GF is related to the density of defects within the continuous carbon network. A strain-induced increase of the density of states near E_F is identified as origin of the piezoresistive effect, a change in mobility is unable to explain the experimental decrease of the resistance with applied strain.

The obtain results on the piezoresistivity favor the development of high-temperature strain sensors able to detect static and dynamic excitation. As a proof of concept a demonstrator to sense the natural frequency of a planetary gear has been developed.

Zusammenfassung

Die vorliegende Arbeit widmet sich der Beschreibung der Mikrostruktur des Kohlenstoffs, den elektrischen Eigenschaften und dem piezoresistivem Verhalten von Polymer-abgeleiteten Siliciumoxycarbid (SiOC/C) Nanokompositen mit einer Kohlenstoffkonzentration im Bereich von $1 < \phi_C < 45$ vol.%. Die Nanokomposite werden mittels direkter Polymer-zu-Keramik Umwandlung synthetisiert wobei poly-organosilikone und präkeramische Polymere zunächst pyrolysiert und anschließend verdichtet werden (Spark Plasma Sintering, $1000 < T < 1800$ °C; $P = 50$ MPa, Argon). Mit Hilfe spektroskopischer (Raman, TGA-FTIR, XRD, XPS) und elektrischer (Gleichstromwiderstand, Impedanz, Hall Effekt) Untersuchungen werden die jeweiligen Proben charakterisiert. Die Proben setzen sich aus einer glasartigen Matrix (Silica, $\text{SiO}_x\text{C}_{4-x}$), Siliciumcarbid und einer segregierten Kohlenstoffphase zusammen und werden, um die elektrischen und piezoresistiven Eigenschaften zu beschreiben, nährungsweise als ein Zweikomponentensystem (Glass/Kohlenstoff) betrachtet. Der Zustand des Kohlenstoffs in SiOC/C hängt von dem Kohlenstoffanteil des verwendeten Präkursors und der thermischen Behandlung ab. Wie die UV Raman-Untersuchungen belegen, wandelt sich die Kohlenstoffphase von einem ungeordneten (amorphen) in einen nanokristallinen Zustand innerhalb des Temperaturbereichs $1000 < T < 1800$ °C um. Die fortschreitende Ordnung oder Graphitisierung wird durch die zunehmende laterale Kristallitgröße ($7.5 < L_a < 20$ nm) und der damit zusammenhängenden Abnahme der Defektdichte, welche aus dem A_D/A_G Verhältnis der Raman D- und G-Banden abgeleitet werden kann, verdeutlicht. Leerstellen innerhalb der Kohlenstoffphase werden als wesentliche Art der Defekte identifiziert.

Im Gegensatz zu Proben mit sehr geringem Kohlenstoffanteil ($\phi_C < 1$ vol.%) werden die elektrischen und piezoresistiven Eigenschaften von SiOC/C hauptsächlich von dem Zustand des Kohlenstoffs bestimmt. Für Proben hergestellt bei $T = 1600$ °C nimmt der elektrische Widerstand um mehrere Größenordnungen ab, wenn der Kohlenstoffanteil die kritische Konzentration von 6 vol.% überschreitet. Proben, die hingegen bei 1000 oder 1400 °C synthetisiert wurden, besitzen eine deutlich höhere Perkolationsgrenze von 20 und 8 vol.%, da die Kohlenstoffphase schwächer graphitisiert vorliegt. Oberhalb der Perkolationsgrenze wird der schwach aktivierte ($E_a < 0.1$ eV) elektrische Transport durch konjugierter sp^2 -Bindungen innerhalb des durchgängigen dreidimensionalen Kohlenstoffnetzwerk realisiert. Die Ladungsträgermobilität ($\mu \approx 3$ cm²/Vs) und Dichte der Ladungsträger ($N = 10^{18} - 10^{20}$ cm⁻³) entspricht der von glasartigen Kohlenstoff. An der Perkolationsgrenze wechselt der elektrische Leitungsmechanismus von einem bandähnlichem Transport zu einem Transport innerhalb lokalisierter Zuständen, was durch ein Anstieg in der Aktivierungsenergie ($E_a \approx 0.3$ eV)

verdeutlicht wird. Dies resultiert wahrscheinlich aus einer Elektronen/Locheinschränkung sobald sich die Lokalisierungslänge, der Kristallitgröße von $L_a \lesssim 10$ nm nähert (L_a sinkt im Bereich von $1 < \phi_c < 10$ vol.% Kohlenstoff von 8 auf 4 nm).

SiOC/C verändert unter Druck seinen elektrischen Widerstand, weshalb der piezoresistive Effekt folglich mit dem Anteil an Kohlenstoff und dessen Graphitisierungszustand zusammenhängt. Innerhalb $1 < \phi_c < 10$ vol.% Kohlenstoff steigt der *gauge Faktor* (GF) bis zur Perkulationsgrenze ($GF \approx 45$) und scheint mit Tunnelprozessen der Ladungsträger verbunden zu sein. Extrem hohe GF Werte (> 1000) an der Perkulationsgrenze suggerieren entweder eine Divergenz der GF -Funktion, oder erhöhte lokale Belastung ϵ_{local} , welche um einen Verstärkungsfaktor von der Belastung innerhalb des Probe ϵ_{bulk} abweichen. Oberhalb der Perkulationsgrenze hängt GF von der Defektdichte innerhalb des durchgehenden Kohlenstoffnetzwerkes ab. Eine durch Belastung induzierte erhöhte Zustandsdichte nahe E_F wurde als Ursache für das piezoresistive Verhalten ermittelt, welches durch eine Änderung der Ladungsträgermobilität nicht erklärt werden kann.

Ausgehend von den piezoresistiven Ergebnissen lässt sich ein hochoberflächentemporalstabiler Drucksensor entwickeln, welcher sowohl statisch als auch dynamisch Anregungen detektieren kann. Auf Basis der ermittelten Ergebnisse wurde ein Prototyp entwickelt, welcher die Eigenfrequenz eines Planetengetriebes detektiert.

1 Motivation and aim of the study

A clean and efficient combustion process is especially nowadays, in view of the climate change, the key to reduce fossil fuel consumption and CO₂ emission. While low-carbon fuels or the deployment of hybrid and electric vehicles present viable alternatives, the majority of propulsion systems operating today still use conventional fuels associated with the internal combustion engine. Hence, the understanding of the physical and chemical basics of the combustion process is fundamental to achieving improvements in fuel efficiency, reducing greenhouse gas emissions and moreover allows for intelligent propulsion system design and enhancement of system maintenance and safety. In order to achieve insights into the combustion process innovative high-temperature stable sensor materials are required as the sensor needs to be located as close as possible to the desired measurand for accurate monitoring. However, conventional microelectromechanical systems (MEMS) are not capable of operating under these harsh conditions and thus need to be located outside the combustion chamber. The limitation of non-direct sensing induces inaccuracy and underlines the critical need of high-temperature sensing technology in nearly all industrial sectors such as automotive, aerospace and energy industry.

The most common sensing techniques considered in high-temperature applications are: capacitive, piezoelectric and piezoresistive. Capacitive sensors usually consist of two separated plates whose distance changes upon the applied stress leading to a change in capacitance. This kind of sensor is known to exhibit a low thermal shift, a high resolution and a low background noise. Yet they suffer from limited robustness and are easily disturbed by parasitic capacitance with magnitudes similar to that of the sensor signal. Piezoelectric sensors have been intensively studied in the recent years. Due to their crystalline structure most of the materials only possess piezoelectric behavior along one certain crystal plane. In case of polycrystalline material they need to be post treated in an electric field to induce polarisation. Furthermore, phase transition and oxygen diffusion often lead to a low quality signal limiting the sensing performance to temperatures below $T < 400$ °C.

Piezoresistive sensors utilize the change in electrical resistivity upon mechanical strain and have the advantage to provide accurate dynamic and static measurements. Metallic strain gauges and semiconductive materials (Si, Ge) are generally used in commercially available piezoresistive sensors but often suffer from a high fragility and rigidity. Therefore, polymer-based composites filled with conductive particles appear preferable for a broader range of applications. In particular carbon nanotubes (CNTs) polymer composites are already broadly

used as mechanical strain sensors. However, due to their polymeric nature, the application temperature is limited and the composites often suffer from agglomeration.

Within this work, polymer-derived ceramics (PDCs) are introduced to eliminate the problems of agglomeration and temperature limitation as they are known to withstand harsh environments. Previous work revealed that PDCs exhibit promising piezoresistive behavior which makes them an auspicious future candidate material in sensor technology under harsh conditions. No-post treatment is necessary for the piezoresistive behavior to occur, as it solely relies on the homogeneous *in-situ* segregation of carbon during the polymer-to-ceramic transformation. To date, only a few scientific publications deal with the piezoresistive effect and the electrical properties of PDCs.

The present thesis provides a comprehensive study of the microstructural and electrical properties of polyorganosiloxane derived silicon oxycarbide ceramics (SiOC/C) to prove their deployment as prospective piezoresistive sensor materials. The changes of the electrical properties are investigated as a function of synthesis temperature and varying carbon concentrations. Aim of the study is to present a comprehensive description of the piezoresistive effect in SiOC/C nanocomposites and to demonstrate their application as strain sensors under static and dynamic conditions at room and elevated temperatures.

2 State of the art and basics of piezoresistive ceramics

The first section of this chapter delivers a brief introduction into the SiOC/C system and its microstructure. In the following, their electrical properties and the different conduction mechanisms of various carbon allotropes will be discussed in detail. Finally, an insight into the basic principles of the piezoresistive effect and the current research on piezoresistive, inorganic carbon-composites will be provided.

2.1 Polymer derived ceramics

In 1956, Fritz and Raabe discovered that monomeric organosilicon compounds ($\text{Si}(\text{CH}_3)_4$ and $\text{Si}(\text{C}_2\text{H}_5)_4$) can be thermally transformed into a SiC ceramic at much lower temperatures as compared to the traditional synthesis methods [1]. A few years later, in the early 1960 Ainger and Herbert [2] as well as Chantrell and Popper [3] reported on the thermal conversion of polyphosphazene $((\text{NPCl}_2)_n)$ into a P_3N_5 ceramic. The first technical approach was defined by Verbeek, Winter and Mansmann [4-6] almost ten years later, as they described the production of small-diameter $\text{Si}_3\text{N}_4/\text{SiC}$ fibers upon thermolysis of organosilicon polymers. A significant breakthrough was achieved at the end of the 1970s, when Yajima *et al.* developed a method to fabricate SiC based fibers [7-9]. These initial discoveries and the first successful technical approach promoted the growing interest for this novel synthesis route and led to further developments of new precursors and improved processing techniques. The era between 1950 and 1980 can be marked as the origin of a novel class of ceramic materials, the so-called polymer-derived ceramics (PDCs).

Especially, polysiloxane, polysilazan and polycarbosilane have proven to be the most important preceramic polymers. Figure 2.1 displays the Si-based preceramic polymers and their thermal conversion to their correlating ceramic microstructure.

The final ceramic composition is mainly determined by the chemistry and structure of the preceramic polymer. Accordingly, different ceramic systems such as binary SiC and Si_3N_4 or ternary SiOC and SiCN systems can be achieved depending on the chemical element (X = Si, C, N, O) are bonded to the backbone of the starting polymer. It is important to note that the latter systems cannot be synthesised by traditional processing methods, due to the low solubility of carbon in SiO_2 and Si_3N_4 . In addition, the family of ternary systems can easily be extended to a broad variety of quaternary and even multi-nary ceramics by a simple chemical modification of the preceramic polymer with elements such as: Al, B, Hf, Zr or Ti [10-18].

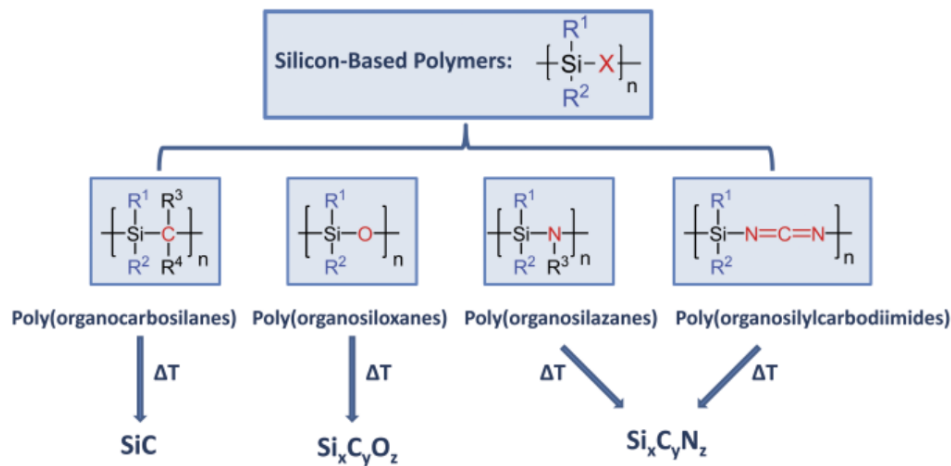


Figure 2.1: Simplified structure of silicon based polymer. By substituting the polymeric backbone atom X with C, O or N different types of ceramics structures can be achieved upon pyrolysis [19].

Not only does the chemistry of preceramic polymer correlate with the resulting ceramic microstructure, it also allows to tailor the properties of the starting polymer like rheology, solubility and decomposition. A broad variety of designed ceramics can be processed or shaped using established forming techniques in plastic industry such as polymer infiltration, injection molding, coating from solvent, extrusion or resin transfer molding [19]. In addition, no sintering additives or agents have to be used during the polymer-to-ceramic process which further facilitates their application.

2.1.1 The SiOC/C system

A silicon oxycarbide compound (SiOC) prepared at $T < 1000\text{ }^\circ\text{C}$ is a covalent network of silicon tetrahedra bonded to carbon and oxygen atoms. Their chemical structure can be derived from silica glass in which part of the oxygen atoms are replaced by carbon atoms solely bonded to silicon. Besides the amorphous network, generally described by $\text{SiO}_{4-x}\text{C}_x$ ($x = 1 - 4$), a fine dispersed carbon phase (“segregated carbon”) might be present, depending on the carbon content of the initial precursor. The so-called “carbon rich” silicon oxycarbides (SiOC/C) therefore inhibit two types of carbon atoms: sp^3 hybridized carbon within the amorphous matrix and sp^2 -type segregated carbon. A schematic depiction of the silicon oxycarbide structure is given in Figure 2.2. As a result of the incorporation of carbon, $\text{C}(\text{Si})_4$ units are locally formed, which strengthens the network and thus enhance several material properties like viscosity, glass-transition temperature and Young’s modulus [20, 21].

One of the first attempts to incorporate carbon into glass was investigated by Ellis in 1951 in order to lower the electrical resistance of silica [22]. In 1968 Smith and Crandall reported on the increasing resistance of devitrification and higher viscosity when a mixture of carbonwax and colloidal silica was hot-pressed at $T = 1000 - 1150\text{ }^\circ\text{C}$ under $P = 138\text{ bar}$ [23].

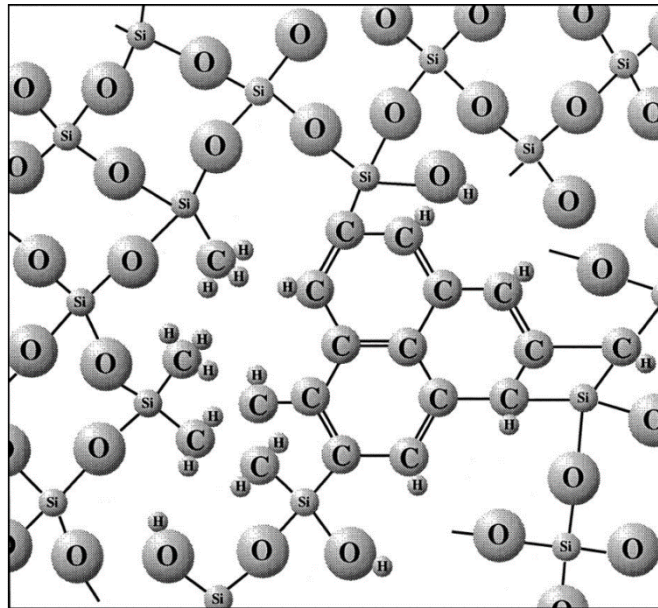


Figure 2.2: Schematic depiction of an amorphous SiOC/C network heat treated at $T < 1000\text{ }^{\circ}\text{C}$ [24].

Eller and Meiser proposed that the incorporated carbon acts as an excellent dehydroxylating agent, removing the silanol groups of the glass which, if left in the structure, soften the final glass [25]. In view of all these studies, none of them could confirm the substitution of carbon into the silica network when separated sources of silica and carbon are used. One of the first evidences of a ternary Si-O-C phase was announced by Pampuch *et al.* in a study investigating the oxidation behavior of SiC in 1980 [26]. Their assumption was later confirmed by the intensive research on the oxidation stability of polymer-derived ceramic SiC fibers (NiCALON) by Lipowitz as well as Port and Sartre [27-29].

As it appears to be challenging to substitute oxygen with carbon within a SiO_2 network, most SiOC glasses reported in the literature are synthesised by the sol-gel process or from polysiloxanes. Hereby the siloxane precursor are prepared through hydrolysis and condensation reactions of silicon alkoxides $\text{R}_x\text{-Si(OR)}_x$ already providing the desired Si-C bonds which are preserved during the subsequent thermal conversion.



Through the substituent R of the silicon alkoxide different functional groups (hydrogen, alkanes, alkenes) can easily be introduced to control e.g. the amount of segregated and network carbon, or the cross-linking process. The latter process plays an important role in the organic to inorganic conversion as it can reduce the thermally induced release of hydrocarbons and prevent fragmentation of the precursor. Hence, a high branching level acquires an enhanced thermal stability and a higher ceramic yield in the subsequent ceramization process of the cross-linked precursor.

2.1.2 The microstructure of SiOC/C

Upon thermal treatment at temperatures below $T < 1000\text{ }^{\circ}\text{C}$, an amorphous structure of two interwoven networks emerge: the amorphous SiOC phase which consists of mixed silicon tetrahedral units and the *in-situ* generated “segregated” carbon phase. Saha. *et al.* proposed a microstructural model where silica-rich nanodomains in the size of 1 – 3 nm are embedded into a percolative network of graphene-like sheets [30]. The interdomain boundaries between both phases are connected through mixed $\text{SiO}_x\text{C}_{4-x}$ tetrahedral units like SiC_3O , SiC_2O_2 and SiCO_3 . A more recent topological model proposes a spatial segregation of the structural $\text{SiO}_x\text{C}_{4-x}$ -units into oxygen-rich and the carbon-rich $\text{SiC}_x\text{O}_{4-x}$ units [31]. This assumption relies on the observation that the concentrations of SiO_4 and SiC_4 units are significantly higher than those expected from a statistical distribution of Si-O and Si-C bonds in SiOC. The oxygen-rich structural units are supposed to constitute the interior backbone of the amorphous ceramic while the carbon-rich units occupy the interface between the ceramic backbone and the segregated carbon phase. Both structural models are depicted in Figure 2.3.

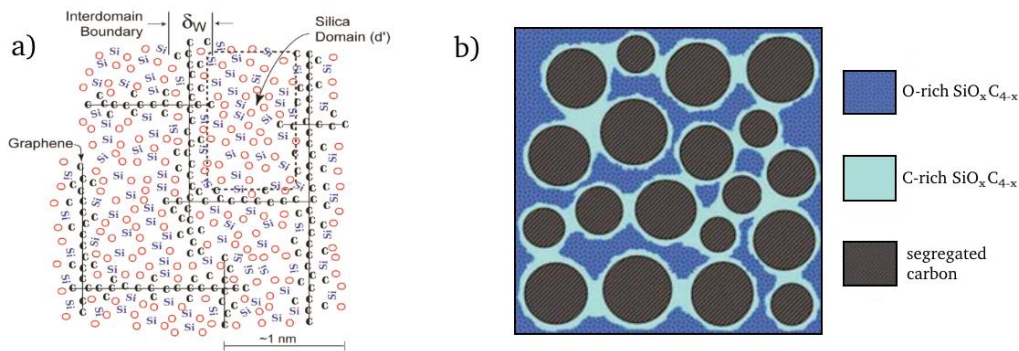
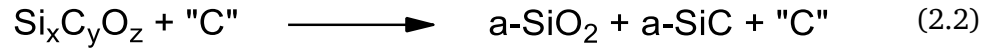


Figure 2.3: Two proposed models of the nanostructure in polymer-derived SiOC. a) Silica nanodomains are warped by layers of graphene [32]. b) O_2 -rich SiOC domains form a continuous network and encapsulate the precipitated carbon [33].

Upon further annealing $T > 1300\text{ }^{\circ}\text{C}$, the SiOC network demixes forming nanodomains of amorphous silica and silicon carbide. Due to the fact that the silica domains are amorphous and do not tend to crystallize into cristoballite, even at high temperatures ($T > 1800\text{ }^{\circ}\text{C}$), the crystallization process of silica in SiOC/C is most probably suppressed. A low interfacial energy between SiC and SiO_2 and the presence of a finely dispersed carbon phase obstructing long-range diffusion in silica were proposed as cause for the enhanced crystallization resistance [32].

However, the crystallization of SiOC into β -SiC seems not to be hindered and can occur by the following two reactions: (i) in the first process at temperatures above $T > 1300\text{ }^{\circ}\text{C}$ the amorphous SiOC separates into amorphous silica and silicon carbide which is then followed by crystallization of the latter. (ii) The second pathway appears only after the phase separation at temperatures above $T > 1500\text{ }^{\circ}\text{C}$ and includes the reduction of silica using carbon as reduction

agent. The nanometer sized β -SiC crystals were found to appear near carbon structures with an average crystal size less than 5 nm [34, 35]. Both reactions may appear in combination at sufficiently high temperatures.



Carbon is the third phase within SiOC/C and begins to segregate at temperatures as low as $T = 500 - 800 \text{ }^\circ\text{C}$. Nearly 70% of the initial carbon atoms present in the preceramic polymer participate in the formation [33]. According to Monthieux *et al.*, carbon starts to segregate as an amorphous mixture of various polycyclic aromatic hydrocarbons (PAHs) with lateral sizes of $L_a = 1 \text{ nm}$ [34]. Dehydrogenation and edge-to-edge linkage of neighbouring PAHs at $T \approx 1000 \text{ }^\circ\text{C}$ lead to the formation of larger graphitic clusters increasing the degree of order. Temperature treatment above $T \geq 1400 \text{ }^\circ\text{C}$ further promotes the ordering process resulting in a carbon phase consisting of misaligned graphene sheets stacked in a turbostratic manner.

HR-TEM studies indicate that despite the high temperature treatment and the associated phase-separation process small amounts of mixed Si-O-C bonds may still exist at the interphase boundaries between silica and silicon carbide [36]. They are also expected at the boundary layer between the silica and carbon phase [37]. To summarize, the microstructure of phase-separated SiOC/C can be described as a nanocomposite of amorphous silica, dispersed turbostratic carbon and β -SiC precipitations.

2.1.3 Percolation within SiOC/C.

Bond percolation theory describes the evolution of interconnected clusters forming a continuous network according to the random principle. The theory did find its broadest application in material research as it can predict certain properties such as electrical resistivity, thermal conductivity and diffusion constants of heterogeneous materials depending on their constituents [38-41]. In the following, we focus on the description of the electrical conductivity in composite materials.

One of the first models to predict the electrical properties of a composite material was the so-called Bruggeman symmetric and asymmetric effect medium theory (EMT) in 1935 [42]. As the asymmetric approach does not allow percolation and is mostly used for dispersions (oil/water or foams), we will focus on the symmetric approach. In this approach, the entire composite consists of ellipsoids, which are assigned in a random order and to the volume fractions of the particular phases. The approximation of the resulting properties of the composite are then developed from averaging over all the ellipsoids. Thus, the EMT theory fails to precisely predict

the filler concentration at which the composite acquires electrical conductivity due to the fact that it is a volume-weighted model averaging the properties of the constituents and ignoring any fractal or long-range correlations. Therefore, the theory has only proven to fairly model electrical percolation in two dimensions [43].

As the insulator-conductor transition does not behave linearly near the percolation threshold, a more precise phenomenological description of the change in electrical conductivity has to be formulated, namely the percolation theory (PT) [39]. Consider fillers with high electrical conductivity added continuously to an insulating matrix. The insulator-conductor transition is then described by the evolution of a continuous pathway throughout the matrix as the filler concentration ϕ_c approaches a critical volume $\phi_{cri.}$ also called percolation threshold. At the threshold, the first percolating path is formed throughout the insulating matrix resulting in an abrupt increase in the electrical conductivity. The overall conductivity of the composite near the percolation threshold can be expressed according to

$$\sigma_c = \sigma_0 \cdot (\phi - \phi_{cri.})^t \quad (2.4)$$

where σ_0 is a proportionality constant, σ_c the conductivity of the composite, $\phi_{cri.}$ the critical concentration below the composite is insulating (percolation threshold) and t the critical exponent. The value of the critical exponent t is known to depend on the lattice dimensionality and was calculated to be $t \approx 2.0$ in a three-dimensional lattice [44, 45]. Derivation from this behavior have been reported for many different composites [46]. According to Balberg this derivation can be assigned to a tunnelling-percolation processes with strong fluctuations in tunnelling distances causing high values even up to $t = 6.0$ [47, 48].

The electrical conductivity of a SiOC/C nanocomposite is determined by the volume fraction and morphology of its carbon segregations. In order to consider the influence of these two factors, Cordelair *et al.* simulated the insulator-conductor transition of SiOC/C by using the general effective media theory (GEM). The GEM combines most aspects of the EMT and PT theory and thus allows to assess the influence of the amount and the different graphitization states of the carbon phase as depicted in Figure 2.4. Following the proposed model by Cordelair *et al.*, the conductivity in SiOC/C can be divided into two regions: the tunnelling regime at low carbon concentrations and the percolation regime [49]. Below the percolation threshold the conductivity is driven by hopping and tunnelling processes between randomly distributed carbon segregations whereas above the percolation threshold a conductive pathway throughout the insulating matrix is present, entering the percolation regime. To account for the distinct carbon morphologies which depend on the applied pyrolysis temperatures, t was varied

between 2–4 and the percolation threshold was set from $\phi_{\text{cri.}} = 20\text{--}5\text{ vol.\%}$ carbon. Accordingly, at low pyrolysis temperatures ($T < 800\text{ }^\circ\text{C}$) a high amount of segregated carbon is necessary to build a conductive pathway due to the low aspect ratio of the presumably spherical-like carbon segregation. This was simulated by a high percolation threshold of $\phi_{\text{cri.}} = 20\text{ vol.\%}$ and a low critical exponent of $t = 2$. Increasing the pyrolysis temperature results in a growing aspect ratio of the carbon precipitations which is expressed by a decreasing percolation threshold $\phi_{\text{cri.}} = 5\text{ vol.\%}$ and an increasing critical exponent of $t = 4.0$. Therefore, the insulator-conductor transition is realized at much lower carbon concentrations for samples pyrolyzed at higher temperatures. Additionally, the authors observed that with increasing aspect ratio the abrupt rise in conductivity at the percolation threshold appeared to be less intense and that the overall conductivity of the SiOC/C material below the percolation threshold was enhanced. Thus, the resulting conductivity and the percolation threshold respectively, can be adjusted by choosing different pyrolysis temperatures as the aspect ratio of the carbon segregations is enhanced.

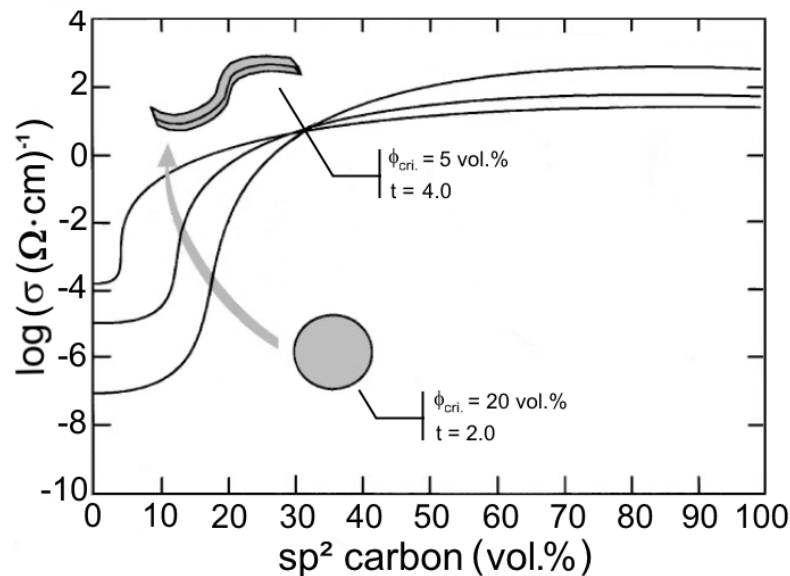


Figure 2.4: Calculated insulator-conductor transition for different values of t and $\phi_{\text{cri.}}$ [49].

A precise prediction of the electrical conductivity of a SiOC/C system is rather challenging as reliable information about its carbon morphology and aspect ratio are difficult to acquire. Besides, the closer the SiOC/C system is to the percolation threshold the stronger the conductivity is influenced by small concentration variations. Therefore, we concentrated on carbon-rich SiOC/C systems ($\phi_{\text{C}} > 10\text{ vol.\%}$) just above the percolation threshold to minimize the influence of the process parameter and to increase their reproducibility.

2.2 Electrical conductivity in SiOC/C

The overall conductivity of PDCs is mainly determined by the concentration and graphitization state of the segregated carbon phase which enables to specifically tailor their electrical behavior. A recently reported SiOC/C ceramic [50] with a high carbon content ($\phi_c \approx 30$ vol.%) showed a resistivity value of $\rho = 0.35 \Omega/\text{m}$ at RT which further decreased to $\rho = 0.14 \Omega/\text{m}$ upon annealing (note that graphite has a resistivity of $\rho \leq 10^{-3} \Omega/\text{m}$). These values are significantly lower than those usually reported for SiOC with a carbon content $\phi_c < 7.5$ vol.% ($\rho = 10^7 - 10^{10} \Omega/\text{m}$) [49]. The change in resistivity is attributed to the higher amount of segregated carbon. Besides the amount of segregated carbon, its degree of order is considered to significantly affect the electrical conductivity as all experimental studies show an increase of conductivity with increasing pyrolysis temperature [51-53] or increasing graphitization, respectively. In the following we will consider the different allotropes of carbon and their change in microstructure and conductivity respectively upon graphitization, as the carbon phase possess the most prominent influence on the electrical conductivity in SiOC/C.

2.2.1 The allotropes of carbon and their unique electrical properties

Elemental carbon is well known to possess a broad variety of allotropes with different electrical, thermal and mechanical properties. Depending on the structure and its hybridization state, the electrical conductivity can vary between a strong insulator (diamond) and a highly conductive material (graphite). This emphasizes the strong correlation between the microstructure and electrical conductivity in carbon materials.

Besides the crystalline structures, various types of disordered carbons such as turbostratic carbon, glassy carbon or diamond-like-carbon (DLC) and their hydrogenated analogous exist. Their properties can be assigned according to the following principles: (i) the ratio of sp^2 and sp^3 sites, (ii) the local arrangement and (iii) the concentration of the hydrogen atoms. A schematic representation of selected carbonaceous allotropes is given in Figure 2.5. Note that the amount of sp^2 carbon and the electrical behavior are broad estimations, as they strongly depend on the synthesis method and the applied heat-treatment.

Graphite consists of solely sp^2 hybridized carbon layers stacked in a hexagonal ABA order. The carbon layers (graphene) are weakly bounded together by Van-der Waals forces produced by the delocalized π -orbitals of each sheet. The reason why elemental carbon favors the graphitic structure in contrast to other group IV elements, which prefer to coordinate along the diamond lattice, is its electronic state and the fact that all first row elements lack of p-like core electrons. This results in tightly contracted p-orbitals, enhancing the covalent sigma bonds of the sp^2 carbon. Therefore, the bonds along the basal plane are extremely stiff and strong, whereas the

bonds between the planes are weak. As a result, graphite can easily be sheared and cleaved in plane. Based on the anisotropic structure of graphite with its delocalized π electrons between the layers, an electrical conductivity of $\sigma = 3 \cdot 10^4 (\Omega \cdot \text{cm})^{-1}$ has been measured along the planes. If the temperature raises, thermal scattering processes decrease the conductivity indicating metallic conduction.

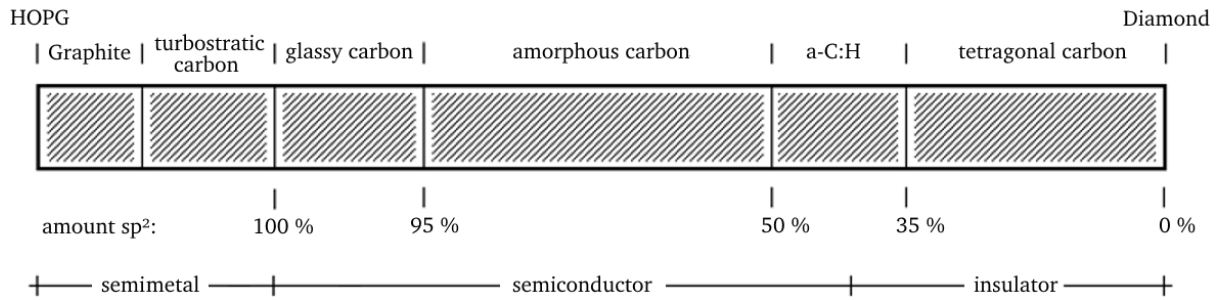


Figure 2.5: Schematic depiction of the carbon allotropes hierarchy and their corresponding conductive class.

The overlap between the valence- and the lowest conducting band is about 36 meV, making graphite a semi-metallic conductor [54, 55]. In contrast, the conductivity perpendicular to the sheets is about four magnitudes lower with values in the range of $\sigma = 1 - 5 (\Omega \cdot \text{cm})^{-1}$. With increasing temperature, the conductivity increases, because the temperature enables the electrons to jump or tunnel between the sheets. For this process an activation energy of $E_a = 0.65 \text{ eV}$ has been calculated [55]. A highly ordered form of graphite is the synthetic "highly oriented pyrolytic graphite" (HOPG) consisting of very well aligned long-ranged crystallites making it a highly conductive carbon material with $\sigma = 2.1 \cdot 10^8 (\Omega \cdot \text{cm})^{-1}$ along and $\sigma = 5 \cdot 10^4 (\Omega \cdot \text{cm})^{-1}$ perpendicular to the plane.

The conductivity of graphitic materials is sensitive to any kind of defects such as sp^3 bonding, vacancies or dislocations like tilt boundaries. With increasing disorder, the crystalline domains decrease in size and their parallel alignment gets more and more distorted. Therefore, in less perfect graphitic material the layer planes are randomly rotated with respect to each other and the interplanar spacing I_c is found to be significantly larger than $I_c > 0.344 \text{ nm}$. Such graphitic structures are termed turbostratic and can be regarded as a semi-crystalline structures with an interplanar spacing of $I_c = 0.350 - 0.380 \text{ nm}$ [56]. Likewise, glassy carbon, also sometimes labeled as vitreous carbon, can be considered as semi-graphitic. Both materials are categorized in terms of their mean lateral cluster size L_a and their mean coherence length of graphene stacks I_c perpendicular to L_a . One refers to turbostratic carbon when the lateral crystal size L_a is rather large ($L_a > 200 \text{ \AA}$) and the graphene sheets are only horizontally rotated, whereas in glassy carbon the crystalline domains are in the range of $L_a \approx 15 - 50 \text{ \AA}$ and the crystalline domains are randomly oriented and tangled in a complicated manner, see Figure 2.6. It is interesting to note,

that glassy carbon does not tend to graphitize even upon further heat treatment. This suggests a very stable structure of entangled sp^2 ribbons which are assumed to be interconnected by tetrahedral carbon atoms at the interface between neighboring crystallites [57-59]. The linkage also prevents the development of parallel stacked sheets, as the C-C bonds have to be broken to produce extensive areas of graphite sheets.

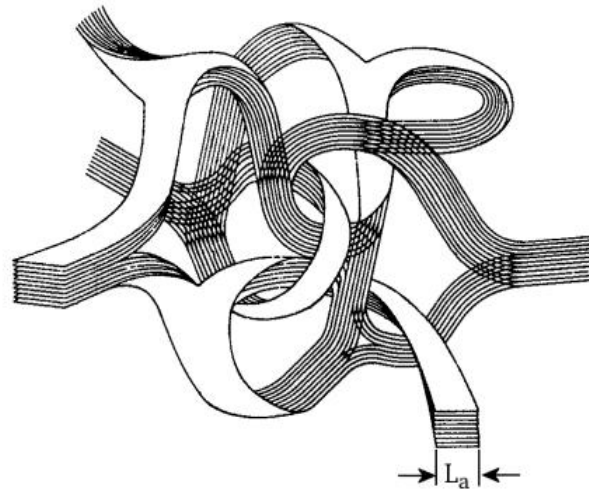


Figure 2.6: Schematic structural model of glassy carbon by Jenkins and Kawamura [59].

Compared to glassy carbon which appears to be quasi-crystalline on a 5 \AA scale and distorted on a long scale ($> 50 \text{ \AA}$), amorphous carbon (a-C) is of true amorphous nature. It is composed of 50 - 95 % of sp^2 carbon and obtains small graphitic clusters with $L_a = 15 - 20 \text{ \AA}$. Through higher fraction of sp^3 carbon and its higher covalence, a-C has a higher density but much lower conductivity compared to glassy carbon. Several structural models have been developed to describe its microstructure [60-62]. It is commonly accepted that the sp^2 sites are clustered within graphitic islands of 34 - 60 fused sixfold rings, and that those islands are interconnected by an insulating sp^3 matrix [63, 64]. Robertson *et al.* suggested that all π -bonds are confined within the graphitic islands instead of percolating throughout the sample like in glassy carbon. This results in randomly oriented islands with localized π -bonds, embedded in an insulating sp^3 matrix. The resulting semiconductive behavior of a-C is primarily determined by the number and size of sp^2 islands present in the material and depends critically on the method of preparation. For example, an a-C deposited by CVD consists of up to 90 - 99% of sp^2 sites with an conductivity of $\sigma = 10^3 (\Omega \cdot \text{cm})^{-1}$ and a band gap of $E_g \approx 0.4 \text{ eV}$, whereas a Ion-beam deposited a-C results in a much higher proportion of sp^3 sites giving a much lower conductivity of $\sigma = 10^{-2} (\Omega \cdot \text{cm})^{-1}$ and a band gap of $E_g \approx 3 \text{ eV}$.

Hydrogenated amorphous carbon (a-C:H) can be considered as the hydrogenated analogous of amorphous carbon. Despite its high hydrogen content of 30 – 60 at.% and the fact that hydrogenation promotes sp^3 bonding, a surprisingly large fractions of sp^2 carbon remains in the

material. The band gap of a-C:H lies in the range of $E_g = 1.7 - 2$ eV when 30 - 50% sp^2 -sites are present [65]. The sp^2 sites are considered to be small aromatic clusters in the size of 1 - 4 fused sixfold rings similar to polycyclic aromatic hydrocarbon structures (PAHs) [64]. Their peripheral carbon atoms tend to be saturated with hydrogen which prevents the formation of high molecular sp^2 clusters. Annealing up to $T = 400 - 600$ °C results in the loss of hydrogen and gradually transforms a-C:H into a-C. Increasing the hydrogen content, regarding the fact that hydrogen bonds to sp^2 and sp^3 sites with a similar probability,[66] results in a gradually declining of the conductivity towards an insulating behavior.

Tetragonal carbon (ta-C) is a non-hydrogenous, amorphous carbon material with a small amount of sp^2 sites (less than 10%) [67, 68]. Its microstructure can be described as a network of amorphous sp^3 carbon interconnected by domains of disordered diamond. The network of these strong sp^3 bonds gives ta-C physical and mechanical properties that are to a certain extent similar to diamond. For instance, ta-C is often used as coating to reduce the abrasive wear on tooling components or as an anti-corrosion coating [69]. As it still obtains small fractions of sp^2 and/or hydrogen, its mechanical properties are somewhat poorer compared to diamond. Consequently, hydrogenated tetragonal carbon (ta-C:H) containing significant amounts of H ($\approx 10\%$) has a lower chemical and thermal stability and also a lower hardness compared to the hydrogen-free ta-C [69]. The electrical conductivity of ta-C lies in the range of $\sigma = 10^{-7} - 10^{-15} (\Omega \cdot \text{cm})^{-1}$ with band gaps around $E_g = 1 - 3.5$ eV which depends on the local configuration of the sp^2 sites rather than simply on the $sp^2:sp^3$ fraction. Compared to a-C in which small polycyclic aromatic hydrocarbons (PAHs) are embedded in a sp^3 matrix, only small C=C sp^2 chains are assumed to be present in ta-C. This is supported by molecular dynamics simulation which indicate that the sp^2 sites are unlikely to cluster in ta-C [67, 70].

Diamond is one of the crystalline allotropes of carbon and is known to be the hardest natural mineral. It can be formed out of graphite under high compression ($P > 15$ GPa) and temperatures ($T > 1500$ °C). The main difference between diamond and graphite is that ideal diamond solely consists of sp^3 - bonded carbon atoms whereas graphite is only composed of sp^2 carbon. Ideal diamond shows an insulating behavior with $\sigma = 10^{-18} (\Omega \cdot \text{cm})^{-1}$ and a high band gap of $E_g = 5.5$ eV. The band gap barely decreases upon heating ($T = 700$ K) which results from the low intrinsic charge carrier concentration of $N = 10^{-23} \text{ cm}^{-3}$ [71]. However, in nanocrystalline diamond the conductivity remarkably increases up to $\sigma = 10^{-6} (\Omega \cdot \text{cm})^{-1}$ as thin graphite layers are expected to be present at the interface between two adjacent nanoparticles. These carbons create energy levels within the band gap of diamond which increases the hopping conductivity near the Fermi level. Table 2.5 delivers a brief overview of the considered carbon allotropes.

Table 2.1: Comparison of the RT conductivity, the band gap, the lateral crystal size L_a and the interplane distance of the different carbon allotropes.

	$\sigma_{RT} (\Omega \cdot \text{cm})^{-1}$	E_g (eV)	L_a (Å)	I_c (Å)	Ref.
crystalline					
HOPG	$3.5 \cdot 10^5$	0	$> 10^3$	3.35	[72]
Graphite	$2.5 \cdot 10^4$	0	$> 10^3$	3.35	[63, 73]
Diamond	$10^{-16} - 10^{-18}$	5.5	-	-	[69, 74]
semi-crystalline					
turbostratic carbon	$2.5 \cdot 10^4$	0	< 100	3.44	[75]
glassy carbon	$10^2 - 10^3$	$\approx 10^{-2}$	15 - 50	3.75	[59, 76, 77]
non-crystalline					
amorphous carbon	$10^{-1} - 10^{-3}$	0.4 - 0.7	10 - 20	> 3.75	[64, 78]
hydro. amorphous carbon	10^{-3}	1.5 - 2.8	≈ 5	-	[79-81]
tetragonal carbon	$10^{-7} - 10^{-15}$	3.0 - 3.5	-	-	[67]

2.2.2 Electrical conductivity in semiconductive carbon structures

The electrical conduction is one key property to define and classify solid materials. According to their conductive behavior, materials are classified into metals, semimetals, semiconductors and insulators. Under the assumptions of (i) an infinite-size system, (ii) a homogenous system and (iii) non-interactivity of the charge carriers, the band theory can successfully predict and explain the electronic behavior of each material. The theory implies that with increasing the numbers of atoms, the electron levels move close together and form a continuum of energy state. This continuum is often referred to as band. As the electronic system of the material seek to minimize its total energy, the bands are "filled up" starting from the lowest energy states. The hypothetical energy level of an electron state with a 50% probability of being occupied is called the Fermi level (E_F). Hence, the energetic location of E_F allows to classify the material according to the conduction classes mentioned above.

In metals, E_F is located within the overlapping valence- and conduction band. Thus, the energy states in the overlap are only half filled which allows the electrons to jump between temporary occupied states. This creates a delocalized electronic state with a high mobility for electrons, which is typical for metals. In case of semi-metallic materials, the overlap between the valence- and the conduction band is small, resulting in a negligible density of states near E_F . Contrary to metals, in which the only present charge carrier are electrons, the conduction in semimetals is realized by electrons and holes.

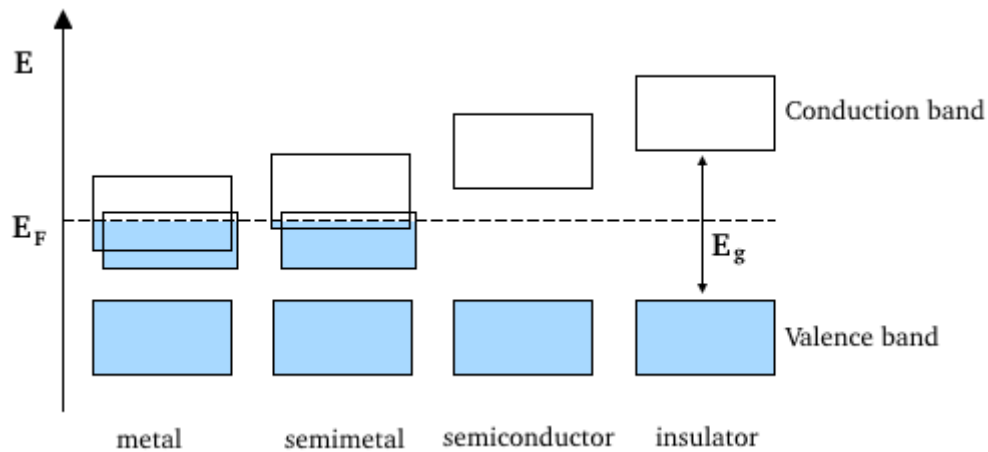


Figure 2.7: Schematic depiction of the band structure going from metals to insulators [82].

Similar conduction occurs in semiconductors and insulators, which are characterized by an energy gap E_g between the valence- and conduction band. By definition, a semiconductor holds a band gap of $E_g \leq 4$ eV whereas an insulator possess a band gap of $E_g \geq 4$ eV. Thermal excitation allows the electrons to jump into the unoccupied conduction band, creating an equivalent amount of holes in the valence band which also contribute to the overall conductivity. By introducing impurities into the crystalline semiconductor- or insulator-lattice, the activation energy E_a for the electronic transport can be drastically lowered. The dopant introduces a defect or disorder into the crystalline lattice which creates an energy state near the valence band (p-doped) or conduction band (n-doped). Thus, the activation energy is much smaller.

The band theory was established to interpret charge carrier transport in crystalline solids and does not directly explain conduction in disordered systems. Nevertheless, the basic concept of the theory can still be applied to describe the semimetal to insulator transition in carbon materials. Through the introduction of stacking disorder well-aligned semi-metallic graphite is gradually transformed into turbostratic carbon with a small band gap of $E_g \approx 0.1$ eV. If the crystallites are further reduced in size and randomly oriented, a narrow band gap semiconductor with localized states results. The principal of localized states was first proposed by Anderson who showed that in a disordered system the probability of electron diffusion over a certain distance drops to zero with the increase of the distance [83]. According to Mott, the formation of localized states is caused by configurational disorder in the amorphous network and may lead to the formation of tail states above and below the extended bands [84]. Two models have been widely used to interpret the electronic properties of amorphous solids: the Cohen-Fritzsche-Ovshinsky (CFO) [85] and the Davis-Mott (DM) model [86].

The DM-model proposes the existence of a localized band near the Fermi level. This midgap-state originate from deviations of the ideal amorphous structure such as dangling bonds and vacancies. The resulting gap between the two extended states E_v and E_c is defined as pseudo or

mobility gap. At the border of the mobility gap, the transition from extended to localized states produces a drop in mobility called mobility edge. The energy states described by the CFO model are depicted in Figure 2.8. In this model Cohen *et al.* assume that the localized tails are only weakly declining towards the midgap. This leads to an overlap of the conduction and valence-band tail leaving a significant density of states at the midgap. The real band structure of an amorphous semiconductor depends on the amount and nature of the present defects and lies somewhere between these two models. A schematic depiction of the models is given in the Figure 2.8.

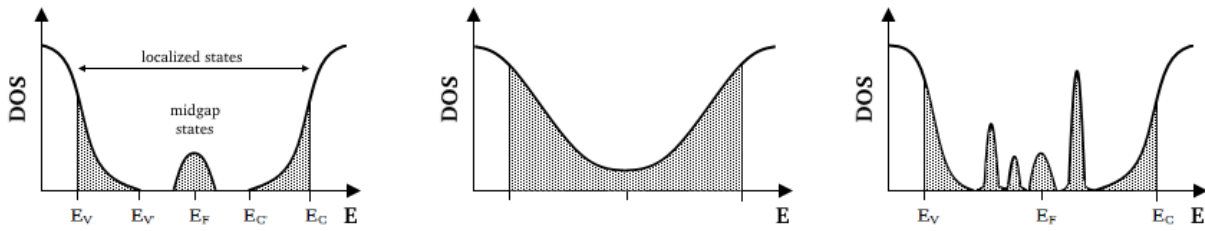


Figure 2.8: DM-Model, CFO-Model and a possible structure of an amorphous system.

Within the model of Davis and Mott, three different conduction mechanisms may occur in amorphous semiconductors: (i) conduction in localized states near the Fermi level E_F , (ii) conduction in band tails and (iii) conduction in extended, delocalized states. At lower temperatures, only the localized states near the Fermi level are occupied. The thermal energy is not sufficiently high enough to allow the charge carrier to jump into the conduction band or its tail states. Because the electronic states are localized within the mobility gap the transport of charge requires a conduction mechanism through the localized states. The mechanism in this area is known as hopping conduction and is observed in two well-known varieties, i.e. nearest neighbor hopping (NNH) and variable-range hopping (VRH). The first mechanism shows a temperature dependency which follows the law of Arrhenius and is given by the following equation:

$$\sigma \propto e^{-\frac{\Delta W}{k_b T}} \quad (2.5)$$

The necessary activation energy ΔW is delivered by the lattice vibration (phonons). As the temperature is lowered below $T < 4.2$ K, the conduction mechanism changes and the charge carrier now prefer to tunnel to sites that are further away but closer in energy, instead of hopping to the nearest neighbor. The conductivity in this temperature region follows:

$$\sigma \propto e^{-\left(\frac{T_0}{T}\right)^{1/4}} \quad (2.6)$$

and was first observed by Mott [87]. The phenomenon is called variable-range hopping (VRH) and shows the empirically found temperature-dependency of $\log \sigma \approx T^{-1/4}$. The mobility of the charge carrier in the localized states is about three orders of magnitude smaller compared to the mobility in the extended states. The theory predicts that the dominance of VRH is always observed in the localized states of semiconductors at temperatures below $T < 4.2$ K. However, the typical $T^{-1/4}$ dependency was also observed for several semiconductors even at RT. In case of an amorphous SiCN system, even at temperatures as high as $T = 800$ °C. It is important to note that a $\log \sigma \approx T^{-1/4}$ dependency does not necessarily imply a VRH-conduction, as calculations of other conduction mechanism also have shown a dependence similar to $T^{-1/4}$.

With increasing temperature, the charge carriers are able to jump from the localized state into the band tails of the conduction band and the valence band, respectively. If the conduction in the band tails is realized by thermally activated hopping of electrons, the conduction is given by:

$$\sigma \propto \left(\frac{k_b T}{\Delta E} \right)^S \cdot e^{\frac{-(E_C - E_F + \Delta W)}{k_b T}} \quad (2.7)$$

If holes are considered as charge carriers the exponent changes to $\frac{-(E_F - E_V + \Delta W)}{k_b T}$, where accordingly ΔW is the activation energy for hopping, ΔE is the width of the respective band tail and the exponent S describes the energy dependency of the density of states in the band tail. At higher temperatures conductivity is realized by electrons thermally raised into the conduction band. The extended states within the conduction band are characterized by a high mobility ($\mu_c = 10^2 - 10^3$ cm²/Vs) which decreases sharply at the mobility gap. The thermal dependency of the conductivity in the extended state is given by:

$$\sigma = e N_{(E_C)} k_b T \mu_c \quad (2.8)$$

with $N(E_c)$ being the density of states at the mobility edge E_c and its mobility μ_c . However, the high defect concentration in amorphous semiconductors is responsible for the relapse of the electrons back into the localized states which drastically reduces the charge carrier mobility below $\mu_c < 10$ cm²/Vs [88]. The localized states have to be distinguished from dopant states, as they lie deeper in the gap which is why they do not release their charge carrier as easy as the dopant states do.

2.2.3 Graphitization of carbon

With increasing thermal treatment graphitization of the carbons starts to take place and the semiconductive material is progressively transformed into a material with metallic behavior. At $T \approx 1000\text{ }^\circ\text{C}$, the basic structure units (BSU) with a length of $L_a \approx 10\text{ \AA}$ start to pile up and form distorted columnar structures. The hydrogen atoms at the crystallite periphery are released, which further promotes in-plane growth of adjacent BSUs. At $T > 1700\text{ }^\circ\text{C}$ the columnar structures disappear and wrinkled layers are formed, which rapidly increase in L_a and I_c minimizing E_g . Above $T > 2100\text{ }^\circ\text{C}$ most of the in-plane defects have been eliminated and stiff and straight carbon layers have emerged resulting in an overlap of valence and conduction band.

The process of graphitization is emphasized by the theoretical work of Coulson *et al.* who investigated the evolution of the energy states of varying hexagonal arrays of aromatic molecules. According to their calculations, the valence and conduction band begin to approach each other when the number of carbon atoms increases. At about ≈ 50 carbon atoms, the upper and lower band come into contact resembling the behavior of a semi-metallic material such as graphene [89].

With the development of structural order, the lateral crystal size L_a increases and the charge carrier mobility is changed. Nevertheless, a broad statistic distribution of varying crystallite sizes with boundaries and different orientation remains in non-graphitic carbons, which results in a narrow band gap semiconductor, depicted in Figure 2.9. According to Mrozowski, the electronic transport in graphitic-like materials is realized by "intrinsic" as well as "excess" charge carriers [90, 91]. The term "intrinsic" describes π -electrons in the upper π -band and holes in the lower π -band. Consequently, there exists an energy gap between those two bands, which is large for small aromatic clusters, almost in the same range as that of diamond ($E_g \approx 5\text{ eV}$), but gradually drops to $E_g = 0.03\text{ eV}$ as the size of the aromatic planes increases. The "excess" carriers are represented by holes which emerge as a result of the presence of π -electron trapping states. When electrons are trapped out of the valence band, the E_F will be depressed enabling a positive hole conduction mechanism even at low temperature [90]. With parallel alignment of the planes and elimination of the remaining in-plane defects, the number of carriers start to refill the valence band, causing the E_F to rise again. The gap finally vanishes or may even lead to an overlap when the crystallite size reaches about $L_a = 1000\text{ \AA}$. The overlap in highly ordered pyrolytic graphite was found to be dependent on the layer-stacking scheme or the layer order [92]. Hereby, a great number of electrons can easily be raised into the conduction band allowing them to move freely. Cyclotron-resonance experiments suggest that graphite possess

approximately equal concentrations of electron and hole density and a comparable mobility in the range of $\mu = 1.5 - 2 \cdot 10^4 \text{ cm}^2/\text{Vs}$ [93].

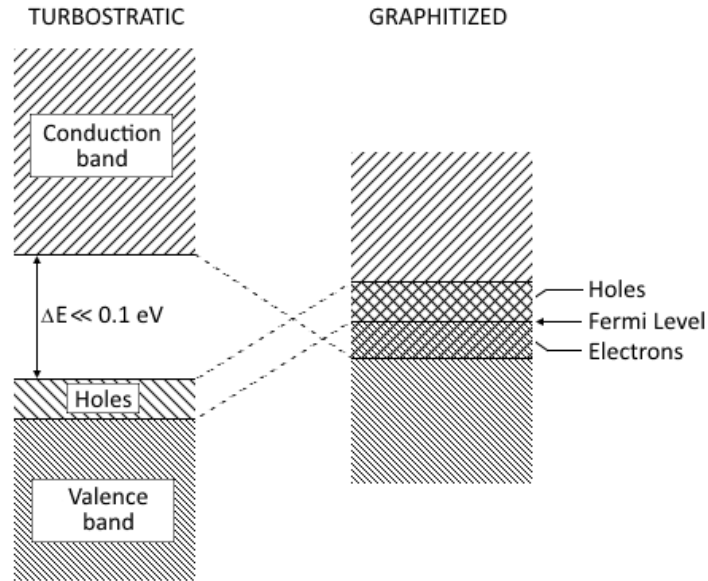


Figure 2.9: Schematic energy-band diagram for turbostratic and graphitic carbon [90].

2.3 The piezoresistive effect

The term piezoresistivity defined as the change in the resistance of a material with applied stress, was introduced by Cookson [94] in 1935 and first patents concerning piezoresistive metal-foil strain gauges were granted in 1952 [95, 96]. A few years earlier Bardeen and Shockley described the piezoresistive effect in single-crystalline semiconductors [97]. The predicted high piezoresistive shear coefficients in doped silicon and germanium were confirmed by Smith [98] and the first silicon-based strain gauge was reported by Mason and Thurston in 1957 [99]. A few years later piezoresistive sensors became market-ready.

Within a basic description of the piezoelectric effect (PZR), the initial bulk resistance R_0 of a material with the dimensions $l_0 \times w_0 \times h_0$ and the electrical resistivity ρ_0 is given by

$$R_0 = \rho_0 \frac{l_0}{w_0 \cdot h_0} \quad (2.9)$$

and changes upon applying an external load

$$\frac{\Delta R}{R_0} = \left(\frac{\Delta l}{l_0} - \frac{\Delta w}{w_0} - \frac{\Delta h}{h_0} \right) + \left(\frac{\Delta \rho}{\rho_0} \right) \quad (2.10)$$

Accordingly, two contributions to the PZR can be identified: The first is a pure geometrical effect, while the second one describes the material-specific piezoresistive response. Considering an isotropic material obeying Hooke's law, the change in the resistivity can be written as

$$\frac{\Delta R}{R_0} = (1 + 2\nu)\varepsilon + \left(\frac{\Delta\rho}{\rho_0}\right) \quad (2.11)$$

with the Poisson's ratio ν and the strain ε . The gauge factor (GF), which describes the fractional change of the resistance with the applied strain, then reads

$$GF = \frac{\Delta R/R_0}{\varepsilon} = (1 + 2\nu) + \frac{\Delta\rho}{\varepsilon \cdot \rho_0} \quad (2.12)$$

and defines the sensitivity of strain sensors.

Most of the metals own a small PZR with GF -values of about 2, as the change in their resistance is mainly determined by geometrical effects. In the case of semiconducting materials, the PZR originates from the change of the band structure with applied stress or changes of the charge carrier mobility or density, respectively. Thus, semiconducting piezoresistive materials exhibit significantly higher gauge factors as compared to their metallic counterparts.

2.3.1 Piezoresistivity in crystalline semiconductors

At the time of Smiths discovery of large piezoresistive effects in semiconductors (Si, Ge) most of the existing theories were based on stress induced shifts in bandgap energies. Later in 1950s, Bardeen and Shockley presented a more precise theory to describe the piezoresistive effect based on changes in the charge carrier mobility which still serves as the basis for the more recently proposed models [97]. The theories for n-type semiconductors continue to be refined since the 1950s, while the piezoresistive effect in p-type semiconductors still have not been fully understood due to the complexity of the valence band structure. Therefore, only n-type semiconductors are considered in the following to describe the piezoresistive effect.

One of the most accepted theoretical model to describe the piezoresistive effect in n-type semiconductors is the Many-Valley-Model of Herring *et al.* [100]. Herein the electrons are located in three different conduction band minima along the orthogonal directions as depicted in Figure 2.10. The electrons occupy the minimum energy level of each valley along the centreline of a constant energy ellipsoid. When compressive uniaxial strain is applied along the [100] direction the ellipsoids are asymmetrically dilated or constricted resulting in an anisotropic change in the effective mass and mobility of the charge carrier proportional to the applied stress. Hence, the electrons from the perpendicular valley [010], [001] are transferred to the parallel valley [100] so that the density of states of the effective mass changes. With continuously increasing compressive strain more and more electrons are transferred into the parallel valley which is accompanied by a greater resistance along the [100] direction. This process continuous until all electrons are transferred. Therefore, the longitudinal piezoresistive

effect in n-type silicon is primarily caused by the change in the effective mass due to the reduced mobility of the conduction band electrons [101].

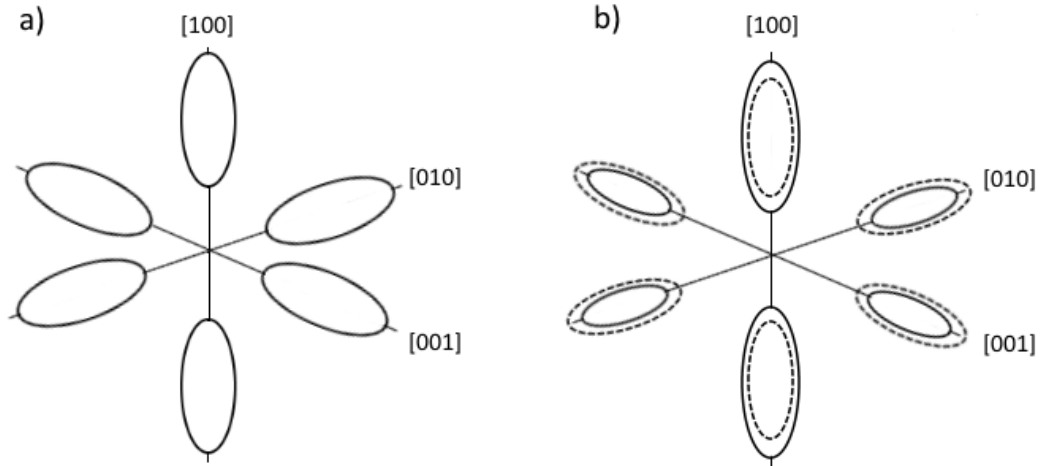


Figure 2.10: Constant energy surfaces in momentum space for n-doped silicon a) Surface of the six constant energy ellipsoids in the conduction band b) The effect of stress on the valley energy depicted by asymmetric dilation or constriction of the ellipsoids, respectively [102].

In order to describe the anisotropy of the PZR, the piezoresistive coefficients π_{ij} are introduced. The electric field vector \vec{E} and the current vector \vec{j} are linked by a 3-by-3 resistivity tensor (ρ). For Si, the resistivity tensor and the stress tensor can be summarized in a 6x6 matrix using the piezoresistive coefficients π_{ij} . Due to the cubic symmetry in crystalline silicon, the number of piezoresistive coefficients is further reduced to three independent coefficients: π_{11} , π_{12} , π_{44} .

$$\pi_{ij} = \begin{pmatrix} \pi_{11} & \pi_{12} & \pi_{12} & 0 & 0 & 0 \\ \pi_{12} & \pi_{11} & \pi_{12} & 0 & 0 & 0 \\ \pi_{12} & \pi_{12} & \pi_{11} & 0 & 0 & 0 \\ 0 & 0 & 0 & \pi_{44} & 0 & 0 \\ 0 & 0 & 0 & 0 & \pi_{44} & 0 \\ 0 & 0 & 0 & 0 & 0 & \pi_{44} \end{pmatrix} \quad (2.13)$$

The effective values for the longitudinal piezoresistive coefficient π_l and the transverse piezoresistive coefficient π_t can be calculated from the coefficients π_{ij} . As can be seen in Table 2.2, the piezoresistive coefficient π_{44} dominates in p-doped silicon whereas in n-doped silicon π_{44} can be neglected. For a detailed description of the piezoresistive effect in crystalline semiconductors the reader is referred to reference [103-105].

Table 2.2: Resistivity and piezoresistive coefficients for p- and n-doped Si and Ge [8].

Materials	ρ [$\Omega \cdot \text{cm}$]	π_{11} [10^{-31} Pa^{-1}]	π_{12} [10^{-31} Pa^{-1}]	π_{44} [10^{-31} Pa^{-1}]
Silicon				
n-type	11.7	-102.2	53.4	-13.6
p-type	7.8	6.6	-1.1	138.1
Germanium				
n-type	9.9	-4.7	-5.0	-137.9
p-type	15.0	10.6	5.0	46.5

2.3.2 Piezoresistivity in carbon

In the 1970s the piezoresistivity of carbon fibers has been intensively studied. Their behavior seems to be rather complex as they show both a positive as well as a negative dependency on the applied strain. Low modulus fibers ($E = 240 - 310 \text{ MPa}$) exhibit a linear positive piezoresistive behavior ($GF = 13.4$) whereas high modulus fibers ($E > 500 \text{ MPa}$) show a non-linear negative behavior ($GF = 3.4$) with the largest sensitivity found at low strains. A change in orientation, inter-particle contact and changes in carrier density have been proposed for the piezoresistive effect [89, 106]. Takezawa and Jenkins investigated the influence of heat treatment on the piezoresistive behavior of carbon rods derived from phenol resin. The materials heat treated at $T = 700 \text{ }^\circ\text{C}$ were extremely sensitive whereas the materials treated at $T = 1200 \text{ }^\circ\text{C}$ showed no sign of piezoresistivity. They postulated that the piezoresistivity is directly related to the intrinsic band gap of the semiconductive material [55].

Similar findings were reported on diamond-like carbon (DLC) films prepared by plasma-assisted chemical vapor deposition [107-109]. The authors assumed that the film consist of well-conducting sp^2 clusters embedded within an insulating sp^3 matrix and that the electrical conduction relies on hopping between adjacent sp^2 clusters [108]. Tensile or compressive strain causes the distance between the clusters to increase or decrease resulting in a change of the resistance. They observed that lower deposition voltages lead to a low sp^2/sp^3 -ratio with gauge factors values in the range of $GF = 51 - 58$, whereas for high deposition voltages a high sp^2/sp^3 ratio with gauge factor values between $GF = 16 - 36$ were observed. They conclude, that the piezoresistivity can be enhanced when the sp^2 clusters are small and the cluster distance is large.

In the last few years graphene (2D-crystalline carbon allotrope) has gained significant interest as a promising material in strain sensor applications, as it can sustain very high in-plane tensile strain (25 - 30 %) [110]. Various types of graphene based strain sensors have been developed based on CVD grown graphene. The highest sensitivity was achieved when graphene was

deposited on a Si_xN_y substrate. Extremely high gauge factor values in the range of $GF = 18000$ were obtained which were ascribed to the change in bond length and grain boundaries [111]. Lee *et al.* used a wafer size graphene prepared by CVD grown on Ni or Cu metal films, which was transferred onto arbitrary substrates to fabricate a strain sensor device with gauge factor values of $GF = 6.1$ [112]. Also Bae *et al.* transferred a CVD grown graphene film on to a flexible polydimethylsiloxane (PDMS) substrate and obtained gauge factor values in the range of $GF = 4 - 14$ when applying strains above 1.8% [113]. Huang *et al.* demonstrated that the resistance of a suspended single-layer graphene device showed only minor changes even when subjected to high deformation. A gauge factor value of $GF = 1.9$ was observed which is comparable to the gauge factor value of $GF = 2.4$ predicted by simulation [114]. They showed that the uniaxial strain is not capable of opening a band gap in graphene and therefore does not affect its carrier mobility. However, many other authors claim that the band gap of graphene opens under uniaxial strain, but theory suggests that a strain below 23 % should not be capable of doing so [115, 116].

Due to the fact, that ideal graphene shows a relatively weak electrical response upon structural deformation Zhao *et al.* deposited a film of nanographene using remote plasma enhanced chemical vapour deposition (RPECVD) whose inter domain distance is altered upon stretching or compressing strain [117]. The average distance between two nanographene domains was estimated to be $d = 3.4$ nm. By controlling the packing density and layer thickness the initial resistance of the film can be tuned. The different piezoresistance sensing mechanism allowed gauge factor values as high as $GF = 300$. As explanation for the high sensitivity, a charge tunneling mechanism within the conductive network of neighboring nanographene domains was proposed which is assumed to react very sensitive to the applied strain.

In summary, the piezoresistive effect in carbon materials strongly depends on the synthesis which affects the homogeneity and the degree of order of the carbon phase. Single layered graphene possess a low piezoresistive effect in the range of $GF = 1.9 - 2.5$. Through the introduction of disorder (point defects, grain boundaries) the piezoresistive response can be enhanced up to $GF = 300$. Many authors assume that primarily the change in hopping or tunneling distance between conductive domains is responsible for the change in electrical conduction and, consequently, the piezoresistive effect.

2.3.3 Piezoresistive carbon-containing inorganic nanocomposites

In the following, carbon-containing, piezoresistive composite materials with an insulating ceramic network are presented. Composites contain at least two different components and if one of them is nano-sized, here mainly the various forms of carbon, the composite is considered

as nanocomposite [118]. Depending on the content of carbon insulating, semiconducting or semimetallic compounds are obtained. As a general rule, the carbon is randomly distributed within the matrix and, unlike in crystalline matter, no directional contribution to the piezoresistive behavior has to be considered.

There are two methods to functionalize an insulating matrix with a conductive carbon phase. In the first method, carbon is mechanically mixed into the insulating material using dispersing agents to prevent agglomeration. Typical systems are alumina/carbon, magnesia /carbon and concrete/carbon, see below. The second method refers to the polymer-derived ceramic (PDC) route. Herein, the carbon phase is generated *in-situ* during the polymer to ceramic transformation. Typical examples of PDC-related nanocomposites are SiOC/C, SiCN/C and SiONC/C. PDCs combine many favourable properties like high-temperature stability, chemical inertness, high hardness and wear resistance and are therefore quite apt for strain/pressure sensors in harsh environment [119].

2.3.3.1 Piezoresistive effect in carbon-containing Al₂O₃/C and MgO/C

To date, very little research has been focused on the piezoresistive behavior of carbon-containing oxide ceramics. Recently, Waku *et al.* investigated the electrical properties of carbon functionalized alumina and magnesia composites under mechanical load [120, 121]. A gauge factor of $GF = 45$ is reported for the magnesia composite functionalized with graphite particles (5.0 wt.%) having an aspect ratio of ≈ 100 . Similar gauge factor values of $GF = 42$ have been obtained when graphite particles (3.5 wt.%) are added in the exact same manner to alumina. In both cases, the carbon content has been chosen close to the percolation threshold where the electrical conductivity changes by orders of magnitude due to formation of a first conductive pathway within the sample [122]. Since the percolation threshold does not only depend on the amount of conductive carbon particles but also on their geometrical shape, Kishimoto *et al.* further investigated the most favourable particle size ratio between the insulating and conductive component of the alumina carbon black composite system [123]. They suggested that the piezoresistive behavior is most strong near the percolation threshold.

Table 2.3 summarizes the few available data on the carbon reinforced ceramic composites Al₂O₃/C and MgO/C. At room temperature, gauge factor values no higher than $GF = 45$ are observed for carbon particles with an aspect ratio of about ≈ 100 occupying a volume fraction between $\phi_c = 5 - 11$ vol.%. Piezoresistive sensors with a sensitivity comparable to conventional Si sensors can be realized with this class of materials.

Table 2.3: Piezoresistive behavior of Al₂O₃ and MgO reinforced with carbon (at RT).

Matrix	Carbon filler	Aspect ratio	Threshold [vol.%]	GF-value
Al ₂ O ₃	graphite particles	≈ 100	5	42 ^a
	carbon black particles	< 100	11	18 ^a
MgO	graphite particles	≈ 100	6	45 ^a

^a = Calculated by the author using Young's modulus of the ceramics [124, 125].

2.3.3.2 Piezoresistive carbon-containing concrete nanocomposites

Carbon-containing concrete composites attracted high interest since 1990 as strain sensors [126]. Concrete is an inorganic composite mainly made of oxides and water. A commonly used material is Portland cement consisting of CaO (≈ 60 wt.%), SiO₂ (≈ 20 wt.%) and Al₂O₃ (≈ 6 wt.%) [127]. The electrical conductivity of concrete depends on its drying stage ranging from air-dried semiconducting to high-temperature-dried insulating concrete [128]. The electrical resistivity of concrete is decreased through the addition of semi-metallic carbon, enabling new functional features including sensing of strain and damage [129-131]. Especially, the ability to detect or prevent structural damage gained much interest as it is of crucial relevance for civil infrastructures [132]. Several studies have been reported on strain and damage sensing with carbon-fiber-reinforced cement composites, see e.g., Ref. [133-138]. In the following, the current status of concrete-based nanocomposites containing nano-sized carbon fillers such as carbon nano-fibers (CNFs) [139-142], carbon nanotubes (CNT) [143-148], carbon black (CB) [129, 149-151] and graphene nano-platelets (GNP) [152, 153] is summarized.

Carbon nano-fiber (CNF) reinforced cement composites

Galao *et al.* performed a systematic study on the sensing properties of CNF-reinforced cement nanocomposites [140]. Several variables like carbon concentration, thermal treatment, current density, loading rate or maximum applied stress were considered. The nanocomposites with the highest sensitivity had a CNF concentration of 2 wt.% and exhibited a gauge factor of $GF \approx 50$. Furthermore, it was shown that curing of the composite had a significant influence on the piezoresistive behavior suggesting that a prolonged curing time provides a more tight fiber-matrix interface, thereby enhancing the piezoresistive response [154]. In accordance with this view, Wen *et al.* considered an intimate contact between the cement matrix and the dispersed CNFs as origin of the piezoresistive behavior [155].

Carbon nanotubes (CNT) reinforced cement composites

The sensing properties of CNT-reinforced cement are known to improve upon oxidative treatment of the CNTs with H_2SO_4 or HNO_3 . Carboxylic acid groups formed on the CNT surface react with the calcium-silicate-hydrate (C-S-H) and/or $\text{Ca}(\text{OH})_2$ from the cement matrix, thereby introducing strong covalent bonds between the CNT and the matrix [147], i.e. chemical modification of the nanotubes allows for tuning of the interface between the CNTs and the cement matrix and thus to improve the piezoresistive response. Li *et al.* investigated the piezoresistive behavior of chemically treated and untreated CNT cement composites under cyclic compressive loading [144]. The untreated and treated CNT reinforced composites (both containing 0.5 wt.% CNTs) exhibited gauge factors values of $GF = 272$ and 371 , respectively. The authors claim that the number of contact points and the tunnel distance between the nanotubes are altered with increasing compressive stress inducing the change of the resistivity.

Graphene nanoplatelet (GNP) reinforced cement composites

A recently published work investigated graphene nanoplatelet-reinforced cement under compressive and tensile strain and reported GF values of about $GF = 100$ [152]. GNPs consist of stacks of graphene sheets exhibiting thicknesses $\ll 100$ nm and diameters of several μm , which results in large aspect ratios of the order of 10^3 (somewhat lower than that of CNTs). The GNP concentration necessary to provide a piezoresistive response was exceeding the percolation threshold of 10 wt.%. Below the percolation threshold, no correlation between resistivity and applied stress was found. Very large GF -values ($> 10^3$) were obtained upon applying low compressive stress. Reduction of the contact resistance within the interface between the GNPs and the cement matrix and closing of the distance between adjacent GNPs were held responsible for this result.

Carbon black (CB) reinforced cement nanocomposites

Carbon black particles are less effective in providing conducting cement composites, due to their low aspect ratio (< 100) [156]. However, CB particles are quite cheap and have therefore been used to lower costs, while the sensing properties are maintained [129, 157, 158]. Nanocomposites with 15 wt.% of CB have been shown to provide GF values of about $GF = 50$ under compressive stress. Even at markedly lower CB contents, far from the percolation threshold, unexpectedly high GF -values were obtained. Thus, a cement-based nanocomposite containing 0.5 wt.% CB still exhibited a gauge factor value of $GF = 14$.

Table 2.4 summarizes the impact of the different carbon fillers CB, CNFs, CNTs and GNPs on a common cement (Portland, Type I). All nanocomposites show enhanced gauge factors

($50 < GF < 350$) close to the respective percolation threshold. The data suggests that, the gauge factor scales with the aspect ratio of the carbon filler, since GF slightly increases by factor of about 6 with the aspect ratio.

Table 2.4: Piezoresistive behavior of carbon-reinforced cement composites at RT.

Matrix	Carbon filler	Aspect ratio	Threshold [vol.%]	GF -value
Portland cement (Type I)	carbon black particles	100	10	55
	graphene nanoplatelets	1000	2.4	100
	carbon nanofibers	< 2000	1.5	45
	carbon nanotubes	< 10000	0.5	360 ^a

^a = Values have been calculated assuming a Young's modulus of 30 GPa [159].

2.3.3.3 Piezoresistivity in PDCs

In 2008, Zhang *et al.* reported on the piezoresistive behavior of a SiCN/C-based material ($\phi_c = 12.6$ vol.%) pyrolyzed at $T = 1400$ °C. Unusually high gauge factors ranging from $GF = 1000$ to 4000 were found, being the highest values for any ceramic known so far [160, 161]. However, no clear explanation has been given yet for the extremely high sensitivity of SiCN/C. Two electrical transport mechanisms are considered to be of importance in SiCN/C: carbon controlled percolation in highly conducting SiCN/C and matrix controlled transport in low conductive samples [162]. The piezoresistivity of the SiCN/C is therefore believed to be solely determined by the tunnelling of electrons between the separated carbon precipitations who decrease in distance, during compression, leading to a significant conductivity enhancement. The authors found both reverse and logarithmic dependence with applied stress for SiCN/C prepared below $T < 1200$ °C, whereas the SiCN/C samples synthesized at temperatures above $T > 1200$ °C showed only a logarithmic dependence [163]. Although intuitively convincing, the lack of experimental data on the tunnel distance and the barrier height as a function of the carbon concentration leaves the description of the PZR by a tunneling model only qualitative and needs further corroboration.

SiOC/C prepared from an poly(methylsilsesquioxane) at $T = 1400$ °C was also found to exhibit piezoresistive behavior ($GF \approx 145$) [164]. According to TEM analysis, turbostratic carbon and nano-domains of SiC form within remaining pores in the composite material. Therefore, the

observed piezoresistive behavior was assumed to rely on a tunnelling-percolative network of turbostratic carbon [165]. An overview of the published GF values are reported in the following Table 2.5.

Table 2.5: Piezoresistive behavior of polymer-derived-ceramics.

	Matrix [vol.%]	seg. carbon [vol.%]	GF-value
SiOC/C	92.5	7.5	145
SiOCN/C	91.5	8.5	600 - 1700
SiCN/C	87.4	12.6	1000 - 4000

Only few data are available for the temperature dependence of the piezoresistive behavior in PDCs [166]. The high-temperature measurements revealed GF values between $GF = 600 - 1700$, strongly depending on the applied stress and temperature. Generally, the gauge factor decreases with temperature indicating an inverse relation with the sample conductivity.

3 Experimental procedure

The following chapter summarizes the preparation of SiOC/C ceramics and the experimental methods used to investigate the structural and electrical properties. In addition, the setup for the piezoresistive investigations of SiOC/C is presented.

3.1 Sample preparation

In order to synthesize polymer-derived SiOC/C ceramics commercially available preceramic polymer resins of the companies Starfire Systems Ltd. (Polyramic®: SPR-212, SPR-684 and SPR-688) and Wacker Chemie AG (BELSIL® PMS-MK and SILRES® 604) have been used. Further compositions were obtained by mixing different ratios of either triethoxysilane TREOS (Sigma-Aldrich, purity 95%), methyldiethoxysilane MDES (Sigma-Aldrich, purity 96%), triethoxymethylsilane TEMS (Sigma-Aldrich, purity 98%) or triethoxyvinylsilane TEVS (Sigma-Aldrich, purity 97%). The different mixing ratios are summarized in Table 3.1 and their molecular structure is displayed in Figure 3.1. The sol–gel route used in the present work has already been reported in detail by many authors [35, 167, 168]. Within this work a series of samples was prepared according to the same general procedure using different organic precursors. An exemplary description of the synthesis procedure is given in the following.

Synthesis of the sol-gel derived polymers

8.21g Triethoxysilane (0.05 mol, 1.0 Eq.) and 9.51g Triethoxyvinylsilane (0.05 mol, 1.0 Eq.) are stirred together for 15 min. An acid mixture (pH \approx 5) of water (5.4g, 6.0 Eq.) is added stepwise for condensation and the solution is stirred over night to obtain a homogeneous clear solution. The solution was aged in air for 24 h without using any catalyst. The monolithic transparent pieces of gel were dried at 80 °C for 24 h in a low temperature oven (Apex AX, Carbolite Gero, Neuhausen, Germany) to remove the residual solvent.

Polymer to ceramic transformation

Both commercially and synthesized sol-gel derived polymers were thermally crosslinked in an alumina tube furnace (HTSS 810/10, Carbolite Gero, Neuhausen, Germany) at $T = 250$ °C for 2 h and subsequently pyrolyzed at $T = 1100$ °C for 2 h with a heating and cooling rate of 100 °C/h under a constant flow of argon (5 L/h). To ensure an oxygen free atmosphere during calcination, the chamber is evacuated three times and purged with high purity argon. The resulting black glass is manually milled and sieved to a particle size below ≤ 40 μ m. The sieved powder ($m = 1 - 2$ g) was sealed within graphite foils and hot-pressed (Spark Plasma Sinter System, SPS-211Lx, Fuji Electronics Industrial Co. Ltd., Technical University of Darmstadt, Prof.

Barbara Albert) without any sintering additives at $T = 1600\text{ }^{\circ}\text{C}$ with a uniaxial load of $P = 50\text{ MPa}$ for 15 min under high purity argon atmosphere and a heating rate of $320\text{ }^{\circ}\text{C}/\text{min}$. Only minor mass loss ($< 2\text{ wt.}\%$) was detected after the pressure assisted sintering process and the black dense monoliths were subsequently cut into rectangular shape ($3\times 3\times 10\text{ mm}$) using a diamond wire cutter or kept in a cylindrical shape. To ensure a defined geometrical shape with plane surfaces, the samples were polished using a grinding machine (ZB 42T, Ziersch&Baltrusch, Ilmenau, Germany) equipped with a diamond grinding wheel.

Table 3.1: Ratio of the sol-gel derived polymers and the commercially available preceramic polymers with the corresponding ceramic yield after pyrolysis.

	Sample	Precursors		Ceramic yield	Ref.	
		TREOS	MDES			
Sol-Gel derived polymers	C-0	10	1	87.1	[167, 168]	
	C-1	2	1	88.4		
	C-2	1	2	86.6		
			TREOS	TEMS		
	C-4	2	1	82.2	this work	
	C-6	1	1	80.7		
	C-8	1	2	78.5		
			TREOS	TEVS		
	C-13	1	1	85.0	this work	
	C-15	1	2	87.6		
	C-18	1	3	88.2		
	C-20	1	4	85.1		
Preceramic polymers	C-11	PMS-MK		81.0	[169]	
	C-17	RD-212		85.6	[170]	
	C-36	Silres-604		84.7	this work	
	C-46	RD 688		85.8	[170]	
	C-60	RD-684		82.0	[171]	

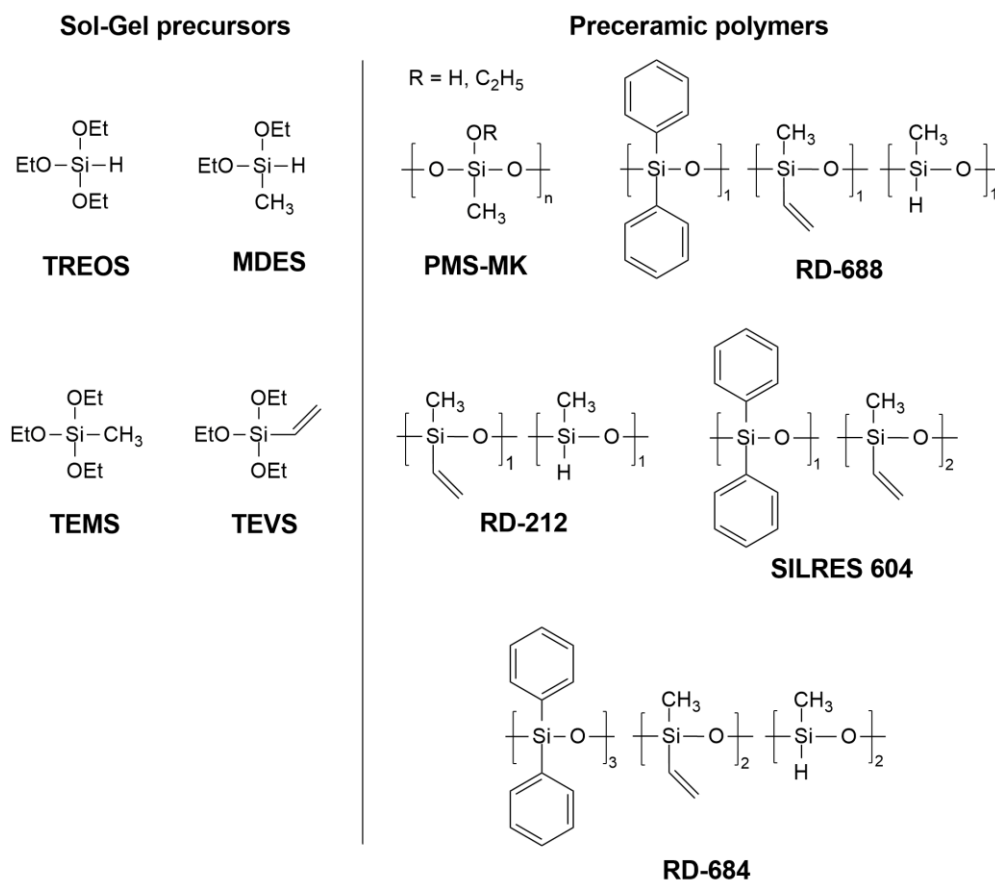


Figure 3.1: Schematic depiction of the sol-gel precursors and the preceramic polymers.

3.2 Materials characterization

The following chapter presents the equipment used for the structural and compositional characterization of the ceramic.

3.2.1 Elemental analysis

The elemental composition of the samples was determined by hot gas extraction. The carbon content of the samples was measured with a carbon analyzer (CS 800, Eltra GmbH, Neuss, Germany) which detects and quantifies the oxidized carbon species by means of IR spectroscopy. An N/O analyzer (Leco TC-436, Leco Corporation, Michigan, US) was used to determine the oxygen content. A similar measurement principle is being used to analyze the oxygen content as the present oxygen of the sample reacts with the graphitic crucible to form CO_2 . The escaping CO_2 can be quantified through IR spectroscopy. The silicon weight fraction was considered to be the difference to 100 wt.%, assuming no other elements being present in the sample.

3.2.2 Density and porosity measurements

The bulk density of the obtained ceramics was determined by the Archimedes method, using distilled water as infiltration medium. Hereby, the sample volume V_S is calculated by the difference between the weight of the dry sample (m_d) in air and submerged in water (m_{n,H_2O}) divided by the density of water ρ_{H_2O} . Accordingly, the volume of the sample V_S reads:

$$V_S = \frac{m_d - m_{n,H_2O}}{\rho_{H_2O}} \quad (3.1)$$

Afterwards, the soaked up sample ($m_{n,air}$) is weighted in air and its mass is subtracted from the weight of the dried sample (m_d) providing the volume of the open pores V_P .

$$V_P = \frac{m_{n,air} - m_d}{\rho_{H_2O}} \quad (3.2)$$

The percentage share of the open porosity is calculated by dividing the volume of the pores V_P by the geometrical volume V_S :

$$P_{open} = 100 \cdot \frac{V_P}{V_S} \quad (3.3)$$

This method only provides access to open pores which can be infiltrated by water. The overall density of the sintered ceramic is calculated according to:

$$\rho = \frac{m_d - \rho_{H_2O} V_S}{m_{n,air} - m_{n,H_2O}} \quad (3.4)$$

3.2.3 Raman spectroscopy

A tunable Ti:sapphire solid state laser (Coherent, Indigo-S) with an excitation wavelength of $\lambda = 256.7$ nm (i.e., 4.8 eV) was employed for the UV Raman studies. Anisotropic BBO (β -barium borate) and LBO (lithium triborate) crystals have been used to generate the UV radiation by frequency tripling the fundamental ($\lambda = 770.1$ nm) of the laser. Scattered radiation is dispersed and detected with a triple stage spectrometer (Princeton Instruments, TriVista 555) equipped with a CCD camera (Princeton Instruments, Spec10:2kBUV). The spectral resolution of the spectrometer is $\mu \approx 1 \text{ cm}^{-1}$. A mirror system has been designed to guarantee an efficient collection of the scattered Raman photons. A spherical mirror (Edmund Optics) focuses the laser beam onto the sample. Two 90° off-axis parabolic mirrors (Thorlabs) collect and refocus the scattered photons into the spectrometer. Prior to each measurement, the spectrometer has been calibrated using boron nitride and the laser power was reduced to $\leq 400 \mu\text{W}$ to avoid sample damage. The acquisition time of each spectrum was ≥ 1 h to obtain a signal-to-noise ratio ≥ 3 .

Visible Raman spectra were recorded with a Horiba HR800 micro-Raman spectrometer (Horiba Jobin Yvon GmbH, Bensheim, Germany) equipped with an Argon laser ($\lambda = 514.5$ nm). The excitation line has its own interference filter (to filter out the plasma emission) and a Raman notch filter (for laser light rejection). The measurements were performed with a grating of 600 and a confocal microscope (magnification 50x, NA = 0.5) with a $100\ \mu\text{m}$ aperture, giving a resolution of approximately $2\ \mu\text{m} - 4\ \mu\text{m}$. The laser power (20 mW) was attenuated by using neutral density filters; thus the power on the sample was in the range from $6\ \mu\text{W}$ to 2 mW. All spectra were background subtracted, smoothed (SMA, simple moving average) and fitted to Lorentzian line shapes using Origin Pro 9.1.0G.

3.2.4 Thermogravimetric analysis

Thermogravimetric analysis (TGA) was performed with a STA 449C Jupiter (Netzsch Gerätebau GmbH, Hanau, Germany) coupled to a FT-IR-spectrometer (Tensor27, Bruker, Massachusetts, USA). The TGA was conducted in order to investigate the thermal stability of SiOC/C in oxidizing atmosphere by measuring the mass change as well as the evolution of carbon monoxide and carbon dioxide. The analysis was performed under a constant oxygen gas flow (Air Liquide, purity $\geq 99.5\%$) and argon gas flow (Air Liquide, purity $\geq 99.5\%$) of 30 ml/L. 100 mg of the ceramic powder were placed into a Al_2O_3 crucible for the measurement. Temperature steps at $T = 200, 400$ and $600\ ^\circ\text{C}$ were set with a heating rate of $5\ ^\circ\text{C}/\text{min}$ and a holding time of 2 h before the measurement temperature was increased to $T = 800\ ^\circ\text{C}$ and $1000\ ^\circ\text{C}$ with a reduced dwelling time of 1 h. The outgasing species were recorded with an FT-IR spectrometer in a range from 500 to $4000\ \text{cm}^{-1}$. The mass change of the sample was recorded with 100 points per minute during the heating ramp and 4 points per minute during the dwelling.

3.2.5 X-ray diffraction

The diffraction pattern were either preformed in flat-sample transmission geometry on a STOE STAD1 P diffractometer (STOE & Cia GmbH, Darmstadt, Germany) equipped with monochromatic Mo-K_α ($\lambda = 0.07093$ nm) radiation for powdered samples or on a STOE X-ray diffractometer using Ni-filtered Cu-K_α ($\lambda = 0.15405$ nm) radiation in case of bulk samples. Both devices are located at the Technical University of Darmstadt in the working group of Prof. Wolfgang Donner. Isoamylacetate was used to fix the powdered samples between two acetate foils for the measurement at the STOE STAD1 P.

3.2.6 X-ray photoelectron spectroscopy

The measurements were conducted at the Technical University of Darmstadt in the working group of Prof. Wolfram Jägermann using a PHI VersaProbe 5000 spectrometer (Physical Electronics Inc. MN, USA) equipped with a monochromatic Al-K_α source ($h\nu = 1486.6$ eV) with a beam diameter of $200\ \mu\text{m}$. The binding energies are referred to the Fermi level of Ag foil. Photoelectrons were collected with the pass energy, $E_{\text{pass}} = 23.5$ eV at $\theta = 45^\circ$ with respect to the surface normal. The background under the high resolution XPS spectra was subtracted by a Shirley-type function using the software XPSPEAK 4.1.

3.2.7 Scanning Electron Microscope

Scanning electron microscopy (SEM) pictures were performed on a Philips XL30 FEG (Philips, Netherlands) by detecting low-energy secondary electrons emitted from the surface (10 - 100 nm) due to excitation by the primary high-energy electron beam. Low conductive samples were coated with a thin layer of gold using an EMITECH K950X (Quorum Technologies Ltd, Kent, UK) in order to avoid charging effects on the sample surface. Imaging was performed at an acceleration voltage of 10 to 25 kV with a secondary electron detector. Semi-quantitative elemental analysis is also possible using energy dispersive X-ray (EDX) module (CDU, EDAX Inc.) via detection of the characteristic X-rays excited by the incident electron beam.

3.3 Electrical investigations

In this chapter the electrode application of the different sample geometries is described together with the experimental setup used to determine their electrical properties. Furthermore, the developed setup to characterize the piezoresistive behavior is presented.

3.3.1 Electrical contacting of the samples

To ensure a good electrical contact and to minimize the contact resistance, on both sample geometries a thin layer (≈ 70 nm) of Au or Pt was sputtered using a EMITECH K950X (Quorum Technologies Ltd, Kent, UK) for 8 min at 40 mA. The cylindrical samples were sputtered on the front side whereas the electrodes of the rectangular samples are located at the long side, as they had to be excluded from the strain direction applied during the piezoresistive measurements. Gold wires ($d = 0.5$ mm) were attached onto the sputtered electrodes in case of the rectangular shaped samples using a gold paste (Gwent group, Pontypool, UK). The paste is burned at $T = 700$ °C in an alumina tube furnace for 1 h under a flowing stream of high purity argon to promote the conductivity and adhesion. The oven chamber is evacuated three times and flushed

with argon to avoid any oxidation reaction. Subsequently, to prevent oxidation during the measurement the electronic contacts are sealed using an Al_2O_3 -based glue (Thermokitt 1100°C, Carl Roth GmbH & Co. KG, Karlsruhe, Germany) by simply drying at $T = 100\text{ °C}$ for 12 h. No change in resistance was observed when the resistance was measured with a four-point method allowing to neglect the contact resistance. Both contacting methods are depicted in Figure 3.2.

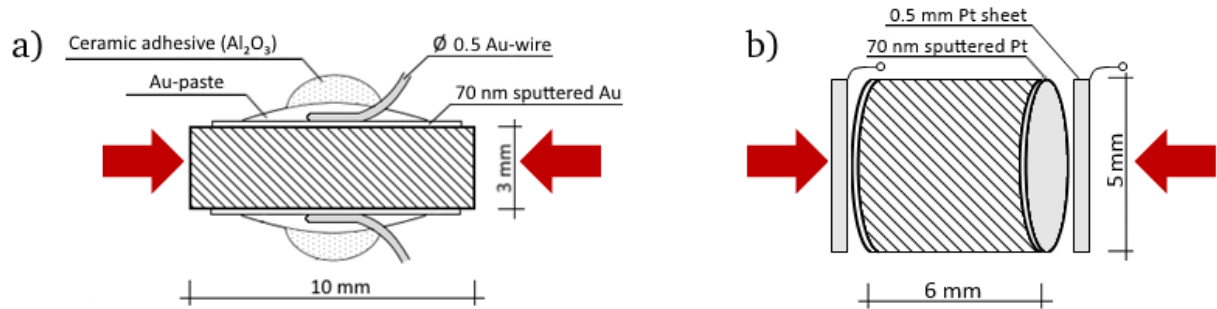


Figure 3.2: Schematic depiction of two different samples geometries with a) the rectangular and b) the cylindrical shape used during the electrical investigations.

3.3.2 Temperature dependent impedance spectroscopy

The impedance spectroscopy offers the possibility to investigate the electrical properties under an alternating current. The device is located at the Technical University of Darmstadt in the working group of Prof. Jürgen Rödel. In the course of the electrical examination the cylindrical samples are clamped between two electrodes (two-point method) within a quartz tube and subsequently hermetically sealed before the tube was slid into a cylindrical alumina furnace (LOBA 1400-45-400-1, HTM Reetz GmbH, Berlin, Germany). Temperatures up to $T = 800\text{ °C}$ are available and are verified by a thermocouple placed next to the sample. The tube is evacuated und flushed with argon (Air Liquide, purity $\geq 99.5\%$) three times before the heating program is started. For electrical investigation an Alpha-A High Performance Modular Measurement System (Novocontrol Technologies, Montabaur, Germany) is used. The measurements are conducted within a frequency range of $\nu = 0.1$ to 3 MHz and an applied voltage of $U = 0.1\text{ V}$.

3.3.3 Piezoresistive measuring chamber

Within this work, a specially developed experimental setup was constructed in cooperation with the Electromechanical Department (EMK) at the TU Darmstadt to assess the static piezoresistive behavior of SiOC/C ceramics. The complete setup and the measurement chamber are depicted in Figure 3.3. The rectangular polished samples were clamped between two plane alumina rods ($\text{Ø} = 5\text{ mm}$) and preloaded with $P = 10\text{ MPa}$ for 30 min. The mechanical load is applied by a stepper motor with a rating of $F = 1000\text{ N}$ and regulated by a load cell

(5900, Sensy S.A, Jumet, Belgium). A digital multifunctional resistance analyzer (2010, Keithley, Munich, Germany) is used to account for the change in electrical resistance upon mechanical loading. The gold wires are connected to four copper wires outside the measurement chamber to avoid any thermo-electrical effects. Through the four-terminal sensing the influence of copper lead resistance can be neglected improving the accuracy, especially for highly conductive samples.

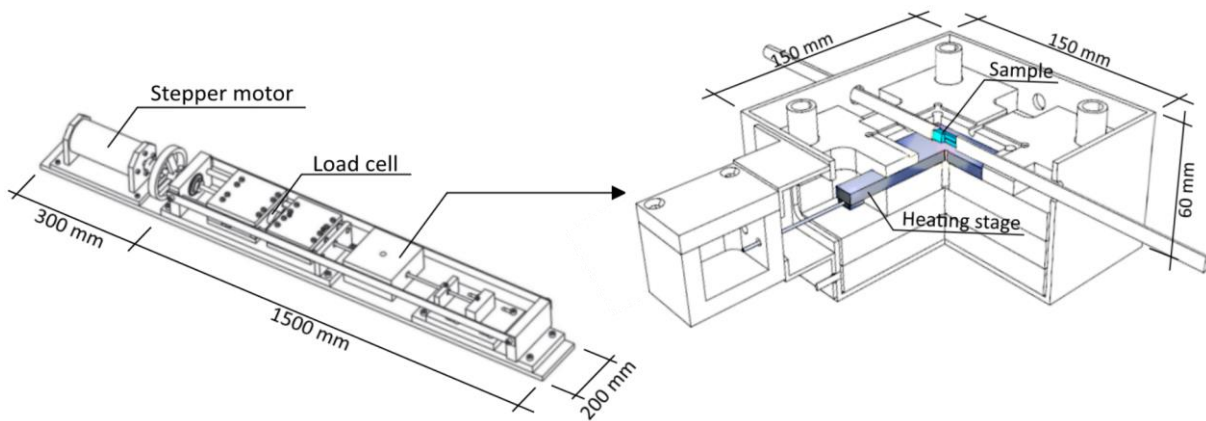


Figure 3.3: Developed experimental setup to determine the piezoresistive effect. The enlarged area represents the measurement chamber.

An operating temperature of up to $T = 1000\text{ }^{\circ}\text{C}$ is achieved through a heating plate (Ultramic, Watlow, USA) located directly under the ceramic sample ($h = 1\text{ mm}$). To reduce the thermal gradient, the inside of the measurement chamber is lined with *Silcapan* (calcium silicate). After heating to $T = 1000\text{ }^{\circ}\text{C}$ for 1 h, the surface temperature of the measurement chamber is about $T = 180\text{ }^{\circ}\text{C} \pm 5\text{ C}$. The measurement chamber additionally offers the possibility to use *in-situ* Raman spectroscopy. Therefore, a window ($\varnothing = 5\text{ mm}$) has been inserted on the upper side of the chamber with magnesium fluoride (MgF_2) as window material due to its high transmission of visible light and high-temperature stability. To avoid thermal damage of the Raman objective a long working distance lens (SLMPLN20x, Olympus, Tokio, Japan) was used with a free working distance of 2.1 cm. A graphical interface for force and temperature control was programmed using LabView 9 which additionally records the measurement data. A measurement uncertainty of 0.4% regarding the force transmission is determined for the developed setup. The obtained data is evaluated using Origin Pro 9.1.0G.

3.3.4 High-temperature piezoresistive setup

In order to determine the high-temperature piezoresistive effect, an experimental setup located at the Research Center Jülich (FZJ) was used. The cylindrical samples were placed in a furnace allowing for measurements of up to $1500\text{ }^{\circ}\text{C}$. After achieving the desired temperature, the uniaxial load was applied by a mechanical testing machine (Model 5565, Instron Corp., Canton,

MA, USA) using alumina rods as extensions. Two platinum electrodes were used for electronic contacting. To ensure a low contact resistance and to exclude any pressure induced changes in resistance, the electrodes were preloaded with $P = 3$ MPa. The resistivities of the loaded and unloaded samples, respectively, were calculated from the observed voltage changes using a multifunctional resistance analyzer (2010, Keithley, Munich, Germany).

3.3.5 Hall measurements

Hall measurements were conducted to measure the electrical conductivity, the Hall constant, carrier mobility and carrier density of the bulk ceramic by the means of an IMP-HT-Hall-900K system (Fraunhofer IPM, Freiburg, Germany) at the University of Mainz. Square-shaped samples (1x10x10 mm) are placed into a sample holder installed within a vacuum chamber. To reduce measurements uncertainties, only samples with parallel main surfaces are used. The chamber is subsequently evacuated and flushed with argon (Air liquid, purity 99.5%). To measure the specific electrical conductivity, the sample is contacted according to the van-der-Pauw measurement theory. Thus, four points are connected at the edge of the sample whereas on one side of the sample the current is applied and on the other side the resulting voltage is measured. The separation of the current and voltage electrode eliminates the contact and lead resistance from the measurement and thereby increases the accuracy. The measurement is done in all four permutations of the contacts, and due to the used AC-resistance bridge in both polarisations. The vacuum chamber moves into positive and negative field position to determine the Hall coefficient and carrier concentration and mobility.

4 Results and discussion

In chapter 4.1 the material properties of SiOC/C are discussed in detail followed by the Raman study of the carbon phase in chapter 4.2. In the following two chapters 4.3 and 4.4 the electrical and piezoresistive properties of SiOC/C are reported which ultimately lead to a development of a preliminary sensor prototype.

4.1 Structural characterization and thermal stability of SiOC/C

This chapter delivers a short survey over the various synthesized silicon oxycarbides (SiOC/C) and how the sintering parameters have to be adjusted in order to ensure a dense bulk ceramic. Density and porosity measurements were performed to follow the densification process. The related change in microstructure and crystallinity is investigated through XRD and XPS measurements. Finally, the thermal stability of the ceramic is investigated by the means of TGA-FTIR measurements up to $T = 1000\text{ }^{\circ}\text{C}$.

4.1.1 Phase composition

In general, SiOC/C glasses can easily be prepared through a direct polymer-to-ceramic transition by pyrolysis of cross-linked poly-organosiloxane networks. These networks contain Si-R bonds ($R = \text{H}, \text{CH}_3, \text{CH}_2\text{CH}_3, \text{C}_6\text{H}_5, \dots$) and can be produced from monomeric organosiloxanes precursors using the sol-gel process and preceramic polymers. A schematical depiction of the sol-gel process and the development of a sol-gel-derived organosiloxane network is illustrated in Figure 4.1.

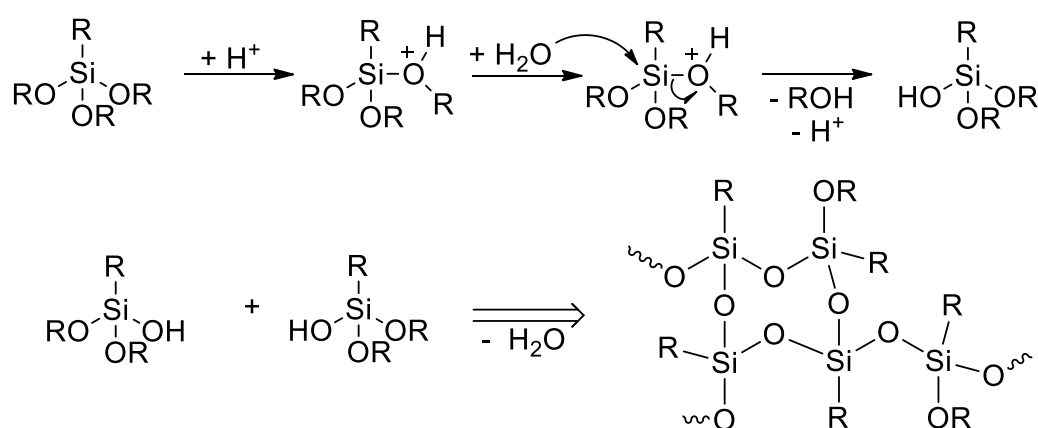


Figure 4.1: Schematically depiction of the sol-gel process and the derived organosiloxane network.

In the present work, either triethoxyvinylsilane (TEVS) or triethoxymethylsilane (TEMS) were mixed with triethoxysilane (TREOS) in different ratios to tailor the chemical composition, notably the amount of residual carbon within the microstructure after pyrolysis. The latter

precursor ensures the establishment of a well-connected network, to lower the mass loss during the pyrolysis step, while the first precursors incorporate carbon into the organosiloxane network. The large range of composites synthesized are presented in the ternary Si-O-C phase diagram displayed in Figure 4.2.

The majority of samples were prepared at $T = 1600\text{ }^{\circ}\text{C}$ and mainly consist of SiO_2 , SiC and C [32]. Most of the compositions synthesised during this work (represented by the green dots) are located in the SiO_2 -rich area and exhibit a linear change in composition with increasing amount of carbon. Some of the commercially obtained poly-organosiloxanes (represented by the red dots) deviate from the linear dependency which is due to their different chemical functionalization and/or crosslinking situation in the initial polymeric stage. The connecting line between SiC and SiO_2 represents compositions in which all carbon is bonded to silicon and no excess carbon is present. Compositions above that line, inside the $\text{SiC-SiO}_2\text{-Si}$ triangle lead to the presence of elemental silicon. However, the vast majority of reported SiOC/C glasses studied so far usually contain excess carbon and their composition falls inside the $\text{SiO}_2\text{-SiC-C}$ triangle following the expression $\text{SiC}_x\text{O}_{2(1-x)} + \text{C}_y$.

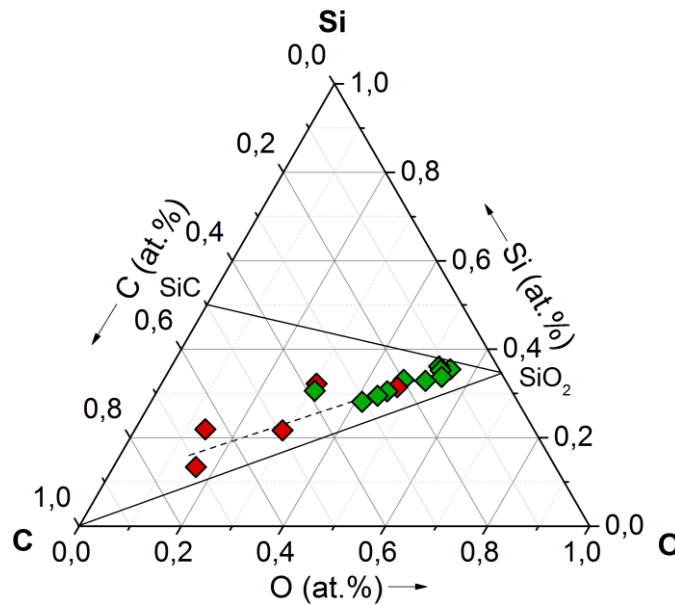


Figure 4.2: Si-O-C phase diagram including the compositions of silicon oxycarbide ceramics pyrolysed at $T = 1600\text{ }^{\circ}\text{C}$. The green dots represent synthesised compositions, while the red dots are derived from commercially available perceramic polymers.

Two assumptions are required to calculate the amount of excess carbon from the elemental analysis. The first premise is that oxygen is strictly bonded to silicon and that no carbon-oxygen bonds are present in the ceramic [172]. In addition, if the materials are fired at temperatures $T > 1000\text{ }^{\circ}\text{C}$ the hydrogen content is below 1 wt.% and can be neglected [173]. Assuming a density of $\rho = 1.45\text{ g/cm}^3$ for the segregated carbon [174] and a density value of $\rho = 2.3\text{ g/cm}^3$

for the amorphous SiO_xC_y network [172] the volume fraction of the carbon phase ϕ_c can be calculated according to:

$$\phi_c = \frac{\{[y - (1 - \frac{x}{2})] \cdot M_C\} / \rho_C}{\{1 \cdot M_{Si} + x \cdot M_O + y \cdot M_C\} / \rho_{\text{SiO}_x\text{C}_y}} \quad (4.1)$$

When the preparation temperature exceeds $T > 1300^\circ\text{C}$, phase separation of the amorphous network and ordering of the segregated carbon occurs. Therefore, the density of segregated carbon may increase up to $\rho = 1.82 \text{ g/cm}^3$ [175], while the overall density of the ceramic is mainly determined by the resulting components SiO_2 (2.33 g/cm^3) [176] and SiC (3.21 g/cm^3) [177]. Thus, in a phase separated system, the volume fraction of the segregated carbon phase is given by:

$$\phi_c = \frac{\{[y - (1 - \frac{x}{2})] \cdot M_C\} / \rho_C}{\{[y - (1 - \frac{x}{2})] \cdot M_C\} / \rho_C + (\{\frac{x}{2} \cdot M_{\text{SiO}_2}\} / \rho_{\text{SiO}_2}) + (\{1 - \frac{x}{2} - \frac{3z}{4} \cdot M_{\text{SiC}}\} / \rho_{\text{SiC}})} \quad (4.2)$$

A brief summary of selected compositions heat treated at $T = 1600^\circ\text{C}$ is presented in the following Table 4.1. The SiOC/C samples are labelled according to their volume fraction of excess carbon. Hence a sample with a volume fraction of $\phi_c = 11 \text{ vol. \%}$ of segregated carbon is designated as C-11.

Table 4.1: Elemental analysis of selected samples after pyrolysis at $T = 1600^\circ\text{C}$ for 15 min in Argon.

Sample	weight percent fraction			SiOC/C	volume percent fraction		
	Si	O	C	empirical formula	SiO_2	SiC	C
C-1	50.97	42.14	6.89	$\text{SiO}_{1.45}\text{C}_{0.28} + 0.04\text{C}$	84.27	14.55	1.18
C-8	48.38	38.69	12.93	$\text{SiO}_{1.42}\text{C}_{0.29} + 0.31\text{C}$	77.42	14.38	8.20
C-11	46.65	39.40	13.95	$\text{SiO}_{1.48}\text{C}_{0.26} + 0.44\text{C}$	76.75	12.24	11.01
C-17	49.13	26.44	24.43	$\text{SiO}_{0.94}\text{C}_{0.53} + 0.63\text{C}$	54.49	27.83	17.68
C-36	36.53	27.90	35.57	$\text{SiO}_{1.34}\text{C}_{0.33} + 1.95\text{C}$	51.91	11.66	36.43

From Table 4.1, a linear decrease of the SiO_2 phase can be identified as the amount of carbon is raised and incorporated into the microstructure. The same trend is found in Figure 4.3 which summarizes the evolution of the SiO_2 and SiC phase as a function of the carbon volume fraction for all samples synthesized during this work. All samples shown have been prepared under the same conditions ($T = 1600^\circ\text{C}$; $P = 50 \text{ MPa}$).

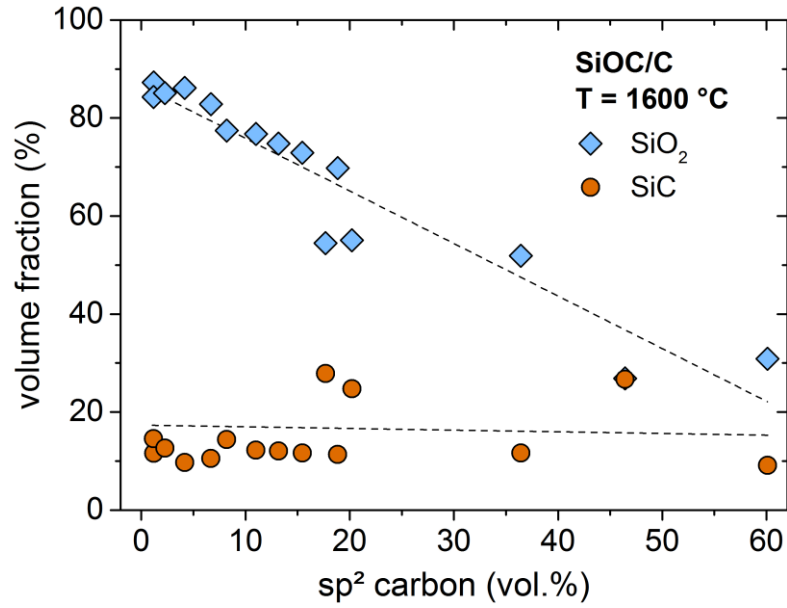
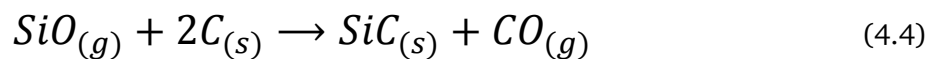
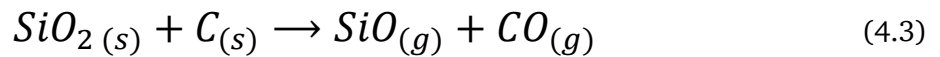


Figure 4.3: Evolution of SiO₂ and SiC as a function of the segregated carbon phase.

Following the course of Figure 4.3, an increasing amount of segregated carbon seems to occur at the expense of the SiO₂ phase, while the SiC phase remains rather unaffected. However, this phenomenon is misleading, as the segregated carbon phase reduces the volume fraction of the whole SiOC network (SiO₂+SiC). Therefore, as the amount of carbon rises, the sp³ carbon within the amorphous SiOC network also increases. This leads to a higher fraction of SiC within the SiOC network after the phase separation process and compensates the percentage volumetric loss of the overall SiOC network resulting in a pseudo constant volume fraction of SiC with increasing amount of carbon.

In general, the development of the SiC phase is related to two processes: (i) the phase separation process of the amorphous matrix occurring at $T \geq 1300$ °C and (ii) the solid state reaction at the interface between the SiO₂ and the carbon phase, called carbothermal reaction given by Equation 2.3 on page 7. In order for the carbothermal reaction to occur, temperatures above $T > 1500$ °C are needed. As suggested by several authors [178],[179] this reaction does not proceed in a single step but rather by the following mechanism (4.3) and (4.4):



It is difficult to decide which of the two pathways exactly dominates the evolution of SiC, but as long as enough carbon is available, the evolution of the SiC phase is defined by the chosen synthesis temperature.

4.1.2 Densification process

Figure 4.4 a) displays the densities of sample C-11 and C-17 as a function of the thermal treatment between $1000\text{ }^{\circ}\text{C} < T < 1800\text{ }^{\circ}\text{C}$. No densification could be achieved at temperatures below $T \leq 1000\text{ }^{\circ}\text{C}$ as only highly porous samples, not able to retain their shape, were obtained. The density of both samples progress in a comparable manner with increasing pyrolysis temperature in the range of $\rho = 2.2 - 2.3\text{ g/cm}^3$ with C-17 having a slightly greater density. Upon further annealing at temperatures above $T > 1600\text{ }^{\circ}\text{C}$ the density of C-17 increases up to $\rho = 2.75\text{ g/cm}^3$, while the density of C-11 only slightly increases up to $\rho = 2.38\text{ g/cm}^3$. The strong increase in density of C-17 can be explained in terms of the higher amount of segregated carbon and the thermally promoted carbothermal reaction which converts the silica phase into silicon carbide. The obtained density of C-17 at $T = 1800\text{ }^{\circ}\text{C}$ is in accordance with the literature-known values of amorphous silicon carbide [180].

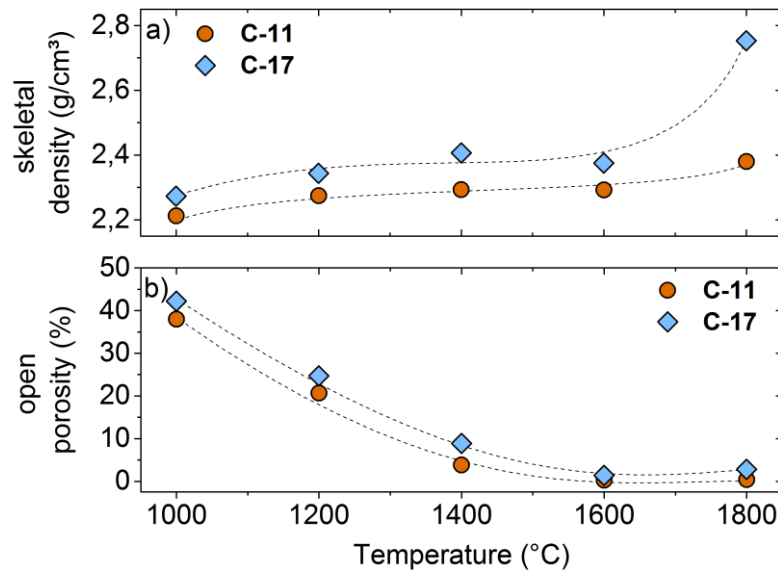


Figure 4.4: Density and residual open porosity of C-11 and C-17 heat treated at various temperatures.

The porosities of both samples (C-11 and C-17) is depicted in Figure 4.4 b). In both cases an open porosity of $\Phi \approx 40\%$ is obtained when the samples are prepared at $T = 1000\text{ }^{\circ}\text{C}$. Increasing the temperature up to $T = 1600\text{ }^{\circ}\text{C}$ under a constant pressure constantly reduces the porosity down to $\Phi = 0.1\%$ for C-11 and $\Phi = 1.1\%$ for C-17. Further annealing up to $T = 1800\text{ }^{\circ}\text{C}$ causes the porosity of both samples to slightly increase as the carbothermal reaction gain in significance causing decomposition of the sample. To avoid any decomposition reactions, yet to ensure a dense microstructure, which is essential for a reproducible piezoresistive effect, the synthesis temperature was set to $T = 1600\text{ }^{\circ}\text{C}$ with a holding time of 15 min and a pressure of $P = 50\text{ MPa}$. In addition, graphite sealing foils and graphite dies were used during the synthesis to separate the ceramic powder from the punch and furthermore to suppress the carbothermal

reaction. It was found that the chemical composition of the sample remains constant regardless if the applied heat treatment is raised. This is emphasized in Table 4.2 and proves that the carbothermal reaction is suppressed in C-11 under the given circumstances [181].

Table 4.2: Elemental analysis of sample C-11 pyrolysed at temperatures between $T = 1000 - 1800$ °C.

Temp.	weight percent			SiOC/C	volume percent		
	Si	O	C	empirical formula	SiO ₂	SiC	C
1000 °C	47.27	38.71	14.02	SiO _{1.44} C _{0.28} + 0.41C	75.91 ^a	13.56 ^a	10.53
1200 °C	46.56	39.02	14.42	SiO _{1.47} C _{0.26} + 0.46C	76.03 ^a	12.48 ^a	11.49
1400 °C	45.88	39.65	14.47	SiO _{1.52} C _{0.24} + 0.50C	76.72	11.16	12.12
1600 °C	46.65	39.40	13.95	SiO _{1.48} C _{0.26} + 0.44C	76.75	12.24	11.01
1800 °C	46.89	38.70	14.41	SiO _{1.45} C _{0.28} + 0.44C	75.67	13.15	11.18

^a= formal chemical composition of the amorphous SiOC network.

Figure 4.5 displays SiOC/C samples with various carbon content all prepared under the same conditions ($T = 1600$ °C, $P = 50$ MPa, $t = 15$ min). The SEM images reveal that only samples up to a carbon volume fraction of $\phi_C = 17$ vol.% can be densified ($\Phi < 1\%$) under the given parameters.

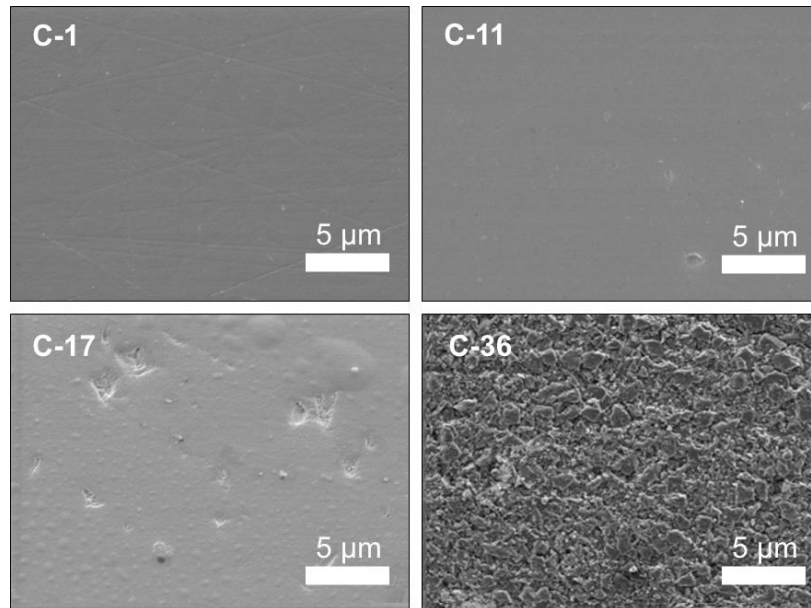


Figure 4.5: SEM images of different SiOC/C samples prepared at $T = 1600$ °C under $P = 50$ MPa.

Higher carbon concentrations lead to silica domains fully encapsulated by a thin layer of carbon which act as a diffusion barrier and thus hinders the viscous flow and densification process of the SiOC/C system [37, 153]. Furthermore, partial decomposition may take place at temperatures above $T > 1400$ °C which retards the densification process due to gas formation [182]. However, this can be excluded due to a rather small equilibrium rate constant of $K_p = 0.072$ for the carbothermal reaction at $T = 1430$ °C. According to the thermodynamic calculations of Plachký *et al.*, a CO pressure of $p_{CO} = 0.07$ bar is necessary to suppress the

carbothermal reaction at $T = 1600\text{ }^{\circ}\text{C}$. Through the usage of graphite sealing foils the partial pressure of CO at the vicinity of the sample surface is assumed to be sufficiently high enough to shift the equilibrium suppressing the carbothermal reaction during synthesis [181]. Hence, the preparation and densification of SiOC/C bulk ceramics is thermally restricted by the carbothermal reaction due to the decomposition of the material and by the amount of segregated carbon limiting the densification process.

4.1.3 Crystallization and bonding situation

To investigate the crystallization behavior of SiOC/C and to clarify if the amount of excess carbon does have an influence on the crystallization behavior, X-ray diffraction were performed. The XRD pattern of C-17, C-11 and C-1 heat treated at temperatures from $T = 1200$ to $1800\text{ }^{\circ}\text{C}$ with a holding time of 15 min are given in Figure 4.6.

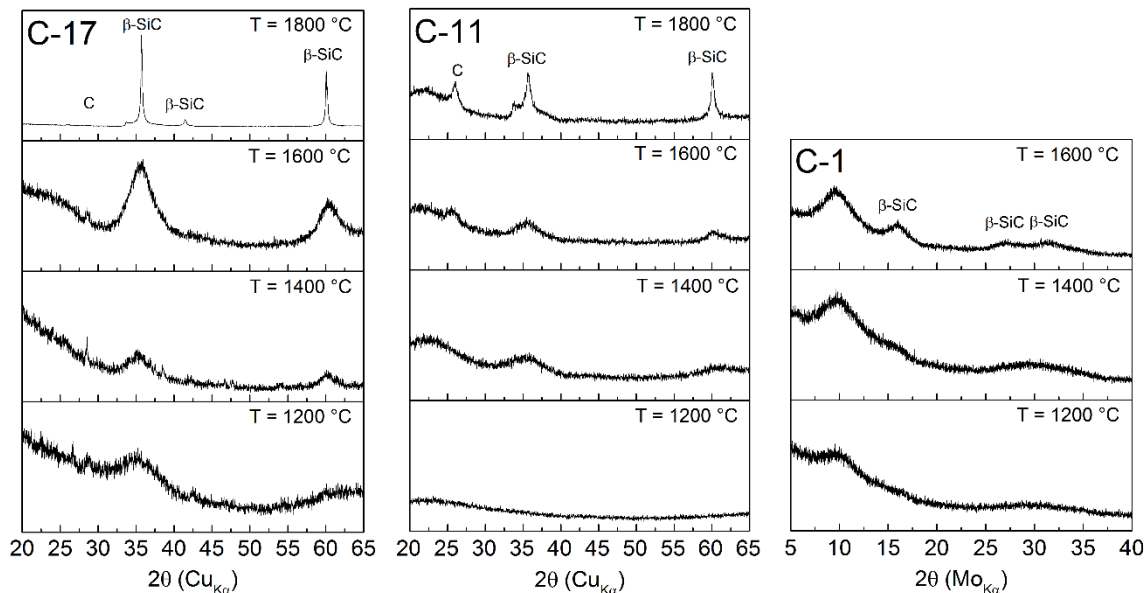


Figure 4.6: XRD patterns of C-17, C-11 and C-1 synthesized at temperatures between 1200 - 1800 °C.

The sample C-11 prepared at $T = 1200\text{ }^{\circ}\text{C}$ was found to be X-ray amorphous with a broad halo around $2\theta = 22^{\circ}$ corresponding to a disordered silica structure [35]. Upon further annealing, broad and weak signals of β -SiC emerge, which gain in intensity and shape until the final temperature of $T = 1800\text{ }^{\circ}\text{C}$ is reached. The crystallization of SiC is represented by the major reflexes at $2\theta = 35^{\circ}$ and 60° corresponding to the (111) and (101) β -SiC lattice planes. A similar crystallization pathway is found for the C-17 sample with the difference that the key signatures of β -SiC already appear at $T = 1200\text{ }^{\circ}\text{C}$ and that the crystalline reflexes at the highest temperature reading $T = 1800\text{ }^{\circ}\text{C}$ clearly display a higher fraction of crystallinity. The small shoulder at $2\theta = 33.5^{\circ}$ appears due to stacking faults in β -SiC. Considering the amorphous nature and neglecting the internal strain within the precipitation the β -SiC particle size can be

roughly estimated according to the Scherrer equation. Hence, when the temperature is raised from $T = 1600\text{ }^{\circ}\text{C}$ to $1800\text{ }^{\circ}\text{C}$, the crystallite size of SiC within C-11 increased from 2.5 to 6.8 nm. In case of C-17, the crystalline size grew by the factor of 10 from 3.0 to 32.2 nm.

HR-TEM investigations support these findings, revealing that the β -SiC crystallite size is about 2 - 4 nm when treated at $T = 1600\text{ }^{\circ}\text{C}$. In addition, the measurements suggest that the majority is located in close proximity to the edges of carbon segregations [36, 37]. The carbon atoms at the edges are expected to be less stable at elevated temperatures and thus are being assumed to be the nuclei of further SiC crystal growth [183]. Although, diffuse reflexes of SiC are already obtained at $T = 1200\text{ }^{\circ}\text{C}$, it remains an open question if the origin of initial β -SiC precipitations is due to reorganization of the amorphous SiOC phase and the subsequent carbothermal reaction or either due to decomposition of the amorphous SiCO microstructure directly leading to β -SiC [32]. The relatively weak reflex at $2\theta = 26.7^{\circ}$ is related to carbon segregations within the SiOC microstructure and is associated to graphitic in-plane structures [171]. The XRD pattern of C-1 showed no reflexes at all being completely amorphous up to $T = 1600\text{ }^{\circ}\text{C}$. This is rather interesting as one would expect, that due to the low amount of carbon the formation of cristobalite should not be obstructed.

Nevertheless, no signs of cristobalite, which is usually formed in vitreous silica at temperatures exceeding $T > 1200\text{ }^{\circ}\text{C}$, are found in the XRD pattern. A possible reason is the phase separation process of the amorphous network as long as the separation distance of the SiO_2 and SiC domains is less than 1.0 nm. The low distance between the separated domains might be in fact too small for nucleation to occur [36]. Saha and Raj assumed a low interfacial energy between SiC and SiO_2 as a possible reason for this phenomenon [32]. Moreover, the segregated carbon phase may obstruct long-range diffusion of silica cluster, not allowing the formation of small clusters required to nucleate cristobalite.

The important role of the segregated carbon phase in terms of the crystallization behavior have been pointed out by many researches [172, 184, 185]. According to Sousa *et al.* [186], carbon-rich SiOC leads to larger SiC crystals but when decreasing the carbon concentration, smaller SiC crystallites are obtained and cristobalite starts to crystallize. In this study, similar findings regarding the crystallization behavior of SiC have been found but no signs of cristobalite were discovered suggesting that the carbon concentration is still high enough to obstruct the crystallization even in carbon depleted samples. The absence of cristobalite and the diffuse XRD reflexes together with the nano-sized β -SiC precipitates indicates that these materials exhibit an outstanding resistance against crystallization in the range of $T \leq 1600\text{ }^{\circ}\text{C}$. This phenomenon is assumed to rely on the segregated carbon phase distributed throughout the whole SiOC microstructure. However, as soon as the temperature is raised above $T = 1600\text{ }^{\circ}\text{C}$, the

carbothermal reaction becomes an increasingly important parameter promoting the crystallization of β -SiC under decomposition of the SiOC/C ceramic.

To gain further insight into the different types of bonds and their distribution within the SiOC matrix, high resolution XPS and MAS-NMR techniques are commonly used, due to their high sensitivity to the chemical surrounding of silicon atoms. Five combinations of mixed silicon tetrahedra may be present in a SiOC matrix, schematically depicted in Figure 4.7. Several studies addressing the distribution of these units were performed using MAS-NMR technique. They could show that, below $T < 1300\text{ }^{\circ}\text{C}$ the amorphous SiOC matrix consist of all five silicon tetrahedral units, but is mostly divided into oxygen-rich and carbon-rich domains [31, 33].

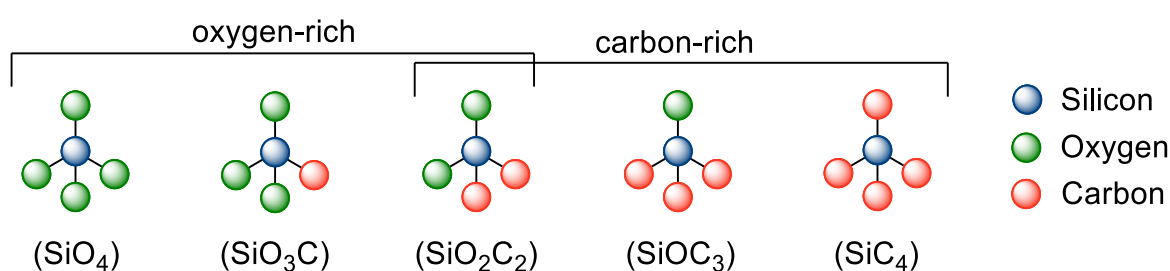


Figure 4.7: A schematic of the five mixed silicon tetrahedra units found in silicon oxycarbide materials.

Above $T > 1300\text{ }^{\circ}\text{C}$, the majority of the mixed tetrahedra diminishes and in general transforms into SiC₄ and SiO₄ units [37, 167]. The XPS technique is a typical surface technique (5 - 7 nm) that delivers valuable information about the different bonding situations. However, it should be noted here, that in amorphous materials where variations in bond length and angle causes broadening of peaks which lead to uncertainties in quantifying species with almost identical chemical shift, such as the mentioned mixed silicon-tetrahedra.

For SiO₂ and SiC, the Si(2p) electrons exhibit binding energies of 103.0 eV and 100.1 eV, respectively. The Si(2p) spectrum obtained from C-1, C-11 and C-17 (all densified at $T = 1600\text{ }^{\circ}\text{C}$ and $P = 50\text{ MPa}$) are displayed in Figure 4.8 showing a broad cumulative peak with a small shoulder at lower binding energies. The peak spans over the typical binding energies of SiO₂ and SiC suggesting the presence of mixed silicon tetrahedra [187, 188]. The largest area in all samples is governed by the Si-O bonding signal at 103.3 eV corresponding to a silica near structure. The peak at 100.5 eV is assigned to Si-C bonds closely related to SiC structures. Due to the amorphous nature of the ceramic and the nearly identical binding energies of the mixed units, no appropriate distinction between them could be drawn. In case of C-1, the peak is located around 101.7 eV and slightly shifts towards higher binding energies (102.0 eV) with increasing amount of carbon.

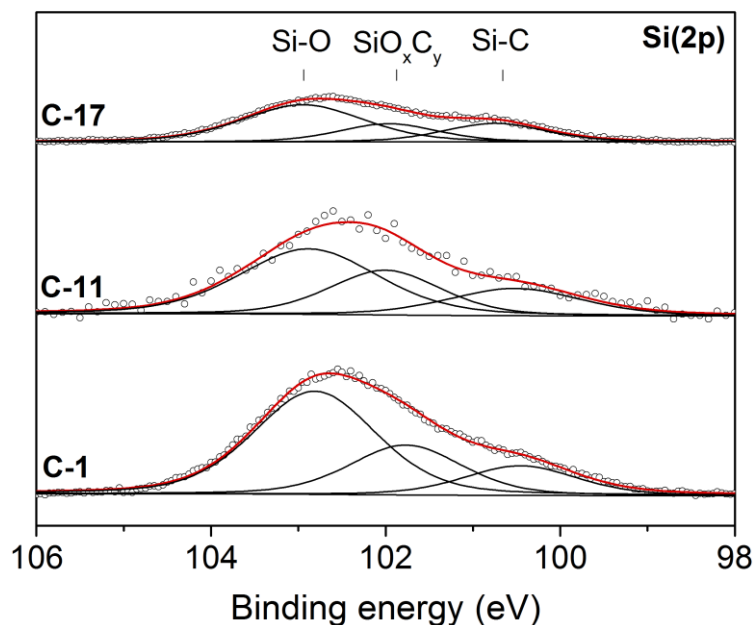


Figure 4.8: Experimental Si(2p) spectrum for C-1, C-11 and C-17 all prepared at $T = 1600\text{ }^{\circ}\text{C}$.

The fact that even after the highest temperature treatment ($T = 1600\text{ }^{\circ}\text{C}$) fully-phase separated SiOC/C still contains mixed tetrahedra is quite surprising as MAS-NMR studies suggest only the presence of SiO_2 and SiC. However, the existence of mixed tetrahedra in phase-separated SiOC has been already proposed in the past and are assumed to be located at the interface between the SiC nanoparticles and the silica matrix [36, 189].

The XPS C(1s) spectrum presented in Figure 4.9 suggests the presence of three components at 282.9, 284.4 and 286.4–286.7 eV. The peak located at 282.9 eV is assigned to Si-C bonds whereas the second peak at 284.4 eV is due to aromatic C-C bonds. Both peaks increase in area as the amount of carbon is raised from C-1 to C-17.

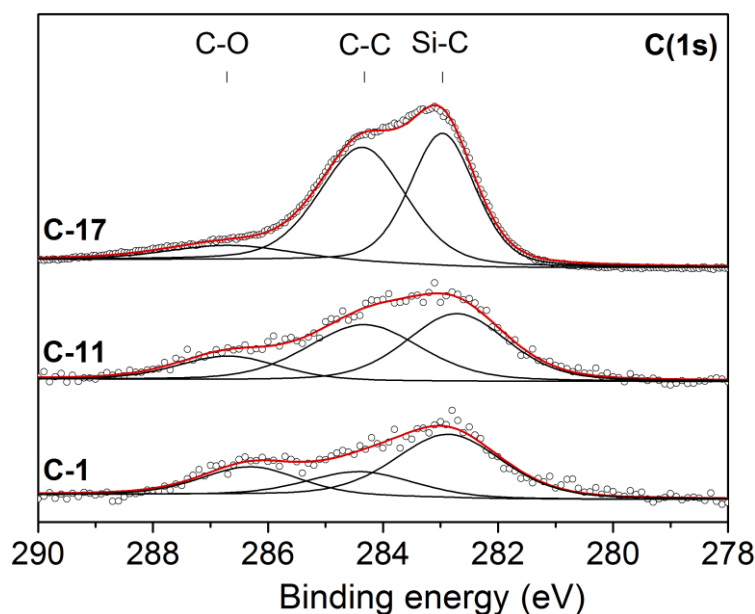


Figure 4.9: Experimental C(1s) spectrum for C-1, C-11 and C-17 all prepared at $T = 1600\text{ }^{\circ}\text{C}$.

The assignment of the last peak in range of 286.4 - 286.7 eV is uncertain. As the XPS technique is a surface sensitive technique, the C-O peak might be assigned to a surface oxidation. Another possibility involves the carbothermal reaction and may consider C-O bonds as an intermediate stage during the commencing reduction of the SiO₂ network [188].

Figure 4.10 presents the O(1s) XPS spectrum showing three types of oxygen bonds located between 530.7 - 531.3, 532.0 - 532.2 and 533.0 - 533.3 eV. The latter peak is assigned to Si-O bonds of silica-near structures and is greatest for C-1. Increasing the amount of carbon causes the peak to decrease which is in agreement with the accompanied decline of the SiO₂ phase. No clear differentiation between the mixed silicon units, represented by the peaks between 532.0 – 532.2 eV, could be made. The last peak at 531.0 eV can be assigned to C-O. In case of the C-17 sample, the peak shifts to binding energies of about 530 eV making it difficult to designate a certain bond.

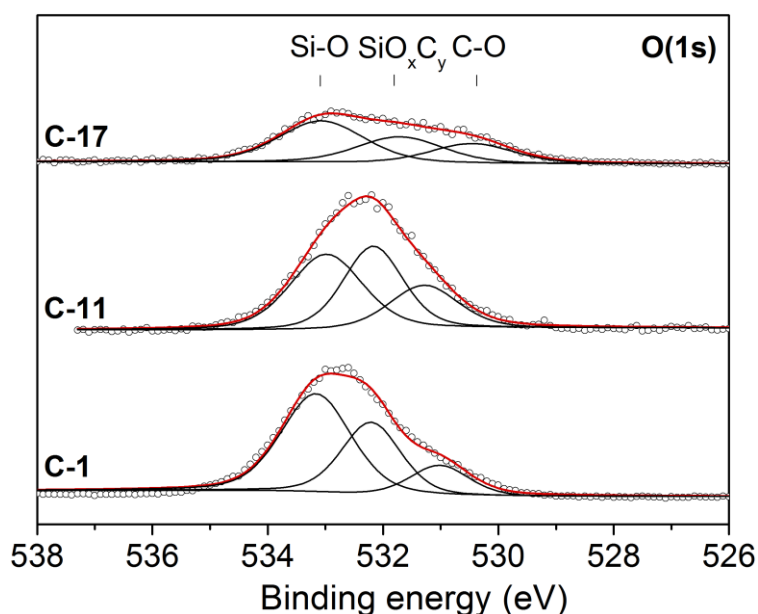


Figure 4.10: Experimental O(1s) spectrum for C-1, C-11 and C-17 all prepared at T = 1600 °C.

In summary, the XPS technique provides valuable information about the binding situation in SiOC/C revealing the presence of mixed silicon units even at synthesis temperatures up to T = 1600 °C. Nevertheless, a profound knowledge about the bonding situation will only be gained with the help of other techniques such as the MAS-NMR [31, 190]. However, further MAS-NMR and XPS studies are needed to support the presented data, especially as XPS is a surface sensitive technique.

4.1.4 Impact of oxidation on the electrical conductivity

Little attention has been paid to the temporary stability of the electrical properties of silicon oxycarbide materials in literature so far [191], although it represents a sensitive measure of its oxidation behavior. Therefore, this chapter examines the electrical conductivity under oxidizing atmospheres to determine the potential usage of SiOC/C as a sensor material at elevated temperatures.

Figure 4.11 depicts the electrical resistivity of a C-17 sample heated at $T = 200\text{ °C}$, 400 °C and 500 °C in air with a dwelling time of 1 h. The resistivity decreases with increasing temperature suggesting activated transport and remains constant at the dwelling times. Degradation of SiOC/C is obviously not relevant up to temperatures of $T = 500\text{ °C}$ and the temporary stability of the electrical signal is sufficient for the intended sensor development, see chapter 4.4.5. However, other sensor applications may require a better long-term stability of the electrical signal and a more comprehensive study should be carried out.

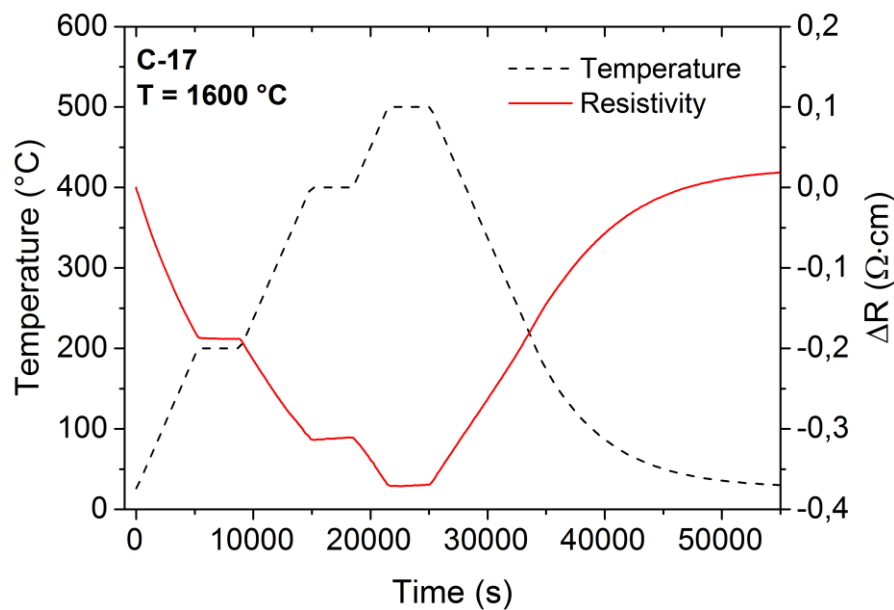


Figure 4.11: The course of the electrical resistivity of C-17 heated up to $T = 500\text{ °C}$ in air.

The degradation of SiOC/C has been also checked by thermo-chemical measurements. Figure 4.12 shows the thermogravimetric analysis coupled with Fourier Transform Infrared Spectroscopy (TGA-FTIR) of C-11 and C-17 heated up to $T = 1000\text{ °C}$ in air.

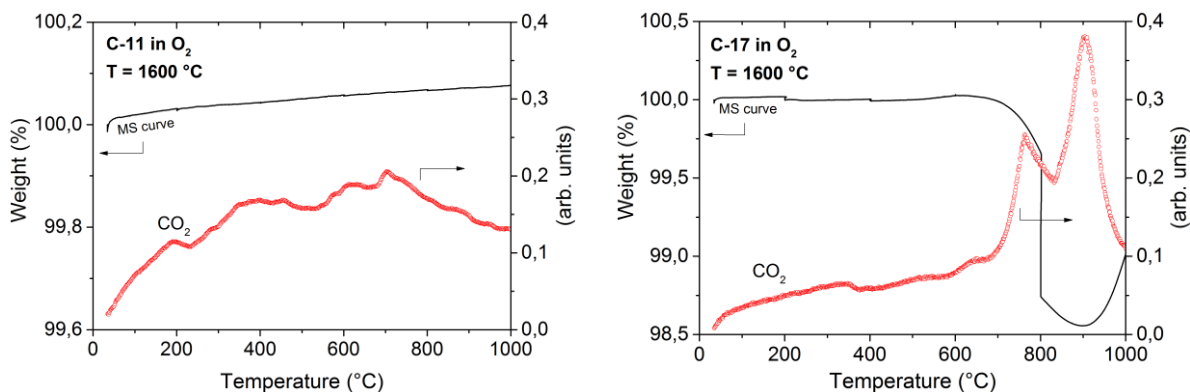
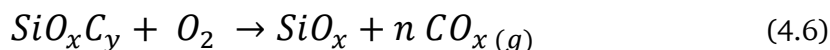


Figure 4.12: TGA-FTIR spectrum of a) C-11 and b) C-17 in the temperature range of 25 – 1000 °C.

A very small mass gain of 0.05 wt.% accompanied by a weak CO₂ signal is detected for C-11 up to T = 1000 °C. A comparable mass gain is obtained for C-17 but only up to a temperature of T = 600 °C. At higher temperatures a steep mass decrease of 1.5 wt.% occurs at about T = 800 °C. If the temperature is further raised up to at T > 900 °C the mass increases again by about 1.1 wt.%. The changes in mass are accompanied by the respective changes of the CO₂ signal and may be explained by the following reactions [191, 192]:



At temperatures T > 600 °C the continuously increasing CO₂ signal indicates the oxidation of carbon according to Equation 4.5. In the second oxidation regime, at temperatures above T > 900 °C the observed mass gain is due to the uptake of oxygen (Equation 4.6) leading to carbon depletion in the SiOC matrix and the formation of a thin insulating silica layer. According to Renlund *et al.* a 2 μm thick SiO₂ surface layer is formed when the SiOC/C is subjected to T = 1420 °C for 240 h in air [193].

4.1.5 Summary

In this work SiOC/C ceramics with different amount of segregated carbon ($\phi_c = 1 - 46$ vol.%) have been prepared by pyrolysis of home-made preceramic polymers and commercially available preceramic polymer resins. The samples have been rapidly densified by spark plasma sintering (1000 < T < 1800 °C, 50 MPa, t = 15 min, Ar) suppressing the carbothermal reaction occurring at T > 1500 °C. Main advantages of this preparation method are that very dense samples ($\Phi < 1$ %) are obtained and that the carbon concentration remains constant for each synthesis temperature. According to XRD the samples stays amorphous up to T = 1600 °C and the composite material can be described in a first approximation as a simple two-phase system of a glassy matrix and segregated carbon. The thermal stability of SiOC/C has been investigated

in order to assess the applicability of SiOC/C as strain sensor competitive to commercially available silicon-based sensors with a temperature limit of about $T = 300\text{ }^{\circ}\text{C}$. The TGA-FTIR measurements indicate that SiOC/C is stable beyond this limit enabling the development of corrosion-resistant high-temperature strain sensors.

4.2 Raman scattering in carbon materials

The Raman spectroscopy is a powerful and non-destructive technique, which allows for assessing lattice dynamics and vibrational spectroscopy of carbon-based materials such as amorphous carbon, [79, 194] carbon nanotubes, [195-197] graphene, [198, 199] graphite [200, 201] and diamond-like carbon (DLC) materials [202, 203]. It is very sensitive to the hybridization state of carbon and provides valuable information about the degree of structural order within the carbon phase. The Raman spectrum of, e.g., diamond shows a single peak at 1333 cm^{-1} due to the tetrahedral sp^3 bonds, whereas highly oriented pyrolytic graphite (HOPG) exhibits a peak at 1580 cm^{-1} assigned to the in-plane stretching vibration of sp^2 carbon (E_{2g} vibration symmetry). The feature is called G band and behaves non-dispersive in well-ordered carbon materials. However, in disordered carbons the G peak shifts to higher wavelength (sometimes past 1600 cm^{-1}) thereby allowing to determine the degree of disorder [204]. Several additional Raman features appear as disorder is introduced into carbon. The most prominent feature in the first order Raman spectrum ($1000 - 1800\text{ cm}^{-1}$) is designated as D band and appears at 1350 cm^{-1} , regardless of the type of disorder. The D band is forbidden in graphite but becomes Raman active through a disorder induced double resonance Raman process [205, 206] which causes in-plane breathing vibrations of the aromatic ring structures (A_{1g} symmetry). It shows low intensities in well-organized materials but becomes dominant in more disordered systems. The G and D vibration modes are depicted in Figure 4.13. Another disorder induced Raman feature which is also assigned to a double resonance process is the so-called D' band appearing at 1620 cm^{-1} . The origin of this band still remains open to debate but is often found when nano-crystalline graphite ($L_a > 20\text{ \AA}$) is investigated [207, 208]. Besides the mentioned Raman lines additional modes may be present in the first order Raman spectrum of disordered carbon materials such as the ν_3 - and ν_1 -mode at approx. 1180 and 1520 cm^{-1} (assigned to polyolefinic chains), the D'' mode at approx. 1500 cm^{-1} (related to unorganized hexagonal aromatic ring structures, i.e. amorphous carbon) and the T band at 1150 cm^{-1} (designated to sp^3 type carbon structures).

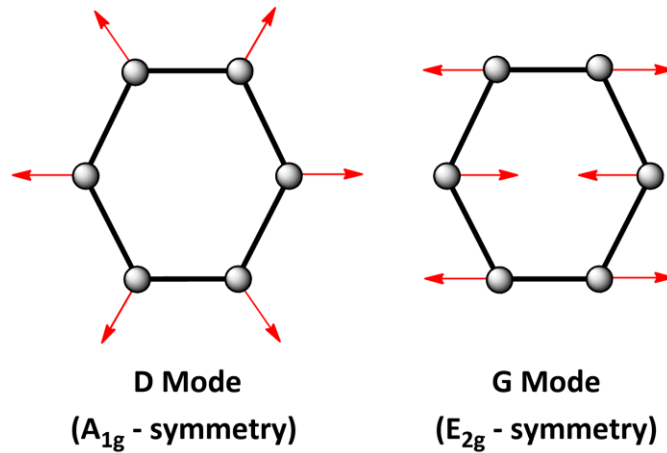


Figure 4.13: Carbon vibration in the G and D modes. The G vibration is not strictly related to aromatic structures and can also be found in polyacetylenes.

The influence of disorder can also be observed in the second order Raman spectrum indicated by several new features appearing in the region between 2200 and 3250 cm⁻¹. Two lines are observed at ~2450 and 3250 cm⁻¹ next to the 2D band and a second strong feature at 2900 cm⁻¹ which is ascribed to a combination of the D and G band and thus labeled D+G band [208].

In case of a single layer graphene, the spectrum is dominated by the already mentioned G band at 1580 cm⁻¹ and the 2D band in the range of 2500 - 2800 cm⁻¹. Going from graphene to HOPG, by increasing the numbers of graphene layers, the 2D band starts to split after 4 layers developing two new features (G'_{3DA} and D'_{3DB}) around 2700 cm⁻¹. The ratio between these two features can be used to estimate the present number of graphene layers [209].

As the Raman spectrum responds sensitive to any kind of defects, it allows to quantify the degree of disorder. Tunistra and König showed that the relative intensity ratio I_D/I_G of the D and G band in graphitic samples depends inversely on the lateral crystal size L_a, obtained from the X-ray diffraction linewidth [210]. Based on their work, Knight and White derived an empirical expression to determine L_a from the I_D/I_G ratio [211]:

$$\frac{I_D}{I_G} = \frac{C\lambda}{L_a} \quad (4.7)$$

As the I_D/I_G ratio strongly depends on the excitation wavelength λ, a wavelength-dependent coefficient C was introduced. The coefficient C can be calculated according to the relationship found by Matthews *et al.*: C_(λ) ≈ C₀ + λ·C₁, with C₀ = -12.6 nm and C₁ = 0.033, valid in the range of 400 < λ < 700 nm [212]. For a wavelength of λ = 514.5 nm a constant of C ≈ 4.4 nm is obtained. A schematic depiction of the lateral crystal size L_a is given in Figure 4.14.

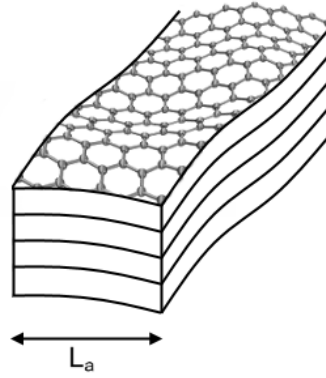


Figure 4.14: Schematically depiction of the lateral crystal size L_a .

According to the TK equation, the I_D/I_G ratio of graphite will increase with decreasing lateral cluster size L_a as the D band intensity will increase. Upon growing disorder, the sp^2 clusters begin to decrease in number and size and become more and more distorted. At this point, the D band intensity starts to decrease, as it is related to the breathing mode of aromatic ring structures causing the I_D/I_G ratio to decrease again. This results in an overestimated L_a value which is why the equation does not hold for highly distorted carbon systems. Hence, the development of a D band indicates growth and fusion of six-folded aromatic ring structures which indicates ordering of amorphous carbons, whereas in graphite the development of the D band indicates disorder. To ensure a precise determination of L_a below 2 nm, Ferrari and Robertson proposed the following correlation [213]:

$$\frac{I_D}{I_G} = C'_\lambda \cdot L_a^2 \quad (4.8)$$

with C'_λ representing a wavelength-dependent factor. However, for disordered carbons many groups have found that the lateral size L_a was best described by using the ratio of the integrated areas instead of the intensities [214]. Consequently, for disordered carbons it is more accurate to use the following equation proposed by Cancado *et al.* [215].

$$L_a = (2.4 \cdot 10^{-10}) \cdot \lambda_l^4 \cdot \left(\frac{A_D}{A_G}\right)^{-1} \quad (4.9)$$

4.2.1 Monitoring the graphitization process in SiOC/C

As already mentioned, the Raman spectroscopy is a very effective technique to follow the graphitization process within SiOC/C as it provides a wealth of information about the present carbon structures and is also capable of discerning even slight structural changes. The visible Raman spectroscopy ($\lambda = 488 - 633$ nm) is about 50 to 230 times more sensitive to sp^2 sites than to sp^3 sites, as λ energetically correspond to the $\pi-\pi^*$ transition states. Even diamond-like carbons (DLCs) containing over 90 % of sp^3 sites are hard to probe as the residual sp^2 modes

superimpose the whole Raman spectrum. By using the UV Raman spectroscopy ($\lambda = 320 - 280 \text{ nm}$), this problem can be avoided. With its higher photon energy of 4.4 - 5.1 eV, UV Raman spectroscopy excites both the π and the σ states which allows to probe sp^3 sites occurring at early stage of graphitization. However, the sensitivity for the sp^2 modes is still stronger by a factor of 5 - 10 compared to the sp^3 sites [216]. Nevertheless, the UV Raman spectroscopy does provide an equal excitation of both graphitic and olefinic components, as it excites not just the lower lying π states [217]. As all vibrations of the sp^2 carbons are induced equally, a more detailed investigation of various sp^2 structures and even to some extent of sp^3 structures are possible. Thus, the UV Raman spectroscopy is a valuable tool to follow the initial graphitization steps during the synthesis of the SiOC/C ceramic.

In the following, the graphitization process of a carbon depleted C-1 and a carbon-rich C-11 sample are examined with UV Raman. In case of the C-1 sample, the low amount of carbon allows to assess the initial carbon which segregates in the early beginning at temperatures $T < 1000 \text{ }^\circ\text{C}$ as the carbons precipitations are encapsulated and spatially separated by the ceramic network. In contrast, the precipitations in the C-11 sample already show first signs of graphitic order. Both UV Raman spectra are compared in Figure 4.15.

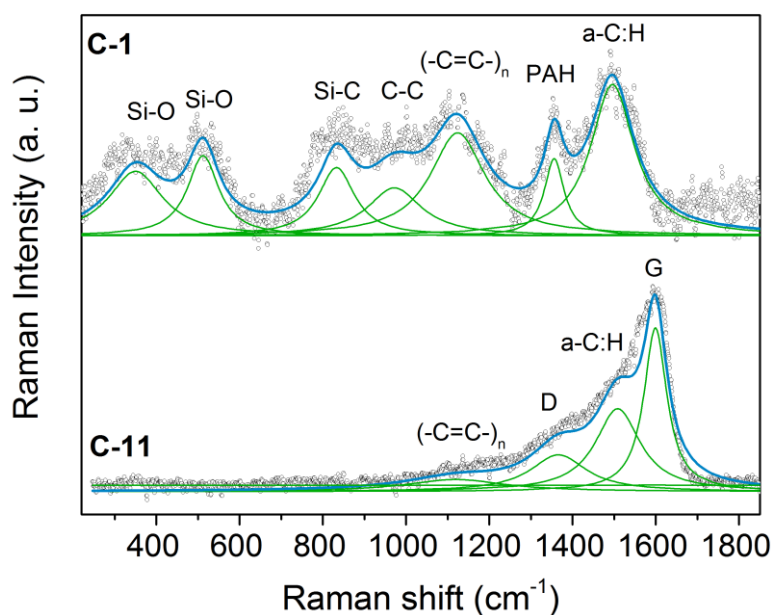


Figure 4.15: Comparison of the UV Raman spectra of C-1 and C-11 sample prepared at $T = 1000 \text{ }^\circ\text{C}$.

The C-1 sample does not exhibit any typical resonances of graphitic (1580 cm^{-1}) or diamond-like carbon (1333 cm^{-1}). Therefore, the signals at wave numbers $> 1000 \text{ cm}^{-1}$ are considered to belong to non-graphitic carbon. The most prominent feature at 1500 cm^{-1} can be attributed to the E_{2g} mode (G band) of amorphous carbon where conjugated sp^2 bonds (ring- and chain-like structures) coexist with sp^3 single bonds. According to the elemental analysis, the C-1 sample contains significant amounts of hydrogen ($\approx 24 \text{ mol.}\%$), suggesting that amorphous

hydrogenated carbon (a:C-H) is formed. The band at 1115 cm^{-1} indicates the presence of polyacetylene $(-\text{CH}=\text{CH}-)_n$ with chain lengths in the order of $n \approx 10$ [218]. Configurational and conformational deformation leads to the strong broadening of the Raman signal. Small polycyclic aromatic hydrocarbons (PAHs) are identified by the signal at 1360 cm^{-1} and the C-C single bonds (sp^3) by the signal at 980 cm^{-1} . Finally, the broad resonances appearing at 345 , 510 and 830 cm^{-1} correspond to the glassy $\text{Si}_x\text{O}_y\text{C}_z$ network (Si-O, Si-O and Si-C). The Raman spectrum of the C-11 sample, in contrast, is dominated by a strong G feature at 1580 cm^{-1} and a weak D mode which can be attributed to nano-graphitic carbon. In between these two signals lies the resonance of a:C:H. The signal of polyacetylene $(-\text{CH}=\text{CH}-)_n$ is also present, but its intensity is much lower as their concentration has already declined at the expense of nano-crystalline graphite. Interestingly, no Raman features of the $\text{Si}_x\text{O}_y\text{C}_z$ matrix are found in C-11 which is probably due to the much greater intensity of the present sp^2 features dominating the Raman spectrum.

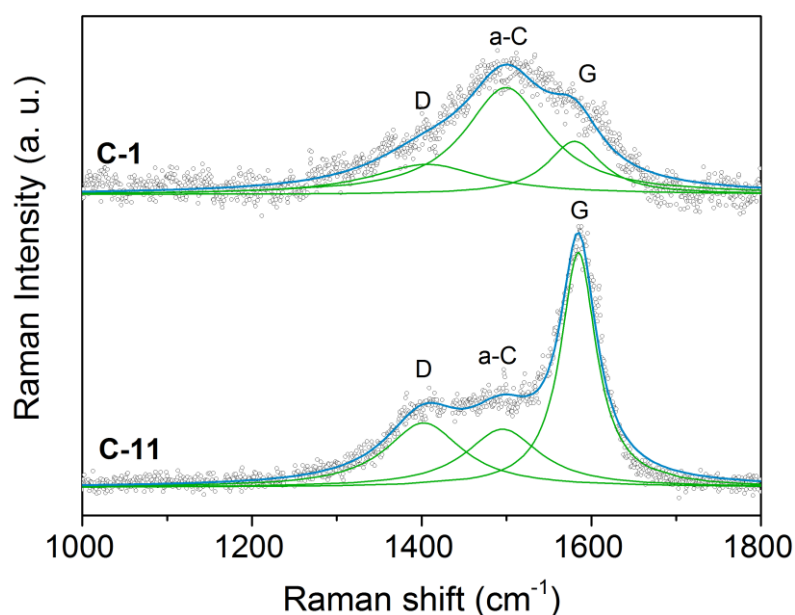


Figure 4.16: Comparison of the UV Raman spectra of C-1 and C-11 sample prepared at $T = 1400\text{ }^\circ\text{C}$.

Raising the pyrolysis temperature up to $T = 1400\text{ }^\circ\text{C}$ results in a more ordered carbon, as shown in Figure 4.16. In both spectra, the features below 1300 cm^{-1} have vanished leaving only the typical sp^2 carbon signals i.e. D ($\approx 1400\text{ cm}^{-1}$), a-C ($\approx 1500\text{ cm}^{-1}$) and G ($\approx 1600\text{ cm}^{-1}$) with different relative intensities. In case of the C-1 sample, a weak G and D mode appeared at the expense of the olefinic chains and PAHs, whereas a strong resonance of a-C remains. As supported by elemental analysis, the change in the carbon microstructure results from the loss of hydrogen at temperatures in the range of $T = 1000 - 1250\text{ }^\circ\text{C}$: breaking up the C-H bonds which promotes the formation of aromatic sp^2 bonded carbon. Nevertheless, the strong feature of a-C still indicates an early stage of graphitization. The UV Raman spectrum of the C-11

sample is comparable with the spectrum at $T = 1100\text{ }^{\circ}\text{C}$ with only slight changes such as the vanished signal of the olefinic chains and the grown intensity of the D mode. By comparing the two Raman spectra, graphitic domains appears to form more easily in carbon-rich samples and the transformation to nano-crystalline graphite can be regarded as finished when the a-C signal disappears.

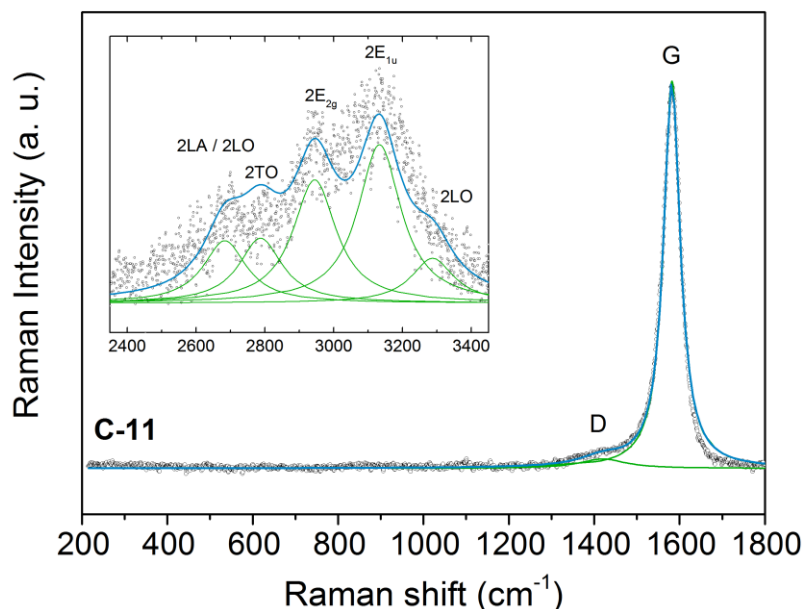


Figure 4.17: UV Raman spectra of sample C-11 prepared at $1600\text{ }^{\circ}\text{C}$. The inset shows the second order UV Raman spectrum.

Figure 4.17 presents the UV Raman spectra of C-11 pyrolyzed at $T = 1600\text{ }^{\circ}\text{C}$. The band attributed to a-C has faded and the characteristic UV Raman bands of graphitic carbon are present: the G band at 1580 cm^{-1} and the complex signal at $\approx 3000\text{ cm}^{-1}$ due to the double resonance scattering. The inset in Figure 4.17 displays the deconvolution of the latter signal. The peak positions of the fitted lines are in excellent agreement with the literature UV Raman data for graphite with the only remarkable difference being the broadening of the Raman lines (by a factor of ≈ 5) which very likely arises from the higher distortion of graphite within the glassy matrix. Note that the obtained data rule out graphene as carbon component, as the UV Raman spectrum of graphene shows a less marked signal structure, i.e. fewer peaks are observed in the range of $2600\text{ to }3400\text{ cm}^{-1}$. The weak but still visible D peak and the change in the full width half maximum (FWHM) of the G band also hint at non-ideal graphite. The FWHM exceeds the value of highly-ordered graphite by far ($\text{FWHM}_{\text{HOPG}} = 10\text{ cm}^{-1}$) and decreases only slightly from 51 cm^{-1} ($T = 1400\text{ }^{\circ}\text{C}$) to 47 cm^{-1} ($T = 1600\text{ }^{\circ}\text{C}$). This also applies for the G band of the C-1 sample with a FWHM of 45 cm^{-1} at $T = 1600\text{ }^{\circ}\text{C}$. Consequently, the transformation of amorphous carbon to nano-crystalline carbon at $T > 1400\text{ }^{\circ}\text{C}$ is seen in the Raman spectrum of C-1 and C-11 by the decrease of the a-C signal and the appearance and increase of the G band.

Upon further thermal annealing to $T = 1600\text{ }^{\circ}\text{C}$, the nano-crystalline carbon phase gradually transforms into disordered graphite-like carbon. In agreement with previous TEM studies,[183] the obtained results suggest the presence of turbostratic carbon within the silica matrix and do not support the model description of carbon as a network of single layer graphene bonded to silica $\text{SiO}_m\text{C}_{4-m}$ tetrahedra [30].

4.2.2 Characterization of the segregated carbon phase by Vis Raman

Figure 4.18 displays the visible Raman spectrum ($\lambda = 514\text{ nm}$) of a C-11 sample heat treated at different temperatures. It can be easily noted, that the evolution of the spectrum reflects the advancing graphitization within the sample. For the least ordered sample at $T = 1000\text{ }^{\circ}\text{C}$, two broad signals representing the D and G band, along with a very broad signal at 1120 cm^{-1} (T band) are obtained. No spectral changes are observed until the thermal treatment is increased up to $T = 1400\text{ }^{\circ}\text{C}$. Hereby, the T band, induced by residual sp^3 carbon, vanishes and the FWHM of the D band significantly narrows along with an increasing intensity. The width and intensity of the G band stays constant but a small shoulder around 1620 cm^{-1} starts to develop. The occurred D' band supports the evolution of small nano-graphitic clusters which is also substantiated furthermore by the development of two signals (2D and D+G) in the second-order spectrum.

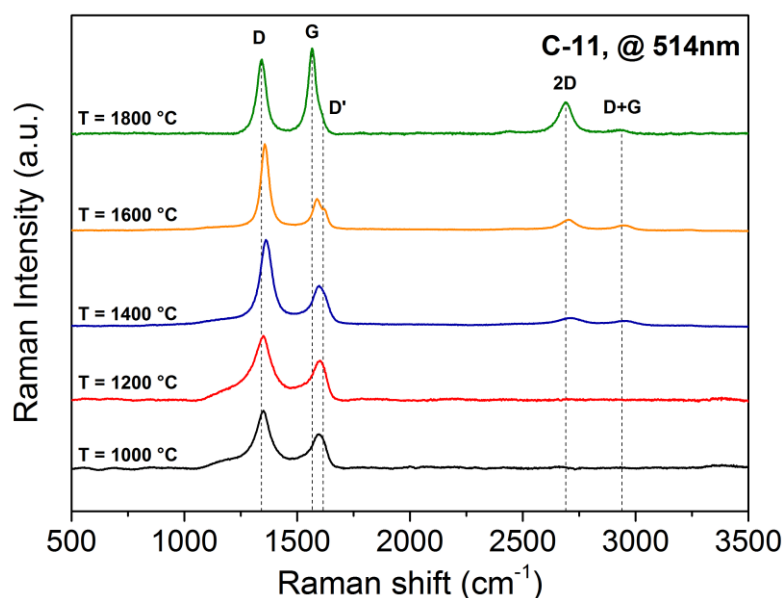


Figure 4.18: Evolution of the Raman spectrum obtained at $\lambda = 514\text{ nm}$ for C-11 samples heat-treated at different temperatures ($1000 < T < 1800\text{ }^{\circ}\text{C}$).

With increasing crystalline order, the D band continues to narrow and the D' band becomes more and more pronounced together with a displacement of the G band towards lower wavelengths. Although the advancing graphitization does not increase the intensity of the G

band, the two signals in the second-order spectrum clearly improve their intensity. In the final spectrum at $T = 1800\text{ }^{\circ}\text{C}$ the intensity of the G band is notably increased and the wavelength is downshifted by 30 cm^{-1} , with the D' band remaining as a small shoulder. In addition, the second-order spectrum markedly differs from the previous ones as the band at 2700 cm^{-1} has apparently grown in intensity and is displaced by 15 cm^{-1} to lower wavelength. According to Pimenta *et al.*, the shape and shift of this band resembles turbostratic stacking of several graphene sheets along the c-axis as the width of the feature ($w = 77\text{ cm}^{-1}$) is notably larger than that of monolayer graphene ($w = 24\text{ cm}^{-1}$) [219]. The progressive changes in the Raman spectrum represent the current intermediate stages during the transition from amorphous to nano-crystalline and eventually to turbostratic micro-crystalline carbon. The spectral parameters for the characteristic first-order Raman spectrum are given in Table 4.3.

Table 4.3: Summary of the features present in the first-order Raman spectrum of C-11.

C-11	ν_T (cm^{-1})	A_T (cm^{-1})	ν_D (cm^{-1})	A_D (cm^{-1})	ν_G (cm^{-1})	A_G (cm^{-1})	$\nu_{D'}$ (cm^{-1})	$A_{D'}$ (cm^{-1})	A_D/A_G
1000 $^{\circ}\text{C}$	1204	10.7	1348.9	117.2	1593.1	51.2	-	-	2.3
1200 $^{\circ}\text{C}$	1193	12.1	1348.6	107.6	1594.7	42.1	-	-	2.5
1400 $^{\circ}\text{C}$	-	-	1349.2	119.8	1597.2	54.6	1623.7	2.1	2.2
1500 $^{\circ}\text{C}$	-	-	1354.8	93.7	1597.3	40.8	1624.3	4.3	2.2
1600 $^{\circ}\text{C}$	-	-	1350.6	77.1	1581.6	48.3	1625.0	4.6	1.59
1800 $^{\circ}\text{C}$	-	-	1342.9	48.6	1563.4	56.5	1611.8	1.8	0.86

The elimination of defects and the growth in crystalline size is also reflected by the change of the FWHM of the D and G band depicted in Figure 4.19. Both features possess a broad signal up to $T = 1200\text{ }^{\circ}\text{C}$ which is mostly caused by different carbon species within the amorphous carbon phase, such as PAHs, polymeric chains, sp^3 carbon and defective nano-graphite. Especially, the D band reacts sensitive to this kind of non-graphitic structures as they enable its Raman vibration mode. With increasing thermal treatment beyond $T > 1350\text{ }^{\circ}\text{C}$, the SiOC matrix starts to separate into SiO_2 and SiC. The separation process promotes clustering of the spatially separated carbon domains which themselves continues to accumulate at the expense of residual sp^3 carbon and olefinic chains. However, the resulting carbon phase is still of highly defective nature and far from being well-ordered.

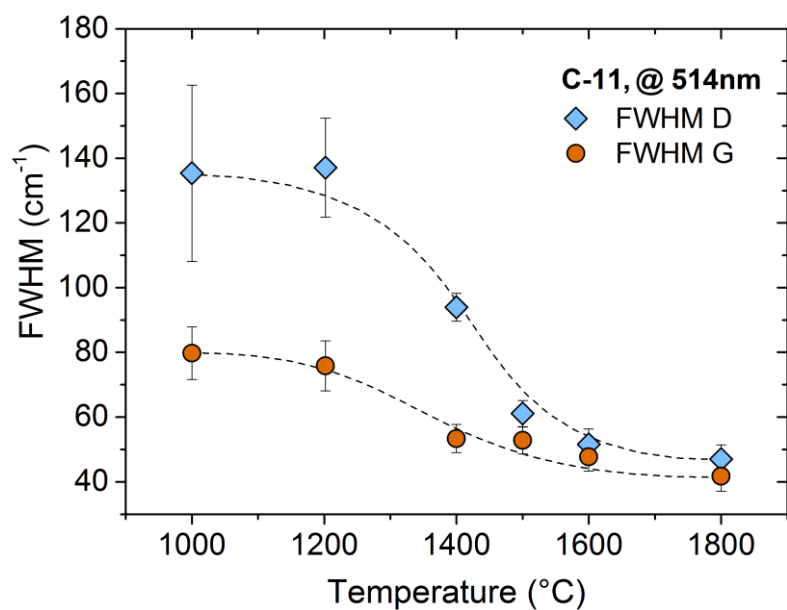


Figure 4.19: Progressive change of the FWHM of the D and G band upon thermal treatment.

The existence and the relative small drop of the G band compared to the degression of the D band supports the assumption that, when the amount of carbon is sufficient enough, the nano-graphitic core structures are almost present at $T = 1000\text{ }^{\circ}\text{C}$ [220]. Upon further heating, the internal lattice defects of the graphitic crystals slowly starts to vanish resulting in a decline of the G linewidth. The accompanied decline of the D width mirror the rearrangement of the surrounding and the eradication of intrinsic defects. At $T = 1800\text{ }^{\circ}\text{C}$ the width of the D and G band lies around $w = 50\text{ cm}^{-1}$ which corresponds to the width of microcrystalline graphite ($w_D = 66.6$; $w_G = 59.9$) and glassy carbon ($w_D = 52.7$; $w_G = 56.1$) whereas the segregated carbon at $T = 1000\text{ }^{\circ}\text{C}$ resembles coke ($w_D = 149.1$, $w_G = 79$) [221]. Nevertheless, even after the highest temperature treatment a high amount of intrinsic defects remains represented by the intense D band.

Figure 4.20 shows the lateral crystal size L_a and its progress with increasing thermal treatment calculated according to Equation 4.9. From the graph it can be derived that the lateral crystal size is not affected up to $T = 1500\text{ }^{\circ}\text{C}$ and only slightly varies around a value of $L_a = 7.5\text{ nm}$. This is supported by the work of Takai *et al.* who obtained similar values ($L_a = 5 - 7\text{ nm}$) for an amorphous carbon film heat treated in the temperature range up to $T = 1500\text{ }^{\circ}\text{C}$. At higher temperatures, the crystalline lattice starts to grow as the intrinsic lattice defects are removed. The onset of graphitization is emphasized by the increase in intensity of the G band and the clear development of D' at $T = 1600\text{ }^{\circ}\text{C}$, see Figure 4.18.

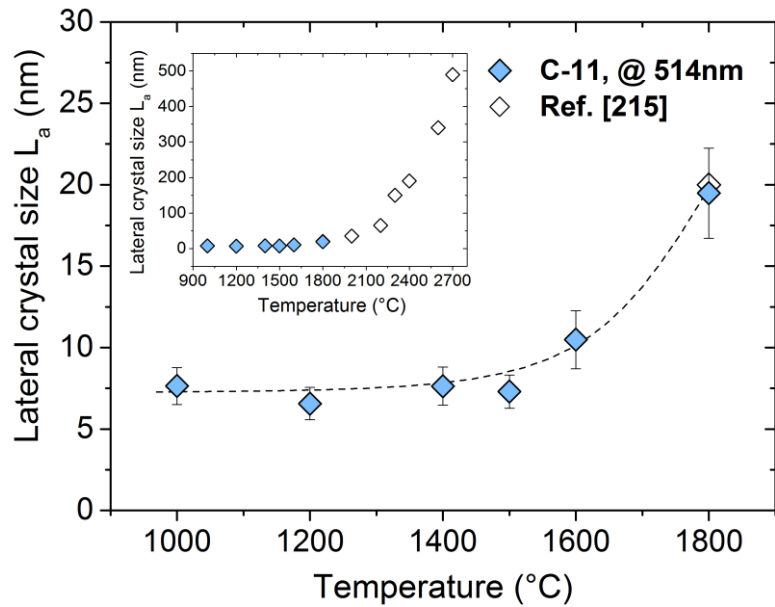


Figure 4.20: Dependency between the lateral crystal size L_a and the thermal treatment. The open data points in the inset represent the work of Ref. [215].

Similar findings but at a much higher temperature readings were published by Cancado *et al.* who investigated the graphitization behavior of diamond-like carbon thin films [215]. Their results are given by the empty dots in the inset of Figure 4.20. According to their XRD measurements a L_a value of $L_a = 20$ nm is obtained after a thermal treatment of $T = 1800$ °C which is in perfect agreement with the L_a value found in the SiOC/C sample. Although higher thermal treatment promotes graphitization, it also supports the degradation of the SiOC network due to the carbothermal reaction (Equation 2.3). Therefore, the samples are prepared at $T = 1600$ °C resulting in smaller graphitic crystals with a size of $L_a = 10 \pm 2$ nm.

To verify if the amount of segregated carbon also affects the lateral size of the graphitic crystallites, several SiOC/C samples with varying amounts of carbon were investigated. The results are depicted in Figure 4.21 and reveal a constant lateral crystal size of $L_a = 9 \pm 1$ nm for samples with a carbon content above $\phi_C > 10$ vol.%. In case of lower carbon contents, ($\phi_C < 10$ vol.%) smaller crystallites in the range of $L_a = 6 \pm 2$ nm are obtained. The observed trend supports the earlier postulated assumption that the formation of nano-crystalline graphite is promoted in carbon-rich samples.

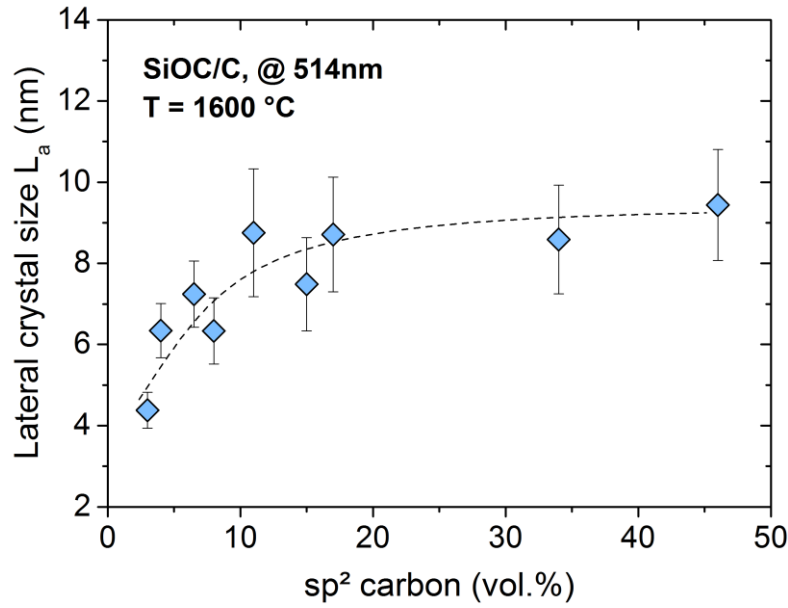


Figure 4.21: Plot of the lateral crystal size L_a as a function of the amount of carbon.

The evolution of disorder within the graphitic crystals can also be characterized as a function of the average distance between defects L_D and the ratio A_D/A_G . The average distance is calculated according to the following equation 4.10 [222]. Figure 4.22 depicts the obtained L_D values of C-11 together with an Ar^+ ion bombarded graphene layer as reference.

$$L_D^2 = 1.8 \cdot 10^{-9} \cdot \lambda_L^4 \cdot \left(\frac{A_D}{A_G}\right)^{-1} \quad (4.10)$$

As can be seen in Figure 4.22, the A_D/A_G ratio of the graphene layer increases linearly up to a maximum value of $A_D/A_G \approx 3.2$. The rising A_D/A_G ratio resembles ordering of the defective crystallites which are initially too small to contribute to the Raman spectrum. As the Ar^+ ion dose is constantly reduced, less defective crystallites are produced, causing the A_D/A_G ratio to increase to its maximum. The subsequent decrease of the A_D/A_G ratio, is caused by further ordering of the crystallites and the accompanied decreasing D band. A similar behavior was observed by Ferrari *et al.* who divided the course of the ratio A_D/A_G according to the crystalline size L_a into stage 1: high defect concentration $I_D/I_G = 1/L_a^2$ and stage 2: low defect concentration, $I_D/I_G = 1/L_a$. They proposed that the TK Equation 5.1 is only valid in stage 2 and breaks down below $L_a < 2$ nm. The transition is usually observed in the range of $A_D/A_G \approx 3$ at $\lambda = 514$ nm which corresponds to the course in Figure 4.22. With regards to C-11 the calculated values follow the decline of the A_D/A_G ratio with increasing crystalline order as the thermal treatment is raised. At $T = 1000$ °C a L_D value of 6 nm is obtained which means that within the average lateral size of the crystallite ($L_{a, 1000\text{ °C}} = 7.5$ nm) at least one defect is present. By increasing the temperature up to $T = 1400$ °C, L_D expands giving values in the range of $L_D = 8 - 10$ nm. This results in the development of the D' band as it resembles nano-graphitic

structures. Upon higher heat treatment, the intrinsic defects are further reduced giving rise to higher L_D and L_a values.

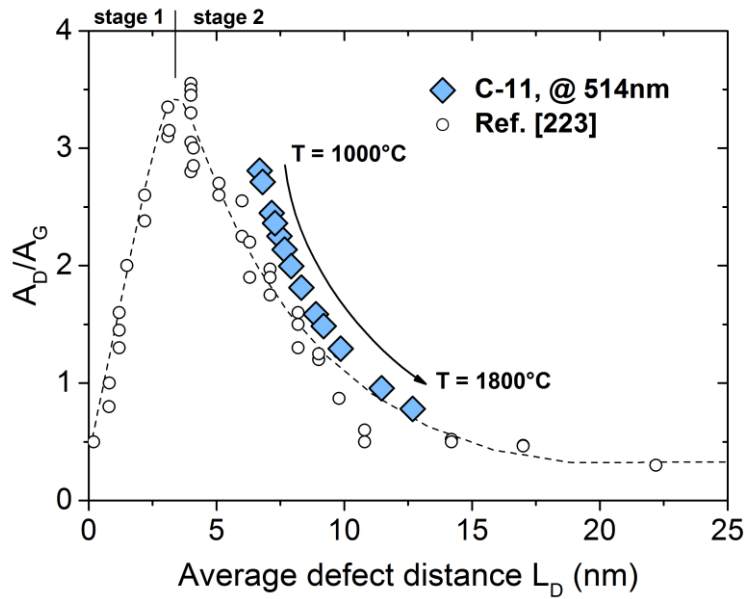


Figure 4.22: Evolution of the average distance between defects L_D within the carbon of SiOC/C synthesized at different temperatures. The empty dots represent Ar^+ ion bombarded graphene [223].

Additional information about the nature of the present defects can be derived from the disorder-activated features in the Raman spectrum. In general, one refers to defects in graphitic materials as anything that breaks the symmetry of the honeycomb lattice causing the D band to appear. Different kind of defects can be defined such as edges, grain boundaries, vacancies, implanted atoms and different carbon hybridization. A systematic study to investigate the influence of the respective defects in graphitic material was performed by Eckmann *et al.*, see Figure 4.23 [224]. They plotted the intensity ratio I_D/I_G versus $I_{D'}/I_G$ following the disorder trajectory. Figure 4.23 reveals that for each individual type of defect a specific slope is obtained. According to their work, sp^3 hybridized graphene exhibits a slope of $I_D/I_{D'} \approx 13$, vacancies within defective graphene revealed a slope of $I_D/I_{D'} \approx 7$ and the smallest slope with $I_D/I_{D'} \approx 3.5$ is obtained for graphite with different grain sizes. As the slope is not dependent on the defect concentration, it can be used to determine the dominant nature of defects. Note that for carbon-rich samples ($\phi_C > 17$ vol.%) the D' peak starts to merge with the G peak making it is difficult to separate the individual contributions of the G peak and D' peak. The linear fit of the obtained data reveals a slope of $I_D/I_{D'} \approx 6.5$ which implies that the dominating nature of defects, for SiOC/C pyrolyzed at $T = 1600^\circ\text{C}$, are vacancies and interstitial defects within the nano-crystalline carbon lattice [225].

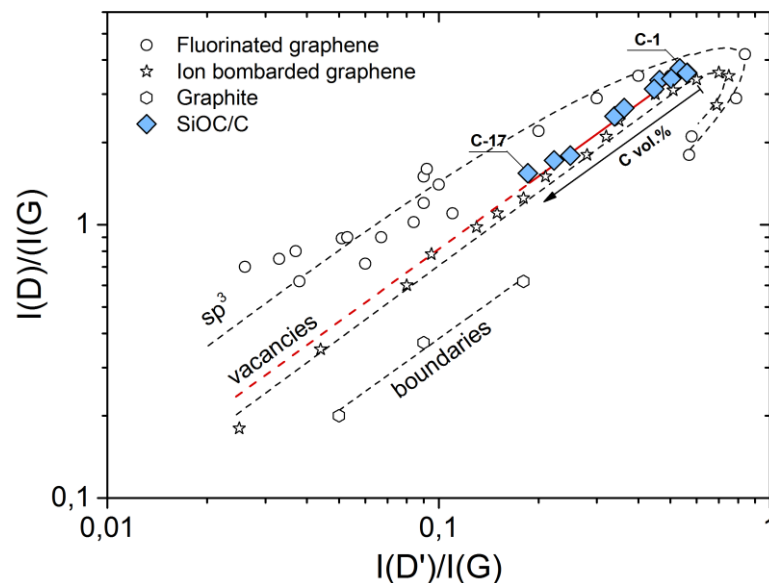


Figure 4.23: I_D/I_G versus ratio $I_{D'}/I_G$. Data from literature is represented by open symbols [224].

It is not surprising that point-defects are found to be the dominant species as the UV Raman measurements have already proven that neither sp^3 defects nor graphene-like boundaries are present in samples prepared at $T = 1600\text{ }^\circ\text{C}$. Therefore, one can state that, the nature of defects in SiOC/C is not controlled by the amount of carbon, but rather thermodynamically by the applied temperature during the synthesis.

4.2.3 Summary

Two distinct well-defined types of carbon are generally assigned according to their graphitization behavior: graphitizing and non-graphitizing carbons [77]. In non-graphitizing carbons, no trace of developed graphitic structure can be detected even after heating to $T = 3000\text{ }^\circ\text{C}$. For graphitizing carbons, on the contrary, graphitization sets in at about $T \approx 1700\text{ }^\circ\text{C}$ and rapidly increases with increasing temperature. According to the Raman results presented in this chapter, the segregated carbon in SiOC/C starts to graphitize around $T = 1600\text{ }^\circ\text{C}$ and therefore can be assigned to the class of graphitizing carbons. In general, the initial carbon segregating at $T \leq 1000\text{ }^\circ\text{C}$ is being best described as an amorphous mixture of chains, PAHs, nano-graphitic clusters and residual sp^3 carbon as supported by the UV Raman data. With increasing thermal treatment and the accompanied phase separation of the amorphous SiOC matrix, the spatial separated carbon structures continue to aggregate at the expense of the residual amorphous carbon. Figure 4.24 schematically depicts a cutout of a nano-crystalline graphite at low temperature/high disorder. It consists of several carbon layers with a lateral crystal size of $L_a \approx 10\text{ nm}$. The layers are oriented in a turbostratic manner with a locally preferred parallel orientation. Tilt and twist boundaries/defects exists within each layer

forming wrinkled graphene-like sheets. These defects are assumed to be responsible for the strong D feature present in the Vis Raman spectra.

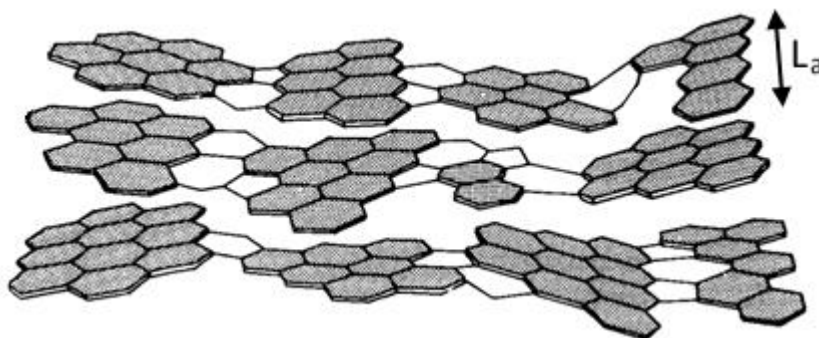


Figure 4.24: Schematic depiction of a nano-crystalline cluster taken from Ref. [226].

The defects are spatially separated by an average distance of $L_D = 7$ nm (at $T = 1600$ °C). The lateral crystal size of the carbon layer remains almost constant up to $T = 1600$ °C. Upon further thermal treatment ($T = 1800$ °C) L_a increases strongly and reaches values similar to those of Cancardo *et al.* ($L_a = 20$ nm) who investigated the graphitization of DLC-films [215]. Even at the highest synthesis temperature ($T = 1800$ °C) a strong D feature remains in the Raman spectra indicating that the carbon phase in SiOC/C is still highly defective as most carbons need temperatures in the range of 2000 - 2500 °C to delete the defects. Therefore, the segregated carbon phase in SiOC/C can be best described as an intermediate stage between glassy and graphitic carbon.

4.3 Electrical properties of SiOC/C

This chapter focuses on the electrical properties of SiOC/C. To gain further insight, Hall measurements and temperature-dependent impedance spectroscopy were conducted. The dc conductivity values were derived through extrapolation of the lowest frequency ($\nu = 0.01$ Hz) to the x-axis intersection. A semicircle, which decreases in size with increasing temperature, is obtained for all SiOC/C samples synthesized at temperatures below $T < 1600$ °C, regardless of the amount of carbon. In contrast, samples synthesized at $T = 1600$ °C showed carbon dependent impedance spectra with either ohmic resistance, obtained for samples with a high carbon content ($\phi_c > 10$ vol.%), or a single semicircle for samples with a lower carbon content. As main result of the impedance measurements no sign of second contribution to the conductivity (contact or matrix dependent resistance) is observed in the most extensively investigated samples prepared at $T = 1600$ °C. Since the bulk resistance obtained from the impedance spectra equals the dc resistance only dc data are reported in the following.

4.3.1 Resistance change with graphitization

PDCs develop a (segregated) carbon phase with pyrolysis which exerts a major influence on the electrical properties [51, 165, 191, 227]. As the concentration and hybridization of carbon in SiOC/C is strongly influenced by the initial polymer composition as well as the pyrolysis condition (temperature, atmosphere and holding time), the resulting PDC ceramic can be progressively changed from an insulator to a semiconductor and semimetal. The electrical properties therefore represent a sensitive measure of the state of carbon during preparation and provide valuable information on the graphitization process.

Figure 4.25 depicts the room temperature conductivity of sample C-11 and C-17 synthesized at $T = 1200 - 1800\text{ }^\circ\text{C}$. Literature data of glassy carbon are added for comparison [55]. Both samples exhibit semiconductive behavior with values between $\sigma = 10^{-4} - 10^{-2}\text{ }(\Omega\cdot\text{cm})^{-1}$ at $T > 1400\text{ }^\circ\text{C}$. The increase in σ observed for C-11 and C-17 around $T = 1300 - 1400\text{ }^\circ\text{C}$ is due to the change in porosity during densification of the sample. Therefore, only σ values obtained at $T > 1400\text{ }^\circ\text{C}$ represent the bulk conductivities of C-11 and C-17. The higher conductivity of C-17 is caused by the higher amount of segregated carbon.

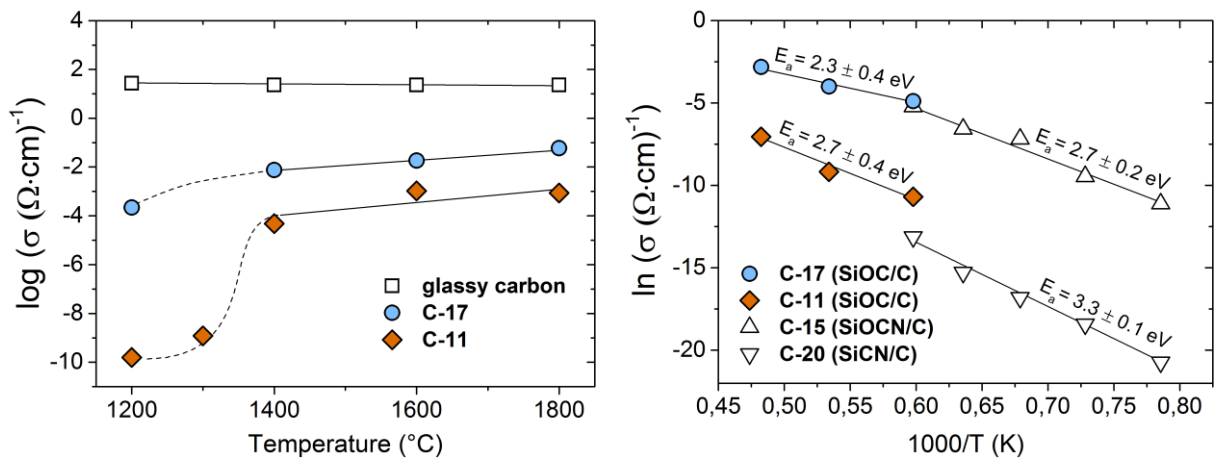


Figure 4.25: Effect of heat-treatment temperature on the RT-conductivity of C-11, C-17. Literature data is taken from Ref. [53, 228].

The activation energies E_a for the electrical transport in C-11 and C-17 ($2.7 \pm 0.4\text{ eV}$; $2.3 \pm 0.4\text{ eV}$), representing the energy for graphitization, are consistent with literature data of other PDC systems and are in accordance with the graphitization energy found in amorphous carbon (3.3 eV , [229]).

4.3.2 Percolation in SiOC/C

The carbon distribution in low conducting and highly conducting samples is schematically depicted in Figure 4.26. Assuming an ideal two components system (non-interacting phases)

the conductivity will be given by the volume fractions ϕ_i and the partial conductivities σ_i of the two components: $\sigma_{\text{total}} = \sigma_{\text{glass}} \cdot \phi_{\text{glass}} + \sigma_{\text{carbon}} \cdot \phi_{\text{carbon}}$. In both cases the overall conductivity is determined by the carbon phase since σ_{carbon} is by orders higher than σ_{glass} .

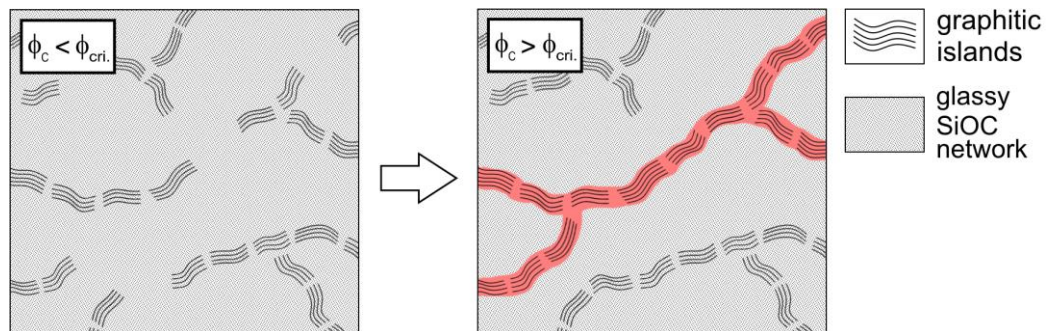


Figure 4.26: Schematic depiction of the carbon distribution within SiOC/C.

Increasing the carbon volume fraction ϕ_C may lead to a percolation type conductivity. Below the critical volume fraction ϕ_{cri} , no continuous path for the charge transport exists whereas above ϕ_{cri} , the charge carriers can be transported efficiently without restriction along the carbon path. Figure 4.27 shows the (logarithmic) room-temperature dc conductivity of the SiOC/C samples with carbon concentrations $\phi_C = 1 - 43$ vol.% synthesized at $1100 < T < 1600$ °C. Based on the Raman data (Chapter 4.2) carbon is mainly sp^2 hybridized. Therefore, the carbon concentration is expressed as the sp^2 volume fraction. The critical concentration (percolation threshold) varies from about 20 – 6 vol.% sp^2 carbon depending on the synthesis temperature. At this concentration the conductivity changes by order of magnitude due to the transition from insulating to semiconducting / almost semimetallic SiOC/C. It is tempting to attribute the decrease of the percolation threshold to an increase in the aspect ratio of the segregated carbon phase, as the threshold depends on the shape of the conductive filler in many composite materials [230-232]. However, no reliable information on the aspect ratio can easily be obtained for SiOC/C, due to the random 3D carbon morphology and the lack of suitable characterization methods. Hence, Cordelair *et al.* computed the insulator-conductor transition in SiOC/C showing that the threshold decreased from 20 to 5 vol.% when the shape of the conductive filler was changed from spherical to rod-like carbon precipitations, see Figure 2.4 [49].

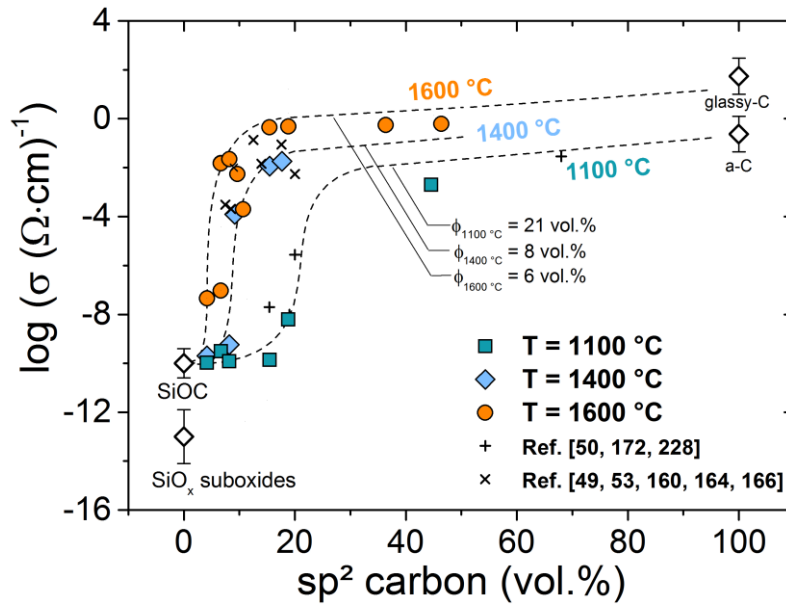


Figure 4.27: The electrical conductivity of SiOC/C as a function of the sp^2 carbon for three different temperature series. Literature values are added for the sake of comparison.

According to the Raman data carbon mainly exists as a sp^2 network. Even for the C-1 sample the network carbon dominates over the smaller aromatic structures (PAHs, polyacetylene), see Figure 4.15, raising doubts about the importance of well-defined geometrical conductive fillers used in the proposed model. The observed shift in $\phi_{cri.}$ may also be caused by changes in the carbon network itself, e.g. the loss of defects and the resulting better alignment of carbon sheets allowing enhanced electrical transport in conjugated bonds. A further sign that geometrical aspects are less important for the percolation in SiOC/C is given by the critical exponent t derived from the $\ln(\sigma/\sigma_0)$ versus $\ln(\phi - \phi_{cri.})$ plot (Figure 4.28). The value for the critical exponent derived from Equation 2.4

$$\sigma_C = \sigma_0 \cdot (\phi_C - \phi_{cri.})^t \quad (2.4)$$

differs strongly from the (solely geometrically defined) universal value of 2 for three-dimensional systems.

For SiOC/C prepared at $T = 1600$ °C with a critical volume concentration of 6 vol.% a value of $t = 4.3$ is obtained which is very similar to that of $RuO_2/silica$ ($t = 3.8$), a well-known fine dispersed composite. Non-universal behavior is frequently observed in dispersed composites, whereas universal behavior is seen more often in clustered samples [46]. The non-universal behavior may result from tunneling/hopping processes between two adjacent conductive particles [233], e. g., taking quantum mechanics into account the critical exponent becomes dependent on the mean tunneling distance and in principle does not obey any upper limit.

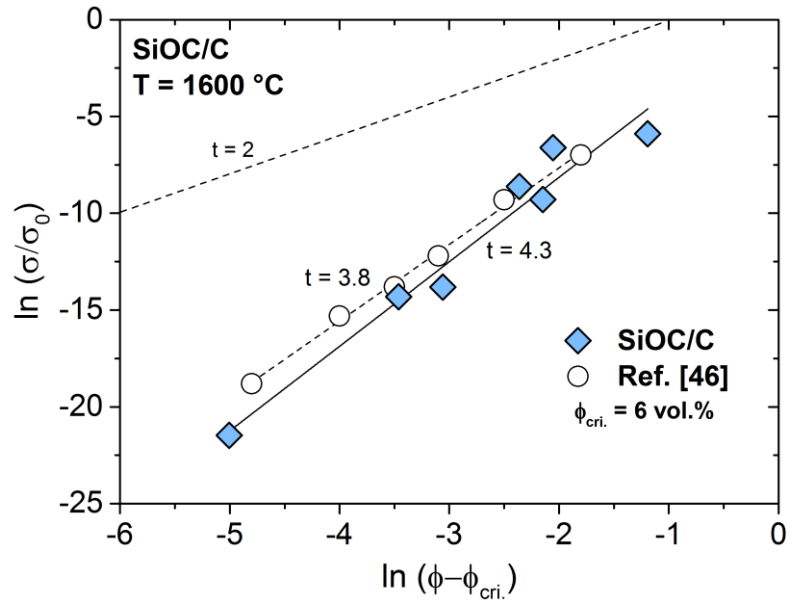


Figure 4.28: Electrical conductivity as a function of sp^2 carbon concentration. The solid line represents the fit from Equation 2.4. The upper dashed line represents the universal behavior with a slope of $t = 2$.

4.3.3 Conduction mechanism in SiOC/C

A broad range of different carbon microstructures can be present in SiOC/C ceramics depending on the synthesis conditions. Consequently, it covers a wide range of electronic properties. At one extreme, the electronic conduction approximates that of graphite, whereas on the other extreme, the present carbons can be considered as an inhomogeneous mixture of partially polymeric molecules encapsulated by an insulating silica-near matrix. In between these two extremes, disorder of various kinds modifies the electronic structure in several ways.

The most comprehensive description of the electrical properties of amorphous materials like SiOC/C was given by Mott and Elliot (see chapter 2.2.2) [86, 234]. They describe the conduction in strongly disordered systems with localized states at the tails of the valence and conduction bands as well as midgap states at the Fermi level. Two hopping mechanisms are discussed: the nearest neighbor hopping (NNH) mechanism within the tail states and the variable range hopping mechanism (VRH) near the Fermi level. The latter hopping mechanism is distinguishable from the other conduction mechanisms by its different temperature dependence: $\log \sigma \approx T^{-1/4}$ at low temperatures (typically $4 < T < 300 \text{ K}$). With increasing temperature the hopping regime changes into the Arrhenius type conduction mechanism ($\log \sigma \approx T^{-1}$). Therefore, the thermal dependence of the conductivity is an effective and informative electrical property providing information about the present conduction mechanism. In case of electrons or holes as majority carriers hopping in localized states can occur as depicted in Figure 4.29a) and Figure 4.29b).

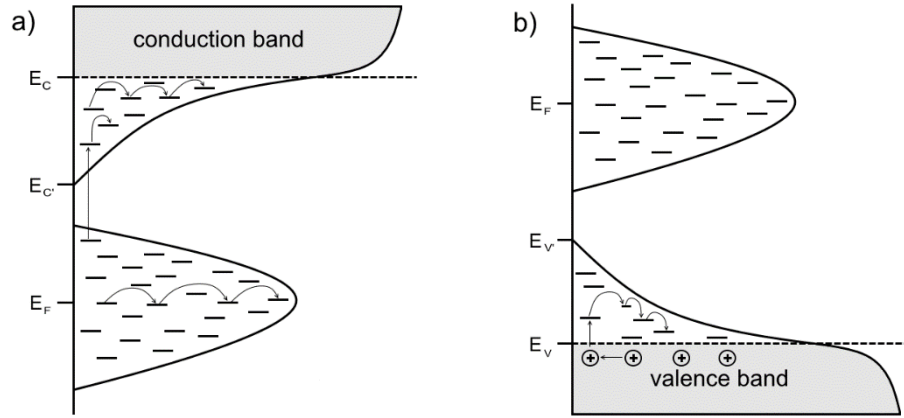


Figure 4.29: Schematically depiction of the electronic transport of a) electrons and b) holes within the localized states.

Only few information about the conduction mechanism in PDCs is available in literature. Haluschka and Engel report on SiCN/C ($\phi_c = 5$ vol.%) and SiOC/C ($\phi_c = 12$ vol.%) prepared at $T = 1500$ °C and $T = 1300$ °C [51, 235]. Both authors interpreted their data within the VRH model. A $T^{-1/4}$ dependency was found up to $T = 800$ °C. Haluschka *et al.* could further prove, that the conduction occurs by phonon-assisted hopping near the Fermi-energy and not near the mobility edges. Engel estimated the density of states near the Fermi energy to be between $N = 10^{17} - 10^{19} \text{ eV}^{-1}\text{cm}^3$ by assuming a localization length of $\alpha^{-1} = 10$ Å common for amorphous semiconductors. Ma *et al.* investigated SiCN/C ($\phi_c = 22$ vol.%) claiming nearest neighbor hopping also called band tail hopping (BTH) as transport mechanism on account of the correlation between the parameters σ_0 and T_0 in the general equation for transport in localized states [228]:

$$\sigma = \sigma_0 \cdot \left[- \left(\frac{T_0}{T} \right)^{1/\beta} \right] \quad (4.11)$$

Figure 4.30 shows the Arrhenius plot of C-11 prepared at temperatures between $T = 1000 - 1600$ °C. Above $T > 1400$ °C a linear dependency of σ with T^{-1} is evident indicating activated transport with $E_a = 0.23$ eV and $E_a = 0.04$ eV whereas below that temperature a non-linear behavior is observed. Plotting the low temperature data against $T^{-1/\beta}$ ($\beta = 3, 4$) yields no clear evidence of non-Arrhenius behavior. Assuming activated transport for the $T = 1000$ °C and $T = 1200$ °C samples two different activation energies, see Figure 4.30, may therefore occur, due to two different contributions to the conductivity. However, one can not rule out that both VRH and thermally activated transport exist in this temperature range. Further measurements are needed for clearance. The decreasing activation energies with increasing synthesis temperature indicate the continuous reduction of the band gap, since for the highest synthesis temperature ($T = 1600$ °C) the activation energy is comparable to that of glassy carbon ($E_a = 0.03$ eV [59]).

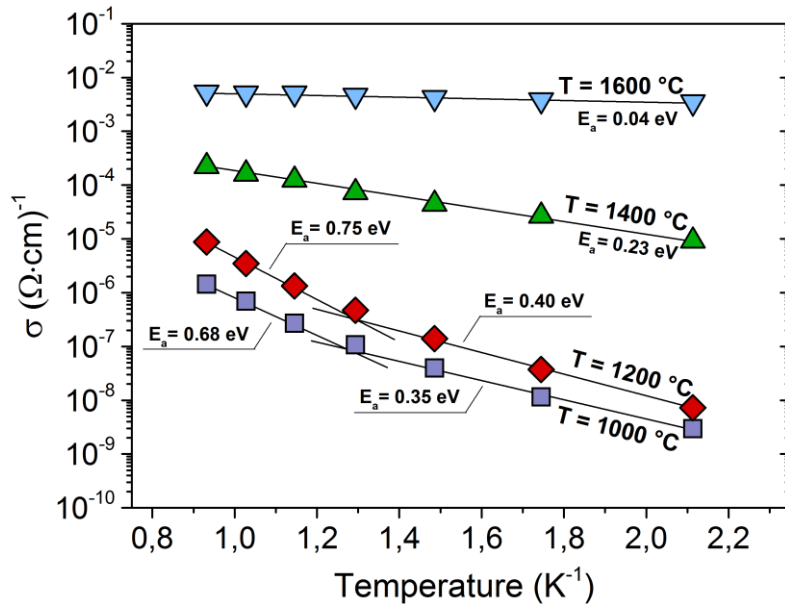


Figure 4.30: Electrical conductivity of C-11 as a function of temperature.

It appears that the conduction in carbon-rich SiOC/C changes with synthesis temperature from VRH (or BTH) to activated Arrhenius-type transport and semimetallic transport in π -conjugated extended states.

Figure 4.31 plots the activation energy E_a as a function of the segregated carbon for samples prepared at $T = 1600\text{ }^\circ\text{C}$. The activation energies were derived from the dc conductivity ($\sigma_{0.01\text{Hz}}$) in the temperature range of $200 \leq T \leq 800\text{ }^\circ\text{C}$. Three different electrical transport regimes can be distinguished as the activation energy decreases from $E_a = 1$ to 0.3 eV and finally to 0.028 eV .

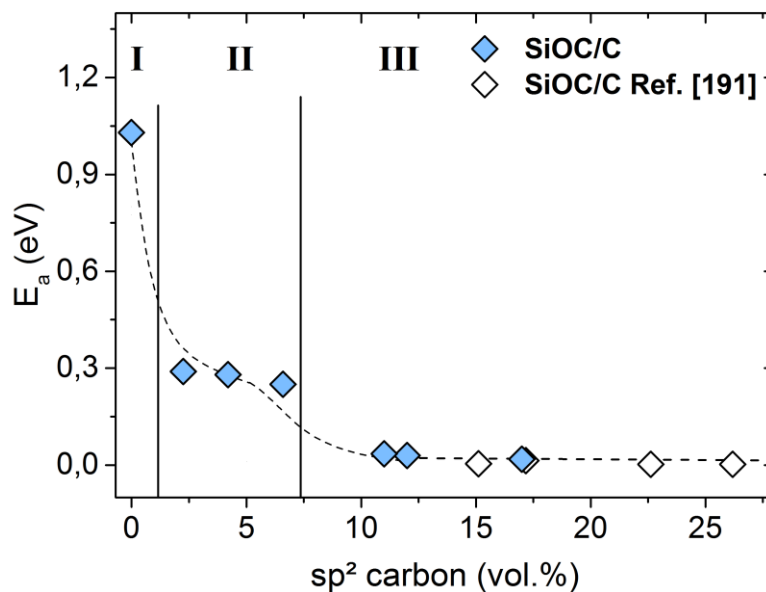


Figure 4.31: E_a of the different conduction mechanism in SiOC/C derived from dc conductivity in the temperature regime of $200 \leq T \leq 800\text{ }^\circ\text{C}$ as a function of the sp^2 carbon.

In the first regime I, conduction occurs within the amorphous silica network as the amount of sp^2 carbon is very low ($\phi_c < 1$ vol.%) and sparsely separated. According to Hapert a high concentration of silicon dangling bonds are present within $a\text{-SiO}_x$, showing a VRH transport within localized states [229]. A VRH conduction mechanism is also likely for carbon-depleted SiOC, due to the defective microstructure of the SiOC matrix.

In the second (semiconducting) regime II ($\phi_c = 2 - 6$ vol.%) the graphitic precipitations are still separated by the SiOC matrix but the resulting potential barrier for the transport is lowered ($E_a \approx 0.3$ eV). The low activation energy arises from additional carbon defects states within the band gap presumably overlapping with the silicon dangling bonds states. A very similar activation energy ($E_a = 0.3$ eV) has been found by Dasgupta *et al.* who investigated hopping between graphitic islands separated by a lower conducting sp^3 layer [81].

In the last regime III, the carbon concentration is above the percolation threshold for samples prepared at $T = 1600$ °C. Thus, the electrical transport is dominated by the continuous, three dimensional carbon sp^2 network yielding activation energies in the range of $E_a = 0.035 - 0.02$ eV, which perfectly resemble the conduction energies found in glassy carbon [55]. The transition from semiconducting to semimetallic conduction is accompanied by the reduction of the gap between carbon π and π^* band states. Carbon essentially controls the density of states, whereas the SiOC states are of minor importance within the third regime. Hence, the same transport mechanism prevails for all samples above the percolation threshold and can be illustrated by the following scheme (Figure 4.32).

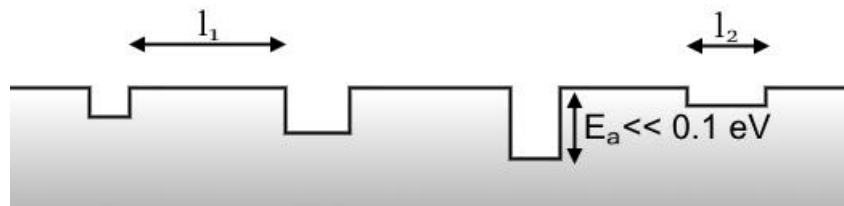


Figure 4.32: Schematically depiction of the shallow traps within the conjugated π -system.

Herein l_1 corresponds to transport in conjugated π -bonds within the carbon network, l_2 represents a shallow carbon defect. This (simplified) model description is supported by the observed constant carrier mobilities from the Hall measurements (Figure 4.33) and the activation energies of $E_a \ll 0.1$ eV from the conductivity studies within $8 < \phi_c < 46$ vol.%.

The electrical behavior of SiOC/C can be correlated with the Raman data obtained in chapter 4.2.2. The activation energy E_a changes inversely with the lateral crystal size L_a assuming that the width of the band gap depends on the concentration of carbon precipitations (Equation 4.12 and Equation 4.13):

$$E_a = \frac{2.1}{L_a} \text{ for carbon based semiconductors [89] and} \quad (4.12)$$

$$E_a = \frac{7.7}{L_a} \text{ for graphitic-like materials [236].} \quad (4.13)$$

An activation energy of $E_a = 0.28$ eV is calculated from Equation 4.12 for the semiconducting samples with an average lateral crystal size of $L_a = 7.5$ nm, which is in excellent agreement with the E_a values from conductivity (Figure 4.31). For graphitic-like materials with $L_a = 9$ nm an activation energy of $E_a = 0.085$ eV is obtained from Equation 4.13 which is of the same order as E_a determined by the conductivity ($E_a = 0.035 - 0.02$ eV).

4.3.4 Hall measurements of SiOC/C

Information about the density and mobility of the dominant carrier type is generally provided by measurements of the Hall Effect. Figure 4.33 plots the carrier density (N) and mobility (μ) as a function of the carbon content for SiOC/C samples prepared at $T = 1600$ °C. Literature values of an SiOC/C synthesized at $T = 1550$ °C are displayed for comparison [237]. Data for the density or mobility can be also obtained from conductivity measurements if the electrical transport solely depends on one charge carrier type (electrons or holes):

$$\sigma = e \cdot N \cdot \mu \quad (4.14)$$

The carrier densities derived from dc measurements (Figure 4.27) are shown in Figure 4.33 (green circles) as a function of the carbon concentration using the experimentally determined mobility of $\mu = 3$ cm²/Vs which is similar to that of turbostratic carbon ($\mu = 3.1 - 6.3$ cm²/Vs [54, 88]). The dc- and Hall-densities perfectly agree above a carbon concentration of ≈ 8 vol.% and are in accordance with values found in glassy carbon [76, 238]. Below this concentration the carrier densities from dc- and Hall-conductivity measurements differ substantially and agreement can only be obtained if a mobility of localized carriers, typically $\mu = 10^{-4}$ cm²/Vs [234], is assumed. Unfortunately, Hall measurements for samples with rather low conductivity or electrical non-uniformity are experimentally challenging and the few data obtained for $\phi_c < 8$ vol.% allow no clear decision.

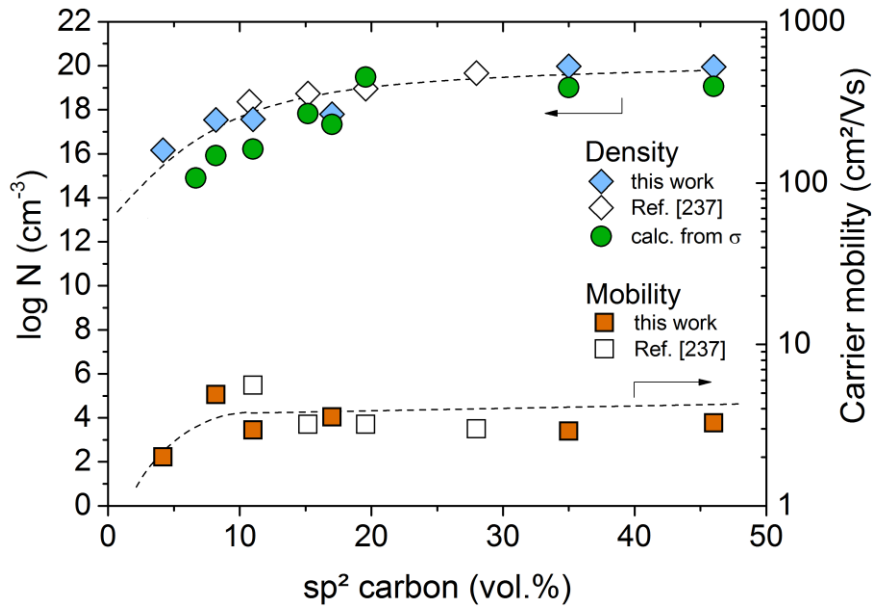


Figure 4.33: Hall density and mobility of SiOC/C prepared at $T = 1600\text{ }^{\circ}\text{C}$. SiOC/C literature values and calculated densities are shown for comparison.

The positive sign of the Hall coefficient indicates p-type carriers which may be due to vacancies (missing carbon atoms within the graphitic lattice) or the removal of dangling bonds creating a hole in the filled π -valence band [239].

Figure 4.34 presents the concentration dependence of the Hall coefficient ($R_H = 1/Ne = \mu/\sigma$). Within the range of $\phi_c = 8 - 43\text{ vol.}\%$ the Hall coefficient remains constant with a typical value of $R_H = 5 \cdot 10^{-2}\text{ cm}^3/\text{C}$ similar to that of glassy carbon ($2.8 \cdot 10^{-2}\text{ cm}^3/\text{C}$) [238].

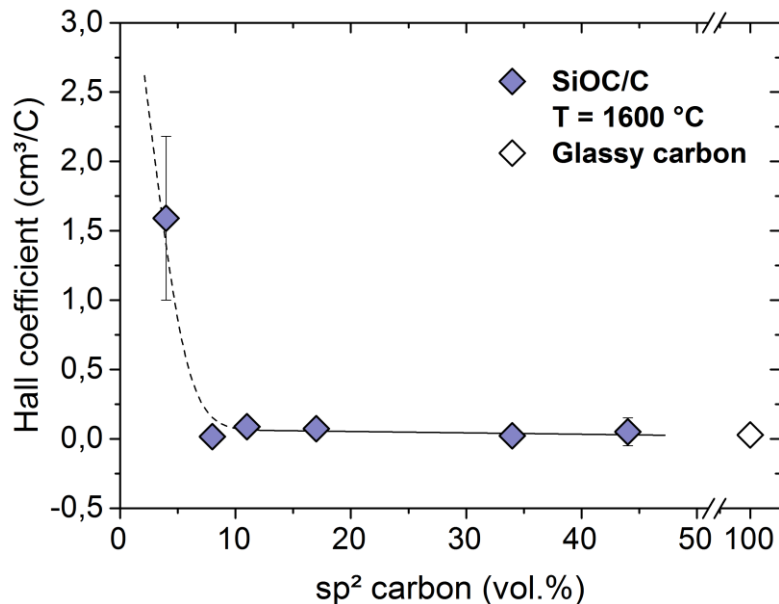


Figure 4.34: Variation of the Hall coefficient with carbon concentration for SiOC/C samples synthesized at $T = 1600\text{ }^{\circ}\text{C}$. Glassy carbon is depicted as reference [238].

Positive Hall coefficients of the same order have been also reported for nano-crystalline graphite ($L_a < 30$ nm [240, 241]). According to Ref. [242] the Hall coefficient increases with increasing disorder and only turns negative in better crystallized graphite ($L_a \gg 100$ nm).

At lower carbon concentrations ($\phi_c < 8$ vol.%) the Hall coefficient increases by two orders of magnitude indicating less ordered crystalline carbon in SiOC/C. This result is supported by the Raman data showing a change of the lateral crystal size L_a and average defect distance L_D in the same concentration region (Figure 4.21 + Figure 4.22). Furthermore, the activation energy for the conductivity (Figure 4.31) increases to ≈ 0.3 eV for $\phi_c < 8$ vol.%.

In summary, the results obtained from the different experiments suggest a change from band-like transport to conduction in localized states which very likely arise from electron/hole confinement when the localization length approaches a lateral crystal size of about $L_a = 10$ nm.

4.3.5 Summary

The electrical properties of SiOC/C vary strongly with the morphology of carbon and the SiOC matrix and indicate a change from conduction in localized states to band-like transport with increasing carbon content. Insulating ($\sigma < 10^{-10}$ ($\Omega \cdot \text{cm}$)⁻¹), semiconducting ($\sigma < 10^{-4}$ ($\Omega \cdot \text{cm}$)⁻¹) or semimetallic ($\sigma < 10^2$ ($\Omega \cdot \text{cm}$)⁻¹) transport can be distinguished depending on the concentration and the degree of order within segregated carbon. The transition to highly conducting SiOC/C - *at the percolation threshold* - depends on the volume concentration of carbon and the synthesis temperature which defines the stage of graphitization or degree of ordering. In case of samples synthesized at $T = 1600$ °C the continuous nano-crystalline graphitic network is formed at $\phi_{\text{cri.}} = 6$ vol.% carbon. The percolation threshold shifts to about 20 vol.% for less ordered samples synthesized at 1100 °C. The conductivity shows a power-law dependence with a critical exponent of about 4 which differs markedly from the (solely geometric defined) universal value $t = 2$ for 3D systems indicating that chemical or physical effects dominate when carbon remains dispersed in the glassy matrix.

Concerning the charge transport mechanism in SiOC/C different conduction regimes can be distinguished for samples prepared at $T = 1600$ °C. Above the percolation threshold σ is very weakly activated ($E_a < 0.03$ eV) and the transport is realized within conjugated π -bonds. Tunneling or hopping of charge carriers between spatially separated graphitic islands appears to be responsible for the electrical conductivity near the percolation threshold. At very low carbon concentrations ($\phi_c < 1$ vol.%), the glassy matrix defines the electrical transport: the activation energy of ≈ 1 eV indicates transport within localized states, presumably silicon dangling bonds.

The charge carrier density of SiOC/C ($T = 1600\text{ °C}$) determined by Hall measurements varies with the carbon content from about 10^{14} to 10^{19} cm^{-3} within $4 < \phi_C < 46\text{ vol.}\%$ carbon. The Hall mobility stays constant above the percolation threshold ($\phi_C \approx 6\text{ vol.}\%$) and has a value of about $3\text{ cm}^2/\text{Vs}$, very similar to that of turbostratic carbon. Below ϕ_{cri} the mobility starts to decrease indicating charge carrier localization. The charge carrier densities obtained from the Hall effect (N_{H}) and the calculated values from the dc conductivity (N_{dc}) agree within the experimental error providing evidence that one type of carrier dominates. The positive sign of the Hall coefficient suggests p-type carriers.

4.4 The piezoresistive effect in SiOC/C

Very little is known about the piezoresistive effect in amorphous semiconductors, due to their highly distorted structure and their complex conduction mechanisms. Even in crystalline semiconductors the piezoresistivity of n-type semiconductors, such as Si, Ge, has not been successfully described until the year 1954, while the effect of their p-type analogues still remains unsolved due to the complexity of the valence band structure [243, 244]. It would be presumptuous to claim that this chapter is able to clarify the origin of the piezoresistive behavior of nano-heterogeneous SiOC/C. Instead, it rather tries to convey a phenomenological description by investigating its dependency on carbon concentration and temperature.

A short overview of the experimental setup and the determination of the gauge factor (GF) by two different methods is provided in the following.

Two experimental setups, schematically depicted in Figure 4.35, have been developed in cooperation with the Electromechanical Department (EMK) at the TU Darmstadt in order to assess the piezoresistive behavior of SiOC/C. In the first setup, depicted in Figure 4.35a), the sample is clamped into the beam and strain is applied by a weight. FEM simulations, performed at the Institut of Electromechanical Department in the working group of Prof. Roland Werthschützky, show the distribution of the tensile (red) and compression forces (blue) and reveals that only compressive stress has to be considered in the sample region, see Figure 4.36.

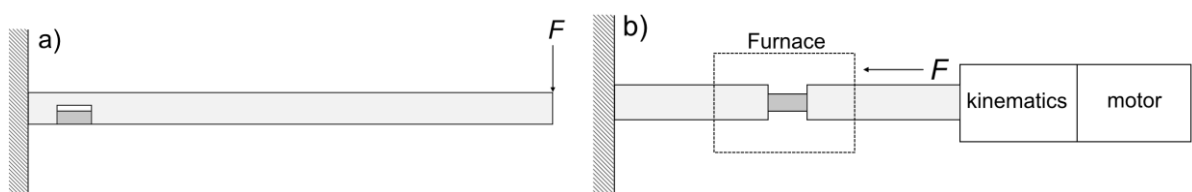


Figure 4.35: Schematic depiction of the developed setups, a) bending beam and b) measurement chamber.

In the second setup, shown in Figure 4.35b), the sample is fixed between two corundum rods within a furnace. The force is applied by a stepper motor. The setup can be operated up to temperatures of $T = 1000\text{ }^{\circ}\text{C}$. A detailed described of the setup is given in chapter 3.3.3.

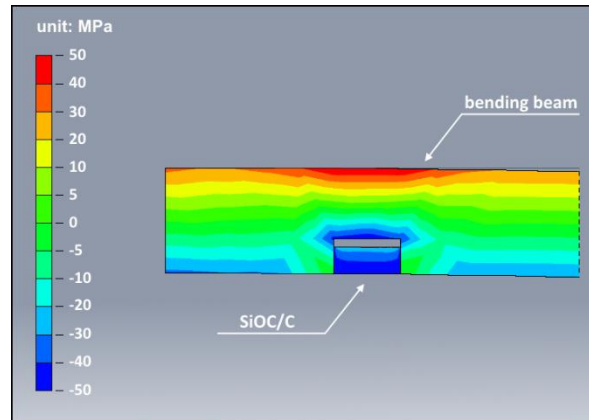


Figure 4.36: FEM simulation of the present stresses within the bending beam and the SiOC/C sample.

A major task of the work was to develop a standard procedure to guarantee precise and reproducible measurements. Therefore, the following steps were taken into account: (i) the samples were grounded and polished to achieve plane front surfaces, (ii) a 70 nm thick electrode (Au, Pt) was sputtered on to the surfaces to ensure a low contact resistance, (iii) the electrical contacts were oriented perpendicular to the strain direction to avoid influence of the strain on the electrical contact, (iv) the samples were preconditioned with $P = 10\text{ MPa}$ for 30 min followed by three abrupt loadings ($P = 30\text{ MPa}$) to provide common starting points. Figure 4.37 depicts the electrical response of the SiOC/C ceramic to the applied strain. Each step of the gradually loading and unloading cycle differ by $P = 50\text{ N}$ with a holding time of 5 min.

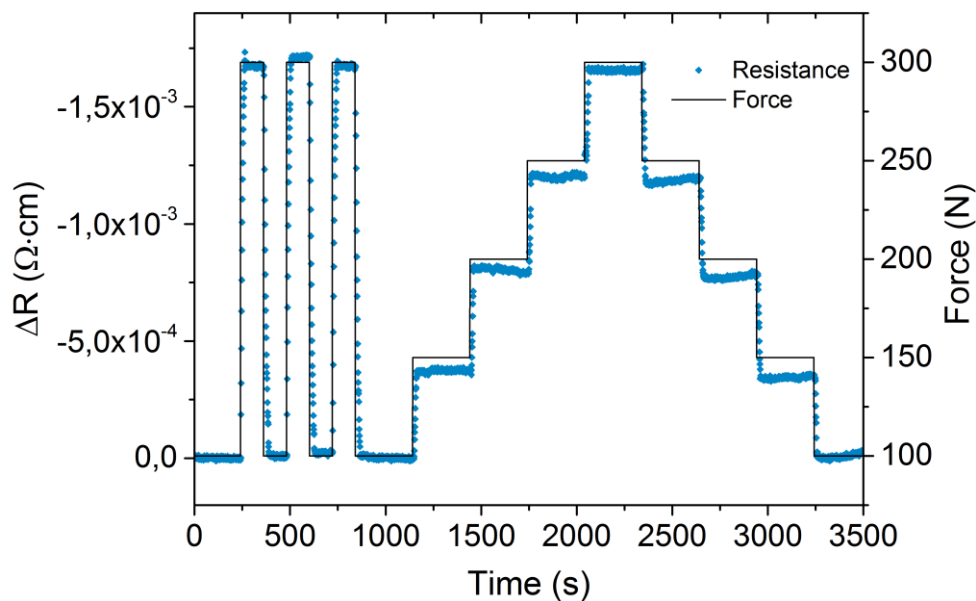


Figure 4.37: Piezoresistive measurement of a SiOC/C sample using the developed stress pattern.

The main parameter for strain sensing is expressed by the gauge factor (GF). In order to determine GF , the strain ε has to be calculated first:

$$\varepsilon = \frac{F}{E \cdot A} \quad (4.15)$$

with F being the applied force, E the Young's modulus of the material ($E_{\text{SiOC/C}} = 100 \text{ MPa}$) and A the contact area of the sample. GF is then defined as the ratio of the fractional change of the electrical resistance to the applied strain,

$$GF = \frac{\Delta R}{R_0} \cdot \frac{1}{\varepsilon} \quad (2.12)$$

with R_0 the electrical resistance at steady-state and ΔR the resistance change caused by the strain. Figure 4.38 presents a typical piezoresistive measurement at RT on a C-17 sample synthesized by $T = 1600 \text{ }^\circ\text{C}$.

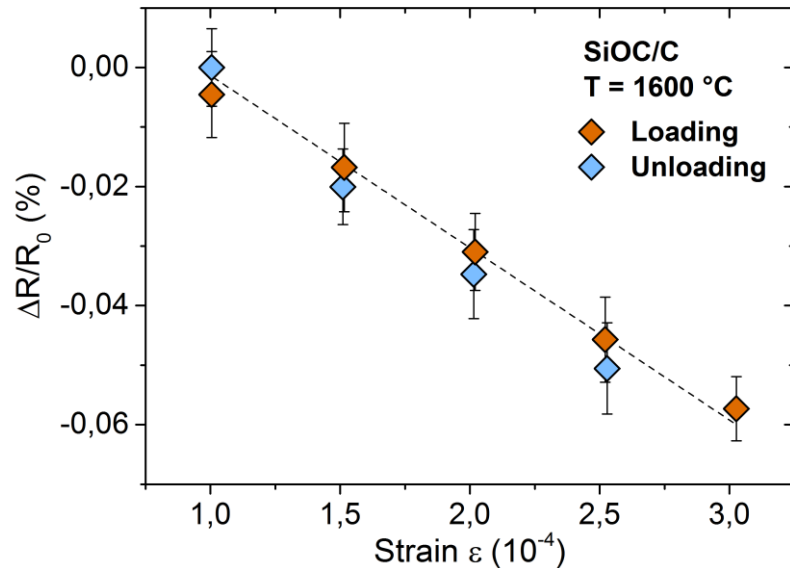


Figure 4.38: Determination of the GF value by plotting the relative resistance change against the strain.

The slope of the $\Delta R/R$ vs. strain plot represents the GF value ($GF = 43$). Precise and reproducible values for GF have been obtained for all samples contacted perpendicular to the strain direction and pre-treated as described above. Without the pre-treatment, the ground resistance shifts markedly causing $\Delta R/R$ values with non-satisfying reproducibility.

4.4.1 Effect of carbon concentration on the piezoresistive behavior

The following chapter deals with the piezoresistive effect of SiOC/C with carbon concentration of $1 < \phi_c < 34 \text{ vol.}\%$ at room temperature and elevated temperatures. All the samples have been synthesized at $T = 1600 \text{ }^\circ\text{C}$ yielding composites with a well-defined carbon phase (nanocrystalline graphite according to Raman) embedded within a glassy matrix. Accordingly, the

focus of the work is set on samples with a continuous carbon network at/above the percolation threshold (Figure 4.27). The main advantage of focusing on 1600 °C samples is that no other types of carbon with very different properties, e.g., amorphous carbon present in SiOC/C synthesized at $T < 1400$ °C, have to be considered.

Figure 4.39 presents the (qualitative) correlation between the Raman and the piezoresistivity data of C-11 clearly indicating that both quantities depend on the degree of disorder in carbon expressed by the intensity ratio I_D/I_G of the Raman D- and G-band (the higher I_D/I_G the higher the disorder).

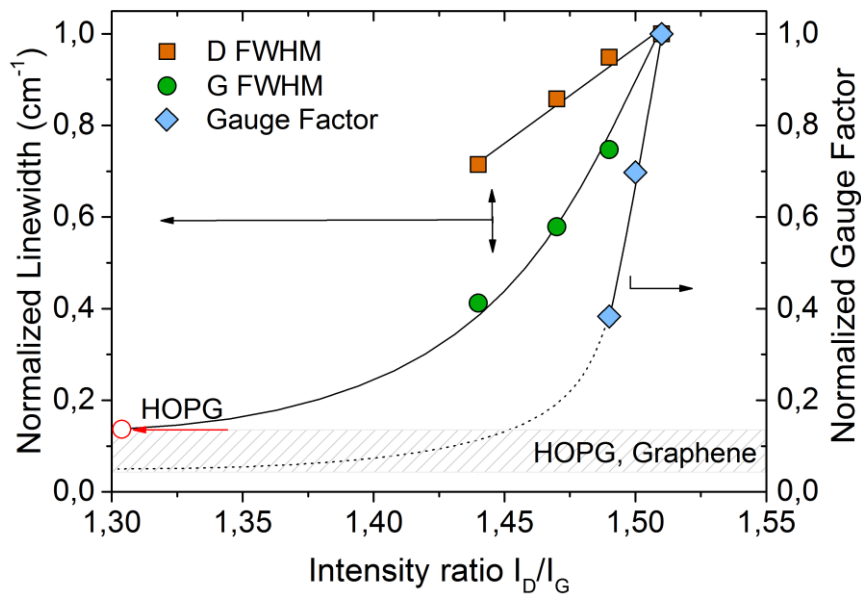


Figure 4.39: Correlation of Raman and piezoresistivity data for SiOC/C. The dashed area represents literature values for GF and Raman linewidth of highly ordered carbon (HOPG, graphene).

For highly ordered carbon (HOPG, graphene) GF decreases to values typical for the geometric contribution to the piezoresistivity (chapter 2.3). The increase of GF is therefore material specific and caused by the disturbance of the graphitic lattice by defects (point, or extended defects, notably dislocations). As shown in Figure 4.40 the GF of diamond-like carbon (DLC) [108, 109] increases with the sp^3 defect concentration by factor of about 3 and reaches a value of about 60 close to the percolation threshold (≈ 30 vol.% sp^3).

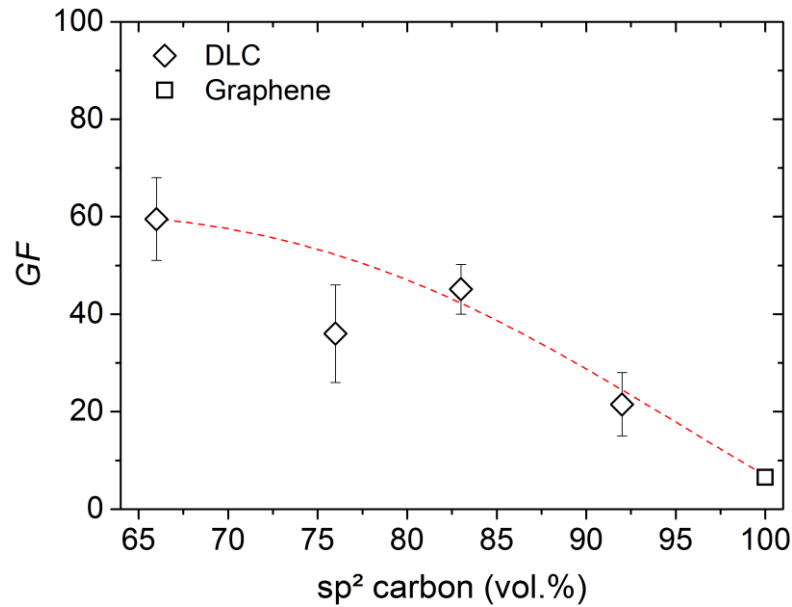


Figure 4.40: Gauge factor as a function of the sp^2 content in carbon allotropes [107, 108, 112].

A very similar behavior can be expected for carbon in SiOC/C. Figure 4.41 depicts the sp^2 carbon concentration dependence of GF in SiOC/C synthesised at $T = 1600\text{ }^\circ\text{C}$. Within between 17 and 35 vol.% carbon the GF rises up to a value of about 43. The GF values for the C-17 and C-11 samples have been determined by the two different measurement techniques described in chapter 4.4 strengthening the reliability of this data. It appears that GF increases with the defect density.

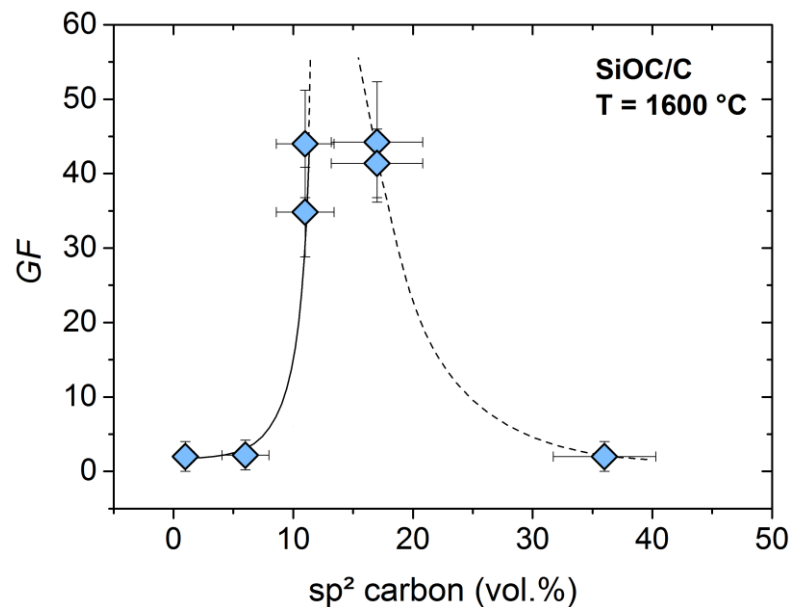


Figure 4.41: Course of the piezoresistive behavior of SiOC/C as a function of the carbon content.

The Raman data supports this correlation. According to Figure 4.42 the average defect distance calculated by Equation 4.10 increases from 7 to 8.5 nm between 6 and 46 vol.% carbon. Hence, the defect density increases with decreasing amount of carbon.

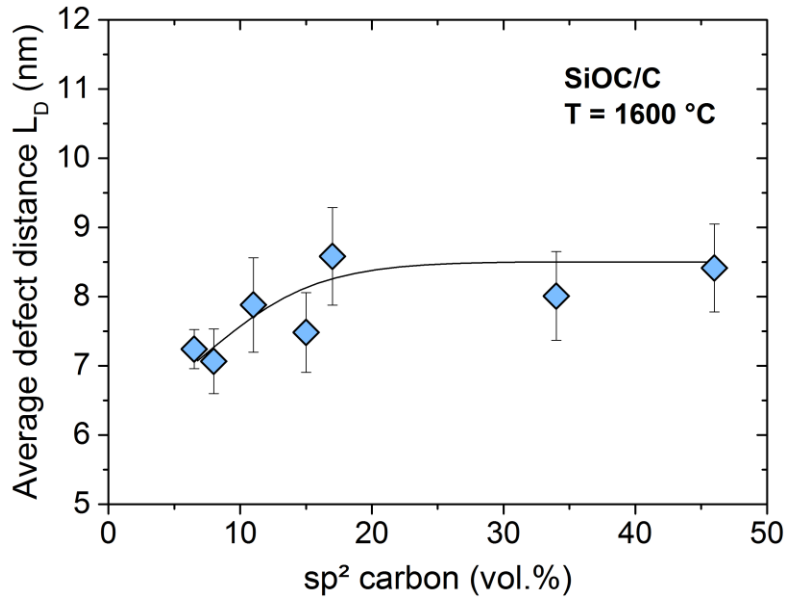


Figure 4.42: The average defect distance L_D plotted against the carbon concentration.

Since the defects are randomly distributed their average distance should vary with the carbon volume as $V^{-1/3}$. Thus, a linear dependency between the logarithmic conductivity and $V^{-1/3}$ should be observed indicating tunneling or hopping transport within the carbon network [245]. Figure 4.43 presents the $\ln \sigma$ versus $V^{-1/3}$ plot for SiOC/C samples with about 4 to 36 vol.% carbon prepared at $T = 1600$ °C.

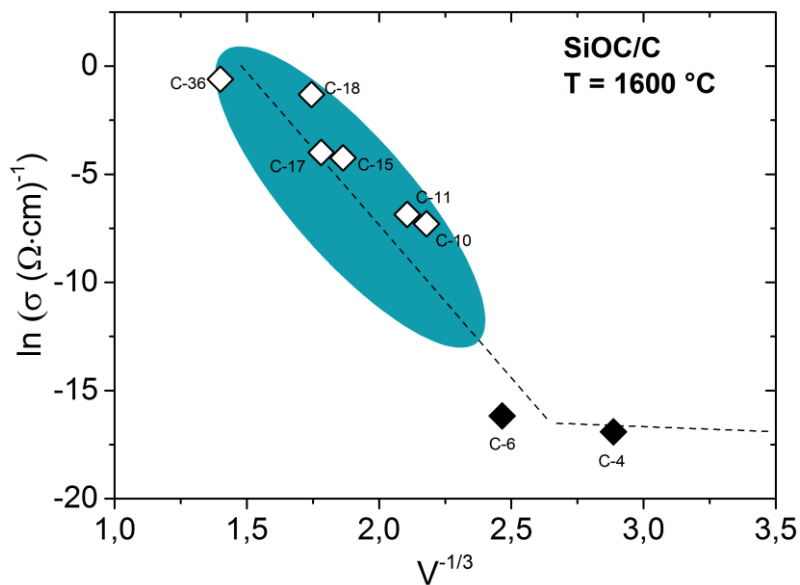


Figure 4.43: Natural logarithm of the conductivity as a function of $V^{-1/3}$.

According to Figure 4.41 GF changes abruptly (from about 40 to 3) close to the percolation threshold (C-11) indicating that defects in carbon are now of minor importance and that the piezoresistive response mainly depends on the geometric contribution of the glassy matrix. This is in accordance with the behavior in other composites ($\text{RuO}_2/\text{Glass}$, carbon/polymer, etc...) when reaching the percolation threshold [46, 149, 246, 247].

The conductivity and piezoresistivity of composite materials such as PDCs, RuO₂/Glass and carbon polymer is frequently described by the tunneling-percolation theory with its main parameters, the tunnel distance and the potential barrier height [46, 248, 249]. A generalized formula for the electric tunnel effect between similar electrodes separated by a thin insulating film has been given by Simmons [250]. The tunneling current density (J) can be described by the following Equation 4.16:

$$J = \left[\frac{3(2m\varphi)^{-\frac{1}{2}}}{2s} \right] \cdot \left(\frac{e}{h} \right)^2 V \cdot \exp \left[- \left(\frac{4\pi s}{h} \right) \cdot (2m\varphi)^{\frac{1}{2}} \right] \quad (4.16)$$

with m, e and h being the electron mass, charge of an electron and Planck's constant, respectively. φ , s and V are the height of tunnel potential barrier, potential barrier width and voltage applied across the barrier, respectively [250]. According to Equation 4.16, the tunnelling current is an exponential function of the barrier width, implying a strong dependence of the resistivity on the particle distance. As a consequence, the resistivity of a composites may decrease with increasing the compressive strain, as the distance between two adjacent particles is narrowed. Following Simmons a substantial change in the current density or resistivity will occur only for carbon particles separated by $\lesssim 1$ nm. Accordingly, the tunneling-percolation model can be used to describe the piezoresistive behavior in the very narrow carbon concentration range of the percolation threshold. At concentrations $\ll \phi_{\text{cri}}$ the compressive strain will not be able to induce a marked piezoresistive response because of the much larger separation of the carbon particles or increased tunnel distances $\gg 1$ nm.

The generalized tunneling model of Simmons suggests that the value of *GF* will be of the same order for the various composite materials mentioned above, since the barrier height φ (defined by carbon), the tunnel distance s (≈ 1 nm at ϕ_{cri}) and the dielectric constant ϵ_r of the insulating phase (MgO, Al₂O₃, cement, glass) are comparable ($4 < \epsilon_r < 5$, [251-253]). Figure 4.44 presents the *GF* values of several mainly carbon containing composites determined at their respective percolation threshold ϕ_{cri} . Very similar *GF* values no larger than 100 are observed. *GF* values in the range of 38 – 55 and 48 have been reported for carbon black (CB) and carbon nanofibers (CNF) containing cement composites [140, 149, 151]. In both cases, a dispersant agent was used to account for a homogenous dispersion of the carbon fillers. Magnesia and alumina composites functionalized with graphite (Gr.) yielded *GF* values in a range of 42 – 45 [120, 121, 123]. Tibrewala *et al.* investigated the piezoresistive responds of diamond-like carbon (DLC) and reported on *GF* values in the range of *GF* = 51 – 68 [108].

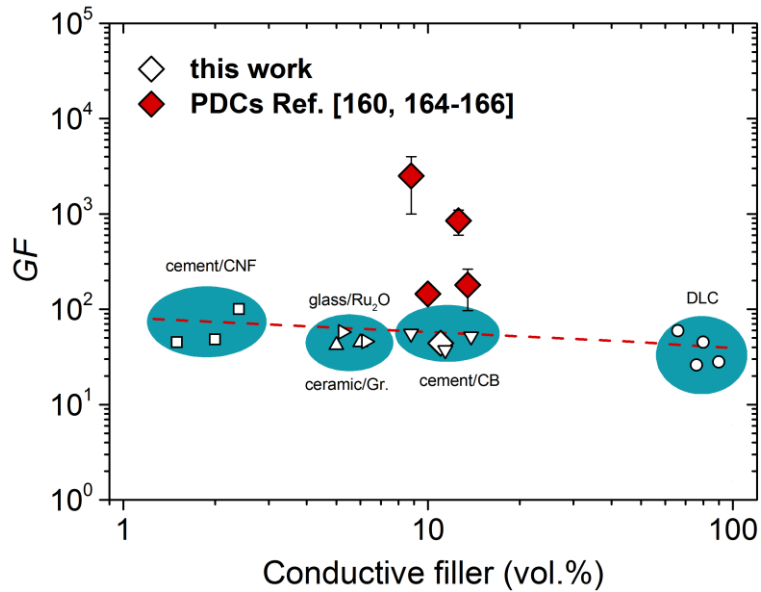


Figure 4.44: GF (at the respective $\phi_{\text{cri.}}$) of inorganic nano-composites, with $\square = [140]$, $\triangle = [120, 121]$, $\triangleright = [46]$, $\nabla = [149, 151]$ and $\circ = [108, 109]$.

For the sake of comparison the GF values of PDC materials from the literature (diamond symbols) and the GF value for C-11 (our value closest to ϕ_c) are included in Figure 4.44. Evidently, these GF values reported on PDCs do not fit into this classification and will be discussed in chapter 4.4.4.

4.4.2 Effect of temperature on the piezoresistive behavior

In the following, the temperature dependency of the GF value of C-11 prepared at $T = 1600\text{ }^\circ\text{C}$ is presented and compared to literature [166]. Two different measurement setups have been used for the thermal investigations. In the low-temperature region ($T < 400\text{ }^\circ\text{C}$) the electrical contacts are oriented perpendicular to the strain direction whereas in the high-temperature region ($T > 1000\text{ }^\circ\text{C}$) the compressive strain was applied directly onto the contacted front surface (Figure 3.2).

Within the temperature range $RT < T < 400\text{ }^\circ\text{C}$ the GF is almost constant. The Arrhenius plot yields an activation energy of about $0.01 \pm 5 \cdot 10^{-3}\text{ eV}$, as depicted in Figure 4.45. The very low activation energy suggests that GF is either correlated with a weakly temperature dependent carrier mobility or a weak change of the carrier density. According to the Hall measurements of C-11 both quantities change very slightly within the temperature range given above (2.6 to $1.4\text{ cm}^2/\text{Vs}$ and $7 \cdot 10^{-17}$ to $1 \cdot 10^{-18}\text{ cm}^{-3}$) allowing no unambiguous decision which quantity determines the temperature dependence of GF .

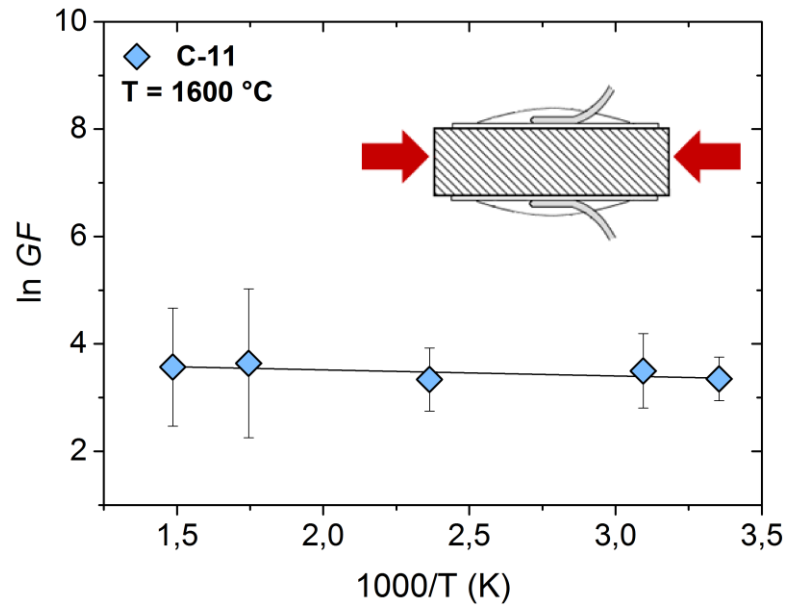


Figure 4.45: Arrhenius plot of GF for a C-11 sample within the range of $25 < T < 400$ °C.

Figure 4.46 depicts the Arrhenius plot of GF in the high-temperature range $1000 < T < 1200$ °C for the C-11 sample together with the literature values from Ref. [166] (open circles, filled circles: extrapolated values). The activation energy derived from the plot is 0.1 ± 0.05 eV.

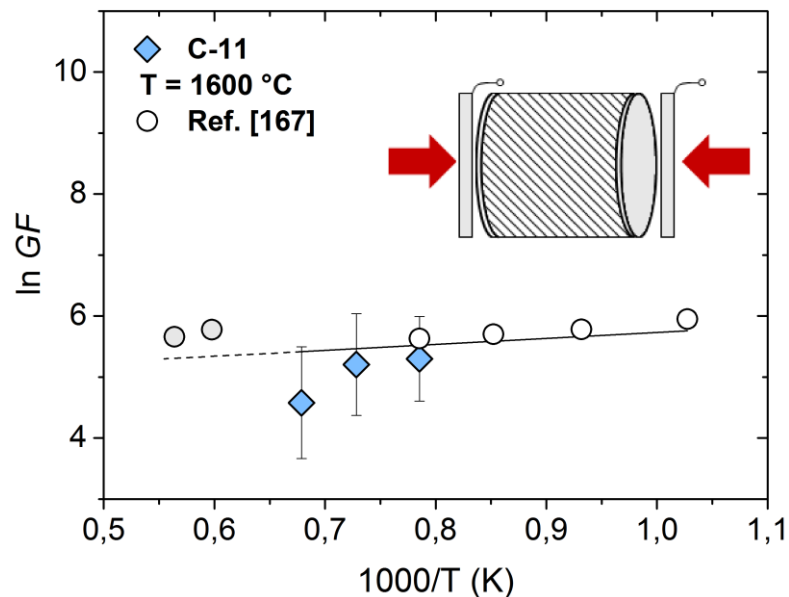


Figure 4.46: Arrhenius plot of GF of a C-11 sample in the range of $1000 < T < 1200$ °C. Literature values (empty and filled circles) of SiOCN/C ($\phi_c = 8.8$ vol.%) are presented for comparison [166].

In view of the large error in E_a it is difficult to decide whether one observes the same activation energy in the high- and low-temperature range or not. Even if we assume that GF is determined by the same transport properties it has to be explained why the absolute GF values differ markedly in both regions, see Figure 4.47.

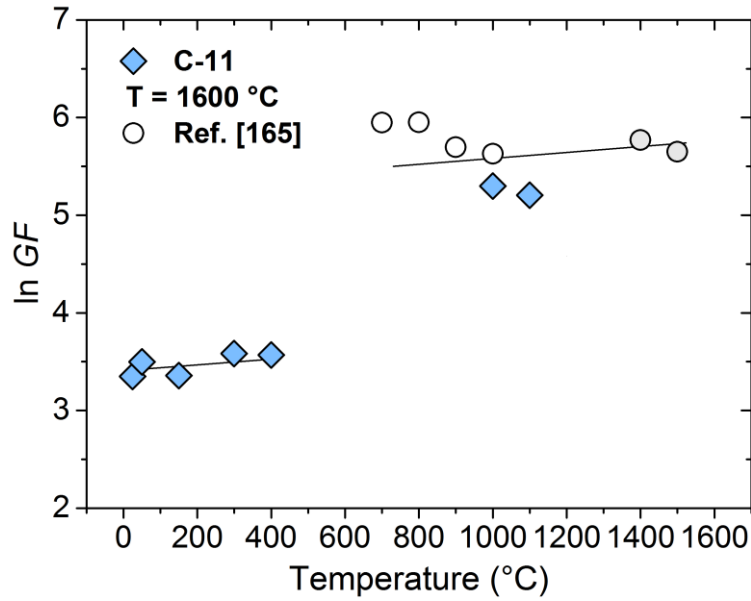


Figure 4.47: GF values of the two temperature regimes. Literature values (empty and filled circles) of SiOCN/C ($\phi_c = 8.8$ vol.%) are presented for comparison [165].

A possible explanation is the following. As described above two different measurement techniques have been applied: in the high-temperature experiment compressive strain is applied to the contacts at the front surfaces whereas at low temperature only the strain in the bulk (ϵ_{bulk}) determines the piezoresistive effect. The observed discontinuous change in GF may therefore arise from the different local strain distributions at the sample/electrode interfaces.

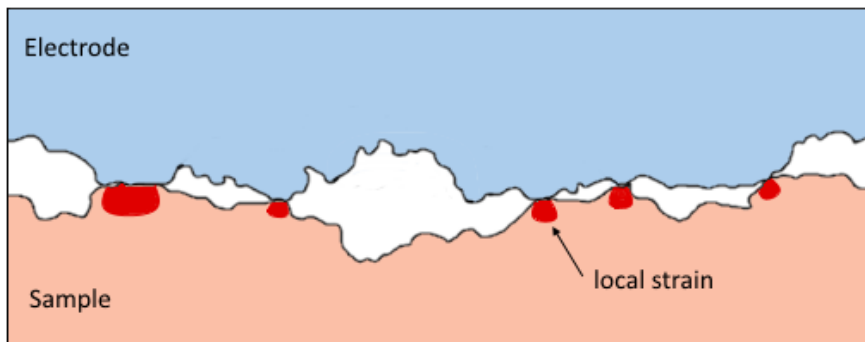


Figure 4.48: Schematic depiction of the local strain at the sample/electrode interface during loading.

Agreement between the two measurements can then be obtained if the (local) strain in the electrode region of the high-temperature setup is approximately one magnitude higher than the apparent strain applied. Hence, the local strain will be given by:

$$\epsilon_{local} = \chi \cdot \epsilon_{bulk} \quad (4.17)$$

with χ the enhancement factor. The enhancement factor will depend on the surface roughness in the sample/electrode interface. The rougher the surface the more contact points will be present raising the strain in the interface.

4.4.3 Origin of the piezoresistive effect in SiOC/C

The change of the resistance with strain in SiOC/C composites will depend on three factors: the charge carrier mobility μ and density N and the geometrical change. The latter can be neglected due to the high stiffness of the material ($E \approx 100$ GPa, [254]). The resistance generally scales with $1/\mu$ and $1/N$. Experimentally, one observes that the resistance decreases with strain (and temperature). Hence, the origin of the piezoresistive effect will be either an increase in μ or N . For (isotropic) condensed matter the dispersion relation $E(k)$ remains linear in the presence of strain.

$$E(k) = h v_F(\epsilon) \cdot k \quad (4.18)$$

Where h is the Planck constant, k the wave factor and v_F the Fermi velocity that depends on the strain ϵ . At a given energy $E(k)$ the magnitude of k is larger for strained materials than in relaxed materials. Accordingly, the density of states has to increase with strain because it is approximately proportional to the inverse of the squared fermi velocity:

$$N(\epsilon) \sim \frac{1}{v_F(\epsilon)^2} \quad (4.19)$$

An increase of the carrier density leads to a decrease of the resistance as observed in our piezoresistive measurements: the origin of the piezoresistive effect therefore would be the strain-induced change of the density of states near E_F . A change of the mobility is unable to explain the experimental results. Assuming again that the Fermi velocity decreases with strain and that v_F scales with μ , the mobility will decrease leading to an increase of the resistance with strain which is not observed. However, both quantities may change with strain. In order to be consistent with the experimental results the change in the carrier density has to outweigh the mobility change. Further experimental and theoretical work are needed to give a unique explanation for the piezoresistive effect in SiOC/C.

4.4.4 Comment on giant gauge factors in PDCs reported in literature

As shown in Figure 4.44 GF values of about 200 to 2000 exist for PDCs with typical carbon concentration between 8 to 11 vol.% which differ substantially from the values obtained in this work with the configuration depicted in Figure 3.2a).

Thin film resistors (TFR) and silicon nanowires are the two main systems in which enhanced gauge factors are commonly observed. In both cases stress concentration is held to be responsible for the observed effect i.e., the local strain is enhanced with respect to the averaged macroscopic strain [255, 256]. According to Ref. [255] GF enhancement occurs in

(heterogeneous) thin film resistors when: the conducting phase is stiffer than the glassy one and when the size of the spatially separated conducting particles is much larger than the tunneling distance. Both requirements are fulfilled for polymer-derived materials close to the percolation threshold indicating that the strain distribution in the interface region between the conductive filler(carbon)/glassy matrix determines the GF enhancement. In case of silicon nanowires the GF changes with the chemical treatment of the wires. The enhancement of GF is expressed as:

$$GF_{enhanced} = \chi \cdot GF_{bulk} \quad (4.20)$$

similar in magnitude to the bulk effect and related to geometric (local) stress concentration. In this work mainly SiOC/C samples with carbon concentrations above the percolation threshold have been investigated. In this case, no conducting carbon particles remaining suspended in the matrix have to be considered but a continuous carbon network within a glassy matrix. Hence, the strain distribution within such composites will differ from that of the above mentioned composites close to the percolation threshold. Generally, the local strain within the sample and the local strain within the interface electrode/sample region contribute to the GF enhancement. If the local stress within the sample is small and negligible the stress distribution in the interface dominates changing markedly when compressive stress is applied. As suggested in Figure 4.48 the local stress will decline with declining surface roughness and vanish for plain surfaces. Such a behavior is observed for, e.g., sample C-11 (Figure 4.49) when the sample is contacted according to Figure 3.2b).

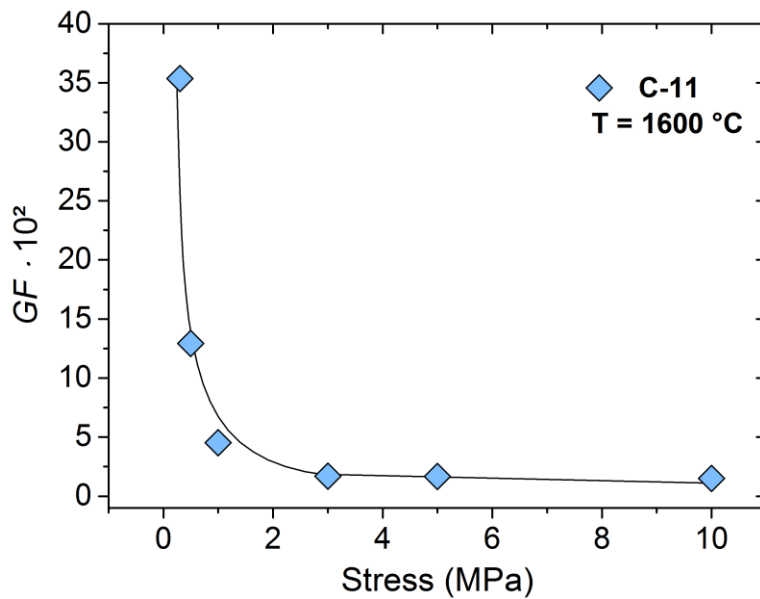


Figure 4.49: Gauge factor as a function of the applied pressure of a C-11 sample.

For low compressive stress (0.5 - 3 MPa) GF corresponds to values around 500 - 3500. When increasing the stress to 5 - 10 MPa GF decreases to about 145 due to the declining of the local strain and approaches the bulk value, $GF_{\text{bulk}} \approx 70$, determined with the contact geometry depicted in Figure 3.2a).

4.4.5 Development and application of a SiOC/C based prototype

The urgent need of the automotive and aircraft industry for sensing over a broader temperature range up to $T = 500\text{ }^{\circ}\text{C}$ have been expressed several times and have led to extensive effort to develop high-temperature sensor materials [257, 258]. Currently, piezoelectric materials are widely used in commercially available sensors which often suffer from the loss of their piezoelectric properties at temperatures above $T > 200 - 300\text{ }^{\circ}\text{C}$ [259]. The increased thermal stability of the SiOC/C ceramic, however, meets the industrial requirements and thus makes it a promising candidate material for future sensing at elevated temperatures ($T > 400\text{ }^{\circ}\text{C}$).

A first sensor prototype based on a C-17 sample was developed in cooperation with the institute of Electromechanical Design at the TU Darmstadt and the department of Energy and Automation technology at the TU Berlin for RT measurements. A schematic depiction of the developed sensor is given in Figure 4.50. The sensor consist of a base plate connected to an initial load element. The piezoresistive SiOC/C is polished in rectangular shape (3x3x10 mm) and clamped between the base and the load element. As the screws are tightened, the load element is pressed against the base applying the required preload of $P = 10\text{ MPa}$. Apart from holding the SiOC/C material in place, the springs also minimize the danger of tilting upon tightening. The electrical contacts are located on the long side of the sample and thus are not affected by the applied preload. To investigate the dynamic piezoresistive behavior a planetary gear was constructed at the TU Berlin given in Figure 4.51.

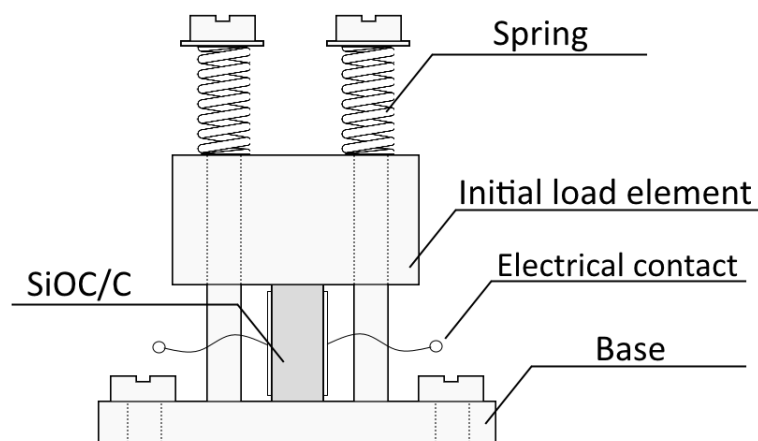


Figure 4.50: Schematic depiction of the piezoresistive SiOC/C sensor prototype for RT measurements.

A commercially available piezoelectric sensor (PIC 255) from the company *PI Ceramics* was used as reference. In order to reduce the damping, a very thin layer of silicon glue was used to attach the PIC 255 onto the plane surface of the ring gear, whereas the base of the SiOC/C prototype is screwed on the outer rim. Both sensors are located across each other to ensure comparable measuring conditions. Goal of the investigation was to measure the surface extension of the ring gear which occurs during the rotation of the three planet gears.

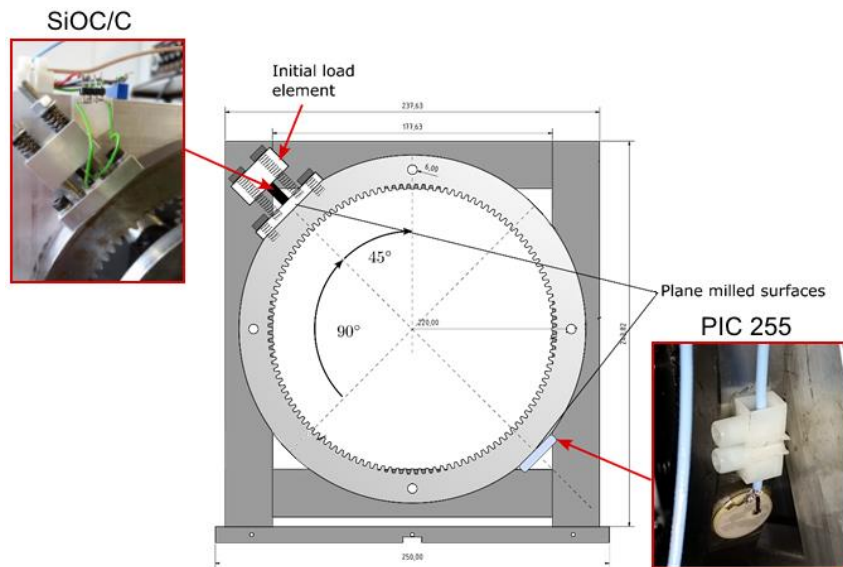


Figure 4.51: Experimental setup of the planetary gear along with the two compared sensors.

The dynamic surface extension induces a radial strain which is detected by the sensors and converted into an electrical signal. In the following, the measured natural frequency of the ring gear is used to compare the two sensors. Therefore, two different rotational speeds are investigated. Figure 4.52 depicts the electrical signal as a function of the frequency determined by the SiOC/C prototype and the PIC 255 at 88 and 120 rpm. At 88 rpm a maximum frequency of $f = 175$ Hz can be detected for both sensors, which represents the natural frequency of the ring gear. In comparison with the PIC 255, the SiOC/C prototype exhibits a significantly higher background noise together with a smaller signal strength. Due to the low signal strength, the utility frequency of the electric power grid is also detected. This frequency operates at $f = 50$ Hz which is why frequencies bearing a multiple of this 50 Hz (100, 150, 200 Hz ...) can be assigned to the electric power grid and not to the vibration frequencies of the ring gear. However, the signal to noise ratio of the SiOC/C prototype is still fair enough to evaluate the data and to detect the main natural frequency at 88 rpm. Increasing the rotational speed up to 120 rpm yielded a nearly Gaussian shaped signal at $f = 243$ Hz for the PIC 255 with a somewhat lower signal strength. The same main frequency is detected by the SiOC/C prototype along with a decent signal to noise ratio.

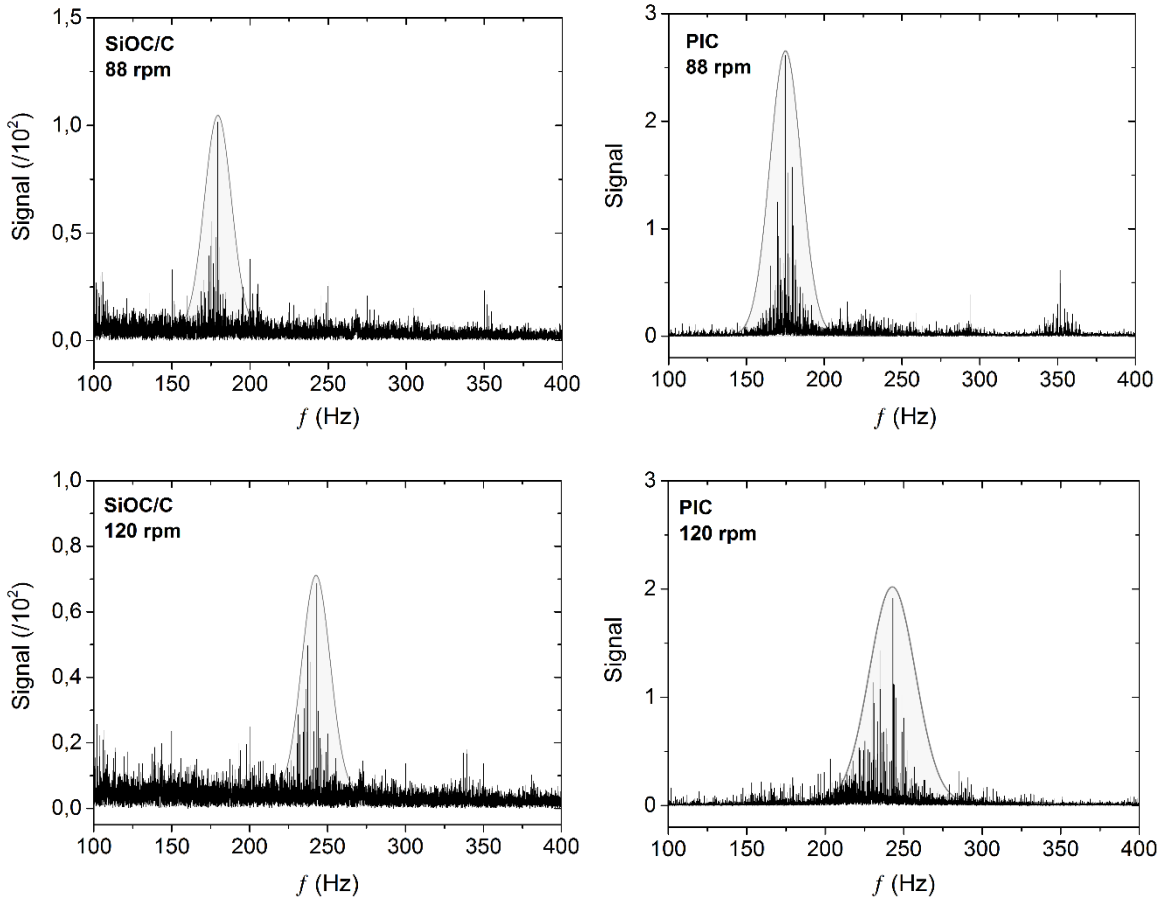


Figure 4.52: Natural frequency of the ring gear measured at 88 and 120 rpm using the SiOC/C prototype and a commercially available PIC 255 sensor.

In general, a low electrical resistivity is desirable in sensing measurements since the low electrical resistivity is helpful for enhancing the signal to noise ratio. However, a low resistivity impairs the piezoresistive behavior of the SiOC/C material. Fortunately, there is a balance between a decent piezoresistive effect and low electrical resistivity near the percolation threshold. Thus, the percolation threshold is an important parameter for designing and further optimizing the sensing property of the SiOC/C material.

In summary it can be stated that, in a first attempt the SiOC/C based prototype has proven its worth in both rotation ranges as a useful sensor to detect the main natural frequency of the ring gear. Together with a suitable downstreamed electronic filter (low-pass and/or band pass filter) and an adjusted composition closer to the percolation threshold, the sensitivity can be further increased and might even be used in future to detect early abrasion or even crack formation of the cogs. Furthermore, does the thermal stability of the material allows for sensing at elevated temperatures in contrast to the commercially available piezoelectric sensor materials. To further improve the sensibility of the sensor the electrical resistance should be assessed using a four-point method instead of a two-point method. This would allow to fully exclude the lead and contact resistance from the measurement as separated electrodes for current and voltage

are used. Hence, the SiOC/C material can be considered a promising future sensor material for sensing at elevated temperatures ($T > 400\text{ }^\circ\text{C}$).

4.4.6 Summary

Two different experimental setups have been developed to determine the gauge factor GF of SiOC/C in compressive mode after preloading. The latter proved to be essential to achieve reliable gauge factors for the bulk material needed for strain sensing applications (for demonstration a radial strain sensor has been developed in this work).

As in other carbon based materials the GF of SiOC/C prepared at $T = 1600\text{ }^\circ\text{C}$ seems to depend on the concentration of point or extended defects. As supported by the Raman data the defect density increases with decreasing amount of carbon and, accordingly, GF increases steadily within the range of 36 to 17 vol.% carbon ($GF_{\text{C-36}} = 3$, $GF_{\text{C-17}} = 45$). Within this concentration range the piezoresistive behavior appears to be related to strain-induced changes of the density of states near E_F . A change in mobility is unable to explain the experimental result.

A very similar increase in GF up to about 50 occurs at low carbon concentration in the range of 6 to 11 vol.% carbon. Whether GF diverges at the percolation threshold ($\phi_{\text{cri.}} \approx 6 \pm 2\text{ vol.}\%$), as expected from percolation-tunneling theory, or reaches a maximum in the range of 11 to 17 vol.% carbon, remains unclear and needs further investigations.

Divergence of GF at the percolation threshold may explain the extremely high GF s, reported in literature for other PDCs. However, giant GF values may also originate from local strain concentration, with $\varepsilon_{\text{local}}$ deviating from $\varepsilon_{\text{bulk}}$ by an enhancement factor χ . In order to explain these literature data χ has to reach values $\gg 10^2$.

5 Conclusion & Outlook

Within the thesis, the state of carbon in SiOC/C and its piezoresistive effect have been investigated. Polymer-derived SiOC/C ceramics with different amount of carbon ($\phi_C = 1 - 46$ vol.%) have been synthesized by pyrolysis of poly-organosiloxane networks and subsequent spark plasma sintering at different temperatures ($1000 < T < 1800$ °C). The morphological and electrical properties of carbon within SiOC/C mainly depend on the actual carbon concentration and the synthesis temperature which determines the stage of graphitization. In case of samples with very low carbon content ($\phi_C \lesssim 1$ vol.%) carbon remains isolated in the glassy matrix and accordingly the electrical transport is limited by localized states in the matrix. With increasing synthesis temperature the structural order within carbon changes from a disordered amorphous to a nano-crystalline state as proven by UV Raman studies. The change/ordering tendency from the amorphous to the crystalline state is reflected by the decrease of the Raman D band and the simultaneous increase of the Raman G band. Their intensity ratio A_D/A_G is generally accepted as a measure of the graphitization progress and allows to assess the lateral crystal size (L_a) and the average defect distance (L_D) in carbon. In SiOC/C L_a stays constant (7.5 nm) up to $T = 1500$ °C and starts to rapidly increase above this temperature indicating expansion of the graphitic layer size or increasing ordering, respectively. The latter is also seen in L_D which increases from about 6 nm ($T = 1000$ °C) to 12.5 nm ($T = 1800$ °C). As $L_D \sim 1/N_{\text{def}}$, the defect density decreases with temperature as expected for ongoing crystallization. Vacancies have been identified as main type of defect in nano-crystalline graphite.

Concerning the electrical and piezoresistive properties of SiOC/C the experimental work has been focused on samples prepared at $T = 1600$ °C. The main advantage of this way of proceeding is that only one well-defined type of carbon (nano-crystalline carbon) has to be considered which forms a continuous three-dimensional graphitic network at a carbon concentration $\gtrsim 6$ vol.%, i.e., at the percolation threshold ϕ_{cri} . Above ϕ_{cri} , electrical transport occurs within conjugated π bonds and is only weakly activated ($E_a < 0.03$ eV) like in glassy carbon. Below ϕ_{cri} , semiconducting behavior is observed for carbon concentration of about 2 to 6 vol.% indicated by an activation energy of $E_a \approx 0.3$ eV and charge carrier densities of $N = 10^{15}$ to 10^{18} cm⁻³. The transport mechanism changes from band-like transport to conduction via localized states which very likely arise from electron/hole confinement when the localization length approaches a lateral crystal size less than 10 nm as derived from Raman measurements. SiOC/C changes its resistivity upon applying a strain and, accordingly, the piezoresistive effect also relies on the carbon concentration and the degree of ordering within carbon. Close to/at

the percolation threshold the gauge factor (GF) can be explained by charge carrier tunnelling. At this concentration rather high GF values are observed which, according to theory, originates from divergence at ϕ_{cri} or local stress concentration. Above ϕ_{cri} GF appears to be related to the density of defects within the carbon network. A change in mobility is unable to explain the experimental results.

Future work should concentrate on the following topics:

- (i) investigation of the piezoresistivity of samples synthesized at 1100 and 1400 °C to complete the results on the 1600 °C samples.
- (ii) 4-point measurements of the resistivity at high-temperatures ($T > 400$ °C) to check/exclude the strain contribution from the interface electrode/sample.
- (iii) modelling of the strain distribution and study of the interface carbon/glassy matrix to determine possible effects on the electrical properties.
- (iv) long-term stability as an essential requirement for sensor development.
- (v) thermally stable packaging of the sensor electronics including reduction of the background noise by a suitable electronic filter.

6 References

1. Fritz G. and Raabe B., *Z. Anorg. Allg. Chem.*, 286(3-4), 149-167, **1956**.
2. Ainger F. W. and Herbert J. M., The preparation of Phosphorus-Nitrogen Compounds as Non-Porous Solids, in *Special Ceramics*, **1960**, Academic Press: New York.
3. Chantrell P. G. and Popper P., Inorganic Polymers for Ceramics, in *Special Ceramics*, **1965**, Academic Press: New York.
4. Verbeek W., Ger. Pat. No. 2218960, **1973**.
5. Verbeek W. and Winter G., Ger. Pat. No. 2236078, **1974**.
6. Winter G., Verbeek W., and Mansmann M., Ger. Pat. No. 2243527, **1974**.
7. Yajima S., Okamura K., Hayashi J., and Omori M., *J. Am. Ceram. Soc.*, 59(7-8), 324-327, **1976**.
8. Yajima S., Hayashi J., Omori M., and Okamura K., *Nature*, 261(5562), 683-685, **1976**.
9. Yajima S., Hasegawa Y., Hayashi J., and Iimura M., *J. Mater. Sci.*, 13(12), 2569-2576, **1978**.
10. Diré S., Babonneau F., Sanchez C., and Livage J., *J. Mater. Chem.*, 2(2), 239-244, **1992**.
11. Soraru G. D., Mercadini M., Maschio R. D., Taulelle F., *et al.*, *J. Am. Ceram. Soc.*, 76(10), 2595-2600, **1993**.
12. Wootton A. M., Rappensberger M., Lewis M. H., Kitchin S., *et al.*, *J. Non-Cryst. Solids*, 204(3), 217-227, **1996**.
13. Riedel R., Kienzle A., Dressler W., Ruwisch L., *et al.*, *Nature*, 382(6594), 796-798, **1996**.
14. Riedel R., Ruswisch L. M., An L., and Raj R., *J. Am. Ceram. Soc.*, 81(12), 3341-3344, **1998**.
15. Ionescu E., Linck C., Fasel C., Müller M., *et al.*, *J. Am. Ceram. Soc.*, 93(1), 241-250, **2010**.
16. Ionescu E., Papendorf B., Kleebe H.-J., Poli F., *et al.*, *J. Am. Ceram. Soc.*, 1782(6), 1774-1782, **2010**.
17. Ionescu E., Papendorf B., Kleebe H.-J., and Riedel R., *J. Am. Ceram. Soc.*, 1789, 1783-1789, **2010**.
18. Riedel R., Mera G., Hauser R., and Klonczynski A., *J. Ceram. Soc. Jpn.*, 114(1330), 425-444, **2006**.
19. Colombo P., Mera G., Riedel R., and Soraru G. D., *J. Am. Ceram. Soc.*, 93(7), 1805-1837, **2010**.
20. Kleebe H.-J. and Blum Y. D., *J. Eur. Ceram. Soc.*, 28(5), 1037-1042, **2008**.
21. Bodet R., Jia N., and Tressler R. E., *J. Eur. Ceram. Soc.*, 16(6), 653-664, **1996**.
22. Ellis R. B., U.S. Pat. No. 2,556,616, **1951**.
23. Smith C. F. and Crandall W. B., U.S. Pat. No. 3,378,431, **1968**.
24. Pantano C. G., Singh A. K., and Zhang H. X., *J. Sol-Gel Sci. Technol.*, 14(1), 7-25, **1999**.
25. Elmer T. H. and Meissner H. E., *J. Am. Ceram. Soc.*, 59(5-6), 206-209, **1976**.
26. Pampuch R., Ptak W. S., Jonas S., and Stoch J., The nature of Si-O-C phase(s) formed during oxidation of SiC, in *Proceeding of the 9th International Symposium on Reactivity of Solids*, Cracow, Poland, **1980**, Elsevier: New York.
27. Lipowitz J., Freeman H. A., Chen R. T., and Prack E. R., *Adv. Ceram. Mater.*, 2(2), 121-128, **1987**.
28. Lipowitz J., *Am. Ceram. Soc. Bull.*, 70(12), 1888-1894, **1991**.
29. Porte L. and Sartre A., *J. Mater. Sci.*, 24(1), 271-275, **1989**.
30. Saha A., Raj R., and Williamson D. L., *J. Am. Ceram. Soc.*, 89(7), 2188-2195, **2006**.
31. Widgeon S. J., Sen S., Mera G., Ionescu E., *et al.*, *Chem. Mater.*, 22(23), 6221-6228, **2010**.
32. Saha A. and Raj R., *J. Am. Ceram. Soc.*, 90(2), 578-583, **2007**.
33. Mera G., Navrotsky A., Sen S., Kleebe H. J., *et al.*, *J. Mater. Chem. A*, 1(12), 3826-3836, **2013**.

34. Monthieux M. and Delverdier O., *J. Eur. Ceram. Soc.*, 16(7), 721-737, **1996**.
35. Bréquel H., Parmentier J., Sorarù G. D., Schiffini L., *et al.*, *Nanostruct. Mater.*, 11(6), 721-731, **1999**.
36. Kleebe H.-J., Turquat C., and Sorarù G. D., *J. Am. Ceram. Soc.*, 84(5), 1073-1080, **2001**.
37. Papendorf B., Ionescu E., Kleebe H.-J., Linck C., *et al.*, *J. Am. Ceram. Soc.*, 96(1), 272-280, **2013**.
38. Bunde A. and Dieterich W., *J. Electroceram.*, 5(2), 81-92, **2000**.
39. Kirkpatrick S., *Rev. Mod. Phys.*, 45(4), 574-588, **1973**.
40. McLachlan D. S., Blaszkiewicz M., and Newnham R. E., *J. Am. Ceram. Soc.*, 73(8), 2187-2203, **1990**.
41. Essam J. W., *Rep. Prog. Phys.*, 43(7), 833-912, **1980**.
42. Bruggeman D. A. G., *Annalen der Physik*, 416(7), 636-664, **1935**.
43. Rozen J., Lopez R., Haglund R. F., and Feldman L. C., *Appl. Phys. Lett.*, 88(8), 081902, **2006**.
44. Batrouni G. G., Hansen A., and Larson B., *Phys. Rev. E*, 53(3), 2292-2297, **1996**.
45. Clerc J. P., Podolskiy V. A., and Sarychev A. K., *Eur. Phys. J. B*, 15(3), 507-516, **2000**.
46. Vionnet-Menot S., Grimaldi C., Maeder T., Strässler S., *et al.*, *Phys. Rev. B*, 71(6), 064201-064201, **2005**.
47. Balberg I. I., *Phys. Rev. Lett.*, 59(12), 1305-1308, **1987**.
48. Balberg I., *Phys. Rev. B*, 57(21), 13351-13354, **1998**.
49. Cordelair J. and Greil P., *J. Eur. Ceram. Soc.*, 20(12), 1947-1957, **2000**.
50. Martinez-Crespiera S., Ionescu E., Kleebe H. J., and Riedel R., *J. Eur. Ceram. Soc.*, 31(5), 913-919, **2011**.
51. Haluschka C., Engel C., and Riedel R., *J. Eur. Ceram. Soc.*, 20(9), 1365-1374, **2000**.
52. Kim K. J., Eom J.-H., Kim Y.-W., and Seo W.-S., *J. Eur. Ceram. Soc.*, 35(5), 1355-1360, **2015**.
53. Nguyen V. L., Zanella C., Bettotti P., and Sorarù G. D., *J. Am. Ceram. Soc.*, 97(8), 2525-2530, **2014**.
54. Chung D. D. L., *J. Mater. Sci.*, 37(8), 1475-1489, **2002**.
55. Jenkins G. M. and Kawamura K., Polymeric carbons - carbon fiber, glass and char, in **1976**, Cambridge University Press Cambridge. .
56. Li L., Zhu Z. H., Lu G. Q., Yan Z. F., *et al.*, *Appl. Catal. A Gen.*, 309(2), 201-209, **2006**.
57. Ergun S. and Alexander L. E., *Nature*, 195(4843), 765-767, **1962**.
58. Kakinoki J., Komura Y., and Ino T., *Acta Crystallogr.*, 13(3), 171-179, **1960**.
59. Jenkins G. M. and Kawamura K., *Nature*, 231(5299), 175-6, **1971**.
60. Ergun S., *Carbon*, 14(3), 139-150, **1976**.
61. Stenhouse B. J. and Grout P. J., *J. Non-Cryst. Solids*, 27(2), 247-256, **1978**.
62. Beeman D., Silverman J., Lynds R., and Anderson M. R., *Phys. Rev. B*, 30(2), 870-875, **1984**.
63. Robertson J. and O'Reilly E. P., *Phys. Rev. B*, 35(6), 2946-2957, **1987**.
64. Robertson J., *Adv. Phys.*, 35(4), 317-374, **1986**.
65. Jansen F., Machonkin M., Kaplan S., and Hark S., *J. Vac. Sci. Technol., A*, 3(3), 605-609, **1985**.
66. Dischler B., *Appl. Phys. Lett.*, 42(8), 636, **1983**.
67. Teo K. B. K., Ferrari A. C., Fanchini G., Rodil S. E., *et al.*, *Diamond Relat. Mater.*, 11(3-6), 1086-1090, **2002**.
68. Veerasamy V. S., Amaratunga G. A. J., Davis C. A., Timbs A. E., *et al.*, *J. Phys.: Condens. Matter*, 5(13), L169-L174, **1993**.
69. Neuville S., *QSci. Connect*, 8, 2-27, **2014**.
70. Jungnickel G., Frauenheim T., Porezag D., Blaudeck P., *et al.*, *Phys. Rev. B*, 50(10), 6709, **1994**.

71. Krüger A., *Neue Kohlenstoffmaterialien: Eine Einführung* 2007, Teubner Verlag / GWV Fachverlage GmbH: Wiesbaden.
72. Issi J.-P. and Charlier J.-C., *Electrical Transport Properties in Carbon Nanotubes*, in *The Science and Technology of Carbon Nanotubes*, 1999, Elsevier Science Ltd.: Oxford.
73. Moore A. W., *Physics and Chemistry of Carbon*, 1973, Dekker: New York
74. Clark C. D., Dean P. J., and Harris P. V., *Proc. R. Soc. Lon. Ser. A*, 277(1370), 312-315, 1964.
75. Short M. A. and Walker P. L., *Carbon*, 1(1), 3-9, 1963.
76. Noda T., Inagaki M., and Yamada S., *J. Non-Cryst. Solids*, 1, 285-302, 1969.
77. Franklin R. E., *Proc. R. Soc. Lon. Ser. A*, 209(1097), 196-&, 1951.
78. Morgan M., *Thin Solid Films*, 7(5), 313-323, 1971.
79. Schwan J., Ulrich S., Batori V., Ehrhardt H., *et al.*, *J. Appl. Phys.*, 80(1), 440-440, 1996.
80. Davis C. A., Silva S. R., Dunin-Borkowski R. E., Amaratunga G. A., *et al.*, *Phys. Rev. Lett.*, 75(23), 4258-4261, 1995.
81. Dasgupta D., Demichelis F., and Tagliaferro A., *Philos. Mag. B*, 63(6), 1255-1266, 1991.
82. Riedel E. and Janiak C., *Anorganische Chemie*, 2007, De Gruyter: Berlin.
83. Anderson P. W., *Phys. Rev.*, 109(5), 1492-1505, 1958.
84. Mott N. F., *Philos. Mag.*, 17(150), 1259-1268, 1968.
85. Cohen M. H., Fritzsche H., and Ovshinsky S. R., *Phys. Rev. Lett.*, 22(20), 1065-1068, 1969.
86. Davis E. A. and Mott N. F., *Philos. Mag.*, 22(179), 0903-0922, 1970.
87. Mott N. F. and Davis E. A., *Electronic processes in non-crystalline materials*, 1979, Clarendon Press: Oxford.
88. Liu C.-C., Walters A. B., and Vannice M. A., *Carbon*, 33(12), 1699-1708, 1995.
89. Dresselhaus M. S., Dresselhaus G., Sugihara K., Spain I. L., *et al.*, *Graphite Fibers and Filaments*, 1988, Springer-Verlag: Berlin, Heidelberg.
90. Klein C. A., *Rev. Mod. Phys.*, 34(1), 56-79, 1962.
91. Mrozowski S., *Phys. Rev.*, 85(4), 609-620, 1952.
92. Soule D. E. and McCluke J. W., *J. Phys. Chem. Solids*, 8, 29-35, 1959.
93. Galt J. K., Yager W. A., and Dail H. W., *Phys. Rev.*, 103(5), 1586-1587, 1956.
94. Cookson J. W., *Phys. Rev.*, 47(2), 194-195, 1935.
95. Eisler P., US 2,885,524, 1959.
96. Jackson P. G. S., GB 720,325, 1952.
97. Bardeen J. and Shockley W., *Phys. Rev.*, 80(1948), 72-80, 1950.
98. Smith C. S., *Phys. Rev.*, 919, 1954.
99. Mason W. P. and Thurston R. N., *J. Acous. Soc. Am.*, 29(10), 1096-1101, 1957.
100. Herring C. and Vogt E., *Phys. Rev.*, 101, 944-961, 1956.
101. Rowe A. C. H., *J. Mater. Res.*, 29(06), 731-744, 2014.
102. Baykan M. O., Thompson S. E., and Nishida T., *J. Appl. Phys.*, 108(9), 2010.
103. Chaparala M. V. and Shivaram B. S., *Piezoresistance of c-Si*, in *Properties of Crystalline Silicon*, 1998, The Institution of Electrical Engineers: London, United Kingdom.
104. Kanda Y., *IEEE Trans. Electron Devices*, 29(1), 64-70, 1982.
105. Barlian a. A., Park W.-T., Mallon J. R., Rastegar A. J., *et al.*, *Proceedings of the IEEE. Institute of Electrical and Electronics Engineers*, 97(3), 513-552, 2009.
106. Curtis G. J., Milne J. M., and Reynolds W. N., *Nature*, 220(5171), 1024-1025, 1968.
107. Peiner E., Tibrewala A., Bandorf R., Biehl S., *et al.*, *Sensors and Actuat. A-Phys.*, 130, 75-82, 2006.
108. Tibrewala A., Peiner E., Bandorf R., Biehl S., *et al.*, *J. Micromech. Microeng.*, 17(7), S77-S82, 2007.
109. Tibrewala a., Peiner E., Bandorf R., Biehl S., *et al.*, *Mater. Sci. Technol.*, 23(3), 362-367, 2007.
110. Wang Y., Yang R., Shi Z., Zhang L., *et al.*, *ACS Nano*, 5(5), 3645-50, 2011.

-
111. Hosseinzadegan H. and Todd C. Graphene has ultra high piezoresistive gauge factor, in IEEE 25th International Conference on Micro Electro Mechanical Systems (MEMS), **2012**,
 112. Lee Y., Bae S., Jang H., Jang S., *et al.*, *Nano Lett.*, 10(2), 490-3, **2010**.
 113. Bae S.-H., Lee Y., Sharma B. K., Lee H.-J., *et al.*, *Carbon*, 51, 236-242, **2013**.
 114. Huang M., Pascal T. A., Kim H., Goddard W. A., *et al.*, *Nano Lett.*, 11(3), 1241-6, **2011**.
 115. Pereira V. M., Castro Neto A. H., Liang H. Y., and Mahadevan L., *Phys. Rev. Lett.*, 105(15), 156603, **2010**.
 116. Ni Z. H., Yu T., Lu Y. H., Wang Y. Y., *et al.*, *ACS Nano*, 2(11), 2301-5, **2008**.
 117. Zhao J., He C., Yang R., Shi Z., *et al.*, *Appl. Phys. Lett.*, 101(6), 063112-063112, **2012**.
 118. Camargo P. H. C., Satyanarayana K. G., and Wypych F., *Materials Research*, 12(1), 1-39, **2009**.
 119. Liew L. A., Zhang W., An L., Shah S., *et al.*, *Am. Ceram. Soc. Bull.*, 80(5), 25-30, **2001**.
 120. Waku K., Hayashi H., and Kishimoto A., *J. Am. Ceram. Soc.*, 91(12), 4168-4170, **2008**.
 121. Waku K., Tagaya S., Hayashi H., and Kishimoto A., *J. Ceram. Soc. Jpn.*, 117(1367), 793-796, **2009**.
 122. Stauffer D. and Aharony A., *Introduction to percolation Theory*, **1994**, Taylor & Francis Group: Philadelphia.
 123. Kishimoto A., Takagawa Y., Teranishi T., and Hayashi H., *Mater. Lett.*, 65(14), 2197-2200, **2011**.
 124. Auerkari P., *Mechanical and physical properties of engineering alumina ceramics*, VTT Manufacturing Technology, **1996**, Technical Research Centre of Finland (VTT): Finland.
 125. Riedel R. and Chen I. W., *Ceramics Science and Technology, Materials and Properties*, **2010**, WILEY-VCH Verlag GmbH & Co. KGaA: Weinheim.
 126. Chen P.-W. and Chung D. D. L., *Smart Mater. Struct.*, 2(1), 22-30, **1993**.
 127. Shao-peng W., Lian-tong M., Zhong-he S., Dong-xing X., *et al.*, *Journal of Wuhan University of Technology-Mater. Sci. Ed.*, 17(4), 69-72, **2002**.
 128. Monfore G. E., *J. PCA Res. Dev. Lab.*, 10(2), 35-48, **1968**.
 129. Wen S. and Chung D. D. L., *Carbon*, 45(3), 505-513, **2007**.
 130. Pan P., Wu S., Xiao F., Pang L., *et al.*, *J. Intell. Mater. Syst. Struct.*, **2014**.
 131. Wen S. and Chung D. D. L., *Carbon*, 44(8), 1496-1502, **2006**.
 132. Xiao H., Li H., and Ou J., *J. Intell. Mater. Syst. Struct.*, 22(2), 191-200, **2011**.
 133. Fu X. L. and Chung D. D. L., *Cem. Concr. Res.*, 26(1), 15-20, **1996**.
 134. Chen P.-W. and Chung D. D. L., *J. Am. Ceram. Soc.*, 78(3), 816-818, **1995**.
 135. Wang S., Shui X., Fu X., and Chung D. D. L., *J. Mater. Sci.*, 33(15), 3875-3884, **1998**.
 136. Yao W., Chen B., and Wu K., *Chem. Phys*, 3, 3471-3471, **2001**.
 137. Wen S. and Chung D. D. L., *Cem. Concr. Res.*, 31(2), 297-301, **2001**.
 138. Reza F., Batson G. B., Yamamuro J. A., and Lee J. S., *J. Mater. Civ. Eng.*, 15(5), 476-483, **2003**.
 139. Chung D. D. L., *J. Intell. Mater. Syst. Struct.*, 13(9), 599-609, **2002**.
 140. Galao O., Baeza F. J., Zornoza E., and Garcés P., *Cem. Concr. Compos.*, 46, 90-98, **2014**.
 141. Howser R. N., Dhonde H. B., and Mo Y. L., *Smart Mater. Struct.*, 20(8), 085031-085031, **2011**.
 142. Gao D., Sturm M., and Mo Y. L., *Smart Mater. Struct.*, 20(4), 049501-049501, **2011**.
 143. Han B., Yu X., and Ou J., *J. Mater. Sci.*, 45(14), 3714-3719, **2010**.
 144. Li G. Y., Wang P. M., and Zhao X., *Cem. Concr. Compos.*, 29(5), 377-382, **2007**.
 145. Saafi M., *Nanotechnology*, 20(39), 395502-395502, **2009**.
 146. Yu X. and Kwon E., *Smart Mater. Struct.*, 18(5), 055010-055010, **2009**.
 147. Li G. Y., Wang P. M., and Zhao X., *Carbon*, 43(6), 1239-1245, **2005**.
 148. Materazzi A. L., Ubertini F., and D'Alessandro A., *Cem. Concr. Compos.*, 37, 2-11, **2013**.
 149. Li H., Xiao H., and Ou J., *Cem. Concr. Compos.*, 28(9), 824-828, **2006**.

150. Xiao H. G., Li H., and Ou J. P., *Sensor Actuat. A-Phys.*, 160(1-2), 87-93, **2010**.
151. Xiao H., Li H., and Ou J., *Sensor Actuat. A-Phys.*, 167(2), 581-587, **2011**.
152. Pang S. D., Gao H. J., Xu C., Quek S. T., *et al.* Strain and damage self-sensing cement composites with conductive graphene nanoplatelet, in Proceeding of SPIE, **2014**, San Diego
153. Ionescu E., Balan C., Kleebe H. J., Muller M. M., *et al.*, *J. Am. Ceram. Soc.*, 97(12), 3935-3942, **2014**.
154. Tyson B. M., Abu Al-Rub R. K., Yazdanbakhsh A., and Grasley Z., *J. Mater. Civ. Eng.*, 23(7), 1028-1035, **2011**.
155. Wen S. and Chung D. D. L., *Cem. Concr. Res.*, 36(10), 1879-1885, **2006**.
156. Chung D. D. L., *Adv Cem Res*, 16(4), 167-176, **2004**.
157. Han B. and Ou J., *Sensor Actuat. A-Phys.*, 138(2), 294-298, **2007**.
158. Ou J. and Han B., *J. Intell. Mater. Syst. Struct.*, 20(3), 329-336, **2008**.
159. Sáez de Ibarra Y., Gaitero J. J., Erkizia E., and Campillo I., *Phys. Stat. Sol. A*, 203(6), 1076-1081, **2006**.
160. Zhang L., Wang Y., Wei Y., Xu W., *et al.*, *J. Am. Ceram. Soc.*, 91(4), 1346-1349, **2008**.
161. Wang Y., Zhang L., Fan Y., Jiang D., *et al.*, *J. Mater. Sci.*, 44(11), 2814-2819, **2009**.
162. Wang Y., Zhang L., Xu W., Jiang T., *et al.*, *J. Am. Ceram. Soc.*, 91(12), 3971-3975, **2008**.
163. Wang Y., Ding J., Feng W., and An L., *J. Am. Ceram. Soc.*, 94(2), 359-362, **2011**.
164. Riedel R., Toma L., Janssen E., Nuffer J., *et al.*, *J. Am. Ceram. Soc.*, 93(4), 920-924, **2010**.
165. Toma L., Kleebe H.-J., Müller M. M., Janssen E., *et al.*, *J. Am. Ceram. Soc.*, 95(29722), 1056-1061., **2012**.
166. Terauds K., Sanchez-Jimenez P. E., Raj R., Vakifahmetoglu C., *et al.*, *J. Eur. Ceram. Soc.*, 30(11), 2203-2207, **2010**.
167. Sorarù G. D., D'Andrea G., Campostrini R., Babonneau F., *et al.*, *J. Am. Ceram. Soc.*, 78(2), 379-387, **1995**.
168. Rouxel T., Soraru G.-D., and Vicens J., *J. Am. Ceram. Soc.*, 84(5), 1052-1058, **2001**.
169. Ionescu E., Terzioglu C., Linck C., Kaspar J., *et al.*, *J. Am. Ceram. Soc.*, 96(6), 1899-1903, **2013**.
170. Kaspar J., Graczyk-Zajac M., Choudhury S., and Riedel R., *Electrochim. Acta*, 216, 196-202, **2016**.
171. Kaspar J., Graczyk-Zajac M., and Riedel R., *Solid State Ionics*, 225, 527-531, **2012**.
172. Renlund G. M., Prochazka S., and Doremus R. H., *J. Mater. Res.*, 6(12), 2723-2734, **1991**.
173. Sorarù G. D., *J. Sol-Gel Sci. Technol.*, 2(1-3), 843-848, **1994**.
174. Martínez-Crespiera S., Ionescu E., Kleebe H.-J., and Riedel R., *J. Eur. Ceram. Soc.*, 31(5), 913-919, **2011**.
175. Betz W., Shollenberger D., Keeler M., Buchanan M., *et al.* High Surface Area Graphitized Mesoporous Carbons. 2007; Available from: <http://www.sigmaaldrich.com/technical-documents/articles/materials-science/nanomaterials/graphitized-mesoporous-carbon.html>.
176. Galusek D., Riley F. L., and Riedel R., *J. Am. Ceram. Soc.*, 84(5), 1164-1166, **2001**.
177. Rino J. P., Ebbsjö I., Branicio P. S., Kalia R. K., *et al.*, *Phys. Rev. B*, 70(4), 045207, **2004**.
178. Filsinger D. H. and Bourrie D. B., *J. Am. Ceram. Soc.*, 73(6), 1726-1732, **1990**.
179. Biernacki J. J. and Wotzak G. P., *J. Am. Ceram. Soc.*, 72(1), 122-129, **1989**.
180. Xue K., Niu L.-S., and Shi H.-J., Mechanical Properties of Amorphous Silicon Carbide, in *Silicon Carbide - Materials, Processing and Applications in Electronic Devices*, **2011**, InTech
181. Esfahanian M., Oberacker R., Fett T., and Hoffmann M. J., *J. Am. Ceram. Soc.*, 91(11), 3803-3805, **2008**.
182. Plachký T., Lenčేశ Z., Hric L., Šajgalík P., *et al.*, *J. Eur. Ceram. Soc.*, 30(3), 759-767, **2010**.

-
183. Kleebe H.-J., Gregori G., Babonneau F., Blum Y. D., *et al.*, *Z. Metallk.*, 97(6), 699-709, **2006**.
 184. Mazo M. a., Tamayo a., Rubio F., Soriano D., *et al.*, *J. Non-Cryst. Solids*, 391, 23-31, **2014**.
 185. Bois L., Maquet J., Babonneau F., and Bahloul D., *Chem. Mater.*, 7(5), 975-981, **1995**.
 186. Sousa B. F., Yoshida I. V. P., Ferrari J. L., and Schiavon M. A., *J. Mater. Sci.*, 48(5), 1911-1919, **2012**.
 187. Önnby C. and Pantano C. G., *J. Vac. Sci. Technol., A*, 15(3), 1597-1602, **1997**.
 188. Sorarù G. D., D'Andrea G., and Glisenti A., *Mater. Lett.*, 27(1-2), 1-5, **1996**.
 189. Stabler C., Roth F., Narisawa M., Schliephake D., *et al.*, *J. Eur. Ceram. Soc.*, 36(15), 3747-3753, **2016**.
 190. Suyal N., Hoebbel D., Mennig M., and Schmidt H., *J. Mater. Chem.*, 9(12), 3061-3067, **1999**.
 191. Lu K., Erb D., and Liu M., *J. Mater. Chem. C*, 4(9), 1829-1837, **2016**.
 192. Brewer C. M., Bujalski D. R., Parent V. E., Su K., *et al.*, *J. Sol-Gel Sci. Technol.*, 14(1), 49-68, **1999**.
 193. Renlund G. M., Prochazka S., and Doremus R. H., *J. Mater. Res.*, 6(12), 2716-2722, **1991**.
 194. Tamor M. a. and Vassell W. C., *J. Appl. Phys.*, 76(6), 3823-3823, **1994**.
 195. Tessonier J.-P., Rosenthal D., Hansen T. W., Hess C., *et al.*, *Carbon*, 47(7), 1779-1798, **2009**.
 196. Dresselhaus M. S., Dresselhaus G., Jorio A., Souza Filho A. G., *et al.*, *Carbon*, 40(12), 2043-2061, **2002**.
 197. Dresselhaus M. S., Dresselhaus G., Saito R., and Jorio A., *Phys. Rep.*, 409(2), 47-99, **2005**.
 198. Malard L. M., Pimenta M. A., Dresselhaus G., and Dresselhaus M. S., *Phys. Rep.*, 473(5-6), 51-87, **2009**.
 199. Ferrari A. C. and Basko D. M., *Nature nanotechnology*, 8(4), 235-46, **2013**.
 200. Ferrari A. C., *Solid State Commun.*, 143(1-2), 47-57, **2007**.
 201. Tuinstra F. and Koenig J. L., *J. Chem. Phys.*, 53(3), 1126-1126, **1970**.
 202. Ferrari A. C., Rodil S. E., Robertson J., and Milne W. I., *Diamond Relat. Mater.*, 11(3-6), 994-999, **2002**.
 203. Irmer G. and Dorner-Reisel A., *Adv. Eng. Mater.*, 7(8), 694-705, **2005**.
 204. Ferrari A. C. and Robertson J., *Philos. Trans. A Math. Phys. Eng. Sci.*, 362(1824), 2477-512, **2004**.
 205. Baranov A. V., Bekhterev A. N., Bobovich Y. S., and Petrov V. I., *Opt. Spectrosc.*, 62(5), 612-616, **1987**.
 206. Thomsen C. and Reich S., *Phys. Rev. Lett.*, 85(24), 5214-7, **2000**.
 207. Vidano R. and Fischbach D. B., *J. Am. Ceram. Soc.*, 61(1-2), 13-17, **1978**.
 208. Nemanich R. J. and Solin S. A., *Phys. Rev. B*, 20(2), 392-401, **1979**.
 209. Ferrari A. C., Meyer J. C., Scardaci V., Casiraghi C., *et al.*, *Phys. Rev. Lett.*, 97(18), 187401, **2006**.
 210. Tuinstra F. and Koenig J. L., *J. Chem. Phys.*, 53(3), 1126-1130, **1970**.
 211. Knight D. S. and White W. B., *J. Mater. Res.*, 4(2), 385-393, **1989**.
 212. Matthews M. J., Pimenta M. A., Dresselhaus G., Dresselhaus M. S., *et al.*, *Phys. Rev. B*, 59(10), R6585-R6588, **1999**.
 213. Ferrari A. C. and Robertson J., *Phys. Rev. B*, 61(20), 14095-14107, **2000**.
 214. Larouche N. and Stansfield B. L., *Carbon*, 48(3), 620-629, **2010**.
 215. Cançado L. G., Takai K., Enoki T., Endo M., *et al.*, *Appl. Phys. Lett.*, 88(16), 163106, **2006**.
 216. Chu P. K. and Li L., *Mater. Chem. Phys.*, 96(2-3), 253-277, **2006**.
 217. Gilkes K. W. R., Sands H. S., Batchelder D. N., Robertson J., *et al.*, *Appl. Phys. Lett.*, 70(15), 1980-1980, **1997**.

218. Castiglioni C., Tommasini M., and Zerbi G., *Philos. Trans. A Math. Phys. Eng. Sci.*, 362(1824), 2425-59, **2004**.
219. Pimenta M. A., Dresselhaus G., Dresselhaus M. S., Cancado L. G., *et al.*, *Phys. Chem. Chem. Phys.*, 9(11), 1276-91, **2007**.
220. Bonijoly M., Oberlin M., and Oberlin A., *Int J Coal Geol*, 1(4), 283-312, **1982**.
221. Cuesta A., Dhamelincourt P., Laureyns J., Martínez-Alonso A., *et al.*, *Carbon*, 32(8), 1523-1532, **1994**.
222. Cancado L. G., Jorio A., Ferreira E. H., Stavale F., *et al.*, *Nano Lett.*, 11(8), 3190-6, **2011**.
223. Lucchese M. M., Stavale F., Ferreira E. H. M., Vilani C., *et al.*, *Carbon*, 48(5), 1592-1597, **2010**.
224. Eckmann A., Felten A., Mishchenko A., Britnell L., *et al.*, *Nano Lett.*, 12(8), 3925-30, **2012**.
225. Hahn J. R. and Kang H., *Phys. Rev. B*, 60(8), 6007-6017, **1999**.
226. De Fonton S., Oberlin A., and Inagaki M., *J. Mater. Sci.*, 15(4), 909-917, **1980**.
227. Haluschka C., Kleebe H.-J., Franke R., and Riedel R., *J. Eur. Ceram. Soc.*, 20(9), 1355-1364, **2000**.
228. Ma B., Wang Y., Wang K., Li X., *et al.*, *Acta Mater.*, 89, 215-224, **2015**.
229. Yasunori I., Mayo S., Shunsuke K., Masaaki K., *et al.*, *Bull. Chem. Soc. Jpn.*, 86(1), 45-50, **2013**.
230. Cattin C. and Hubert P., *ACS Appl. Mater. Interfaces*, 6(3), 1804-11, **2014**.
231. Li J., Ma P. C., Chow W. S., To C. K., *et al.*, *Adv. Funct. Mater.*, 17(16), 3207-3215, **2007**.
232. Mathew M., Schilling T., and Oettel M., *Phys. Rev. E*, 85, 061407, **2012**.
233. Garcia P. F., Suna A., and Childers W. D., *J. Appl. Phys.*, 54(10), 6002-6002, **1983**.
234. Elliot S. R., *Physics of amorphous materials*, **1984**, John Wiley & sons Inc.: New York
235. Engel C., *Elektrische Eigenschaften gefüllter Pyrolyse-Keramiken im System Si-O-C.*, **2000**, Shaker Verlag: Aachen.
236. Robertson J., *Surf. Coat. Technol.*, 50(3), 185-203, **1992**.
237. Kim K. J., Eom J.-H., Koh T. Y., Kim Y.-W., *et al.*, *J. Eur. Ceram. Soc.*, 36(11), 2705-2711, **2016**.
238. Berezkin V. I., Kholodkevich S. V., and Konstantinov P. P., *Phys. Solid State*, 39(10), 1590-1593, **1997**.
239. Mrozowski S. and Chaberski A., *Phys. Rev.*, 104(1), 74-83, **1956**.
240. Klein C. A. and Straub W. D., *Phys. Rev.*, 123(5), 1581-1583, **1961**.
241. Baker D. F. and Bragg R. H., *J. Non-Cryst. Solids*, 58(1), 57-69, **1983**.
242. Kinchin G. H., *Proc. R. Soc. Lon. Ser. A*, 217(1128), 9-26, **1953**.
243. Matsuda K., *J. Comput. Electron.*, 3(3-4), 273-276, **2004**.
244. Ohmura Y., *J. Phys. Soc. Jpn.*, 62(10), 3615-3620, **1993**.
245. Böttger H. and Bryksin V. V., *Hopping conduction in solids*, **1985**, Berlin Verlag: Berlin.
246. Carmona F., Canet R., and Delhaes P., *J. Appl. Phys.*, 61(7), 2550-2550, **1987**.
247. Li H., Xiao H., and Ou J., *Compos. Sci. Technol.*, 68(9), 2114-2119, **2008**.
248. Balberg I., Azulay D., Goldstein Y., Jedrzejewski J., *et al.*, *Eur. Phys. J. B*, 86(10), **2013**.
249. Hu N., Karube Y., Yan C., Masuda Z., *et al.*, *Acta Mater.*, 56(13), 2929-2936, **2008**.
250. Simmons J. G., *J. Appl. Phys.*, 34(6), 1793-1793, **1963**.
251. McGraw D., *IJRRAS*, 25(3), 10-15, **2015**.
252. Mattox D. M., Gurkovich S. R., Olenick J. A., and Mason K. M., *Low Dielectric Constant, Alumina-Compatible, Co-Fired Multilayer Substrate*, in *Cofire Technology: Ceramic Engineering and Science Proceedings*, **1988**, John Wiley & Sons: Hoboken.
253. Siegal M. P., Friedmann T. A., and Sullivan J. P., *Diamond and diamond-like carbon films for advanced electronic applications*, **1996**, University of North Texas Libraries: New Mexico.
254. Moysan C., Riedel R., Harshe R., Rouxel T., *et al.*, *J. Eur. Ceram. Soc.*, 27(1), 397-403, **2007**.

-
-
255. Grimaldi C., Maeder T., Ryser P., and Strassler S., *J. Phys. D: Appl. Phys.*, 36(11), 1341-1348, **2003**.
 256. McClarty M. M., Jegenyés N., Gaudet M., Toccafondi C., *et al.*, *Appl. Phys. Lett.*, 109(2), 023102, **2016**.
 257. Turner R. C., Fuierer P. A., Newnham R. E., and Shrout T. R., *Appl Acoust*, 41(4), 299-324, **1994**.
 258. Jiang X., Kim K., Zhang S., Johnson J., *et al.*, *Sensors* 14(1), 144-69, **2014**.
 259. Damjanovic D., *Curr. Opin. Solid State Mater. Sci.*, 3(5), 469-473, **1998**.

Acknowledgment

I would like to express special thanks to Prof. Dr. Ralf Riedel for offering me the possibility to obtain a doctorate on the field of polymer-derived-ceramics and his continuous support during the thesis.

Prof. Dr. Roland Werthschützky is acknowledged for the second survey of this thesis and his tremendous support during the Rolls & Royce project.

I also want to express a special thanks to two very important persons who supported me in any manner during the thesis and had been crucial for the success of this work. It was a real pleasure to work and learn from PD Emanuel Ionescu and apl. Prof. Norbert Nicoloso as they always helped me with inspiring and open discussions. Frankly speaking, I do not have words to tell you how much I have learned from you guys. Thank you!

I want to address a very big thank-you to all DF group members who contributed to this work in many different ways and for the very friendly atmosphere. In particular, I would like to thank Dipl.-Ing. Christiana Stabler and Dipl.-Ing. Dragoljub Vrankovic for their helpful support in the lab and the many valuable suggestions and discussions. I also would like to thank Dipl.-Ing. Claudia Fasel for TGA measurements and especially for keeping all the devices and laboratories running.

I would like to thank Dipl.-Ing. Linbo Tang from the Electromechanical Department (EMK) for the productive and constructive cooperation during the project with Rolls & Royce. Thereby, I would like to thank Jens Kesting, Peter Hackenberg and Rudolf Lück from Rolls & Royce for financing and for allowing me a glimpse into the daily work routine of a recognized company.

I thank Dr. Benjamin Balke at the University of Mainz for the Hall measurements and for the helpful discussions.

Last but not the least, I am grateful to my parents, grandparents and my brother who made me what I am today and supported me in all walks of life. I cannot express how grateful I am. Thank you!

Finally, and most importantly, I would like to acknowledge the support of my better-half Eva who has been supportive in every way possible, and still manages to make me feel like I am newly in love. *Let's grow old together ...*

List of Abbreviations

BSU	Basic structure units
CB	Carbon black
CFO	Cohen-Fritzsche-Ovshinsky model
CNF	Carbon nanofibers
CNT	Carbon nanotubes
C-S-H	Calcium silicate hydrate
CVD	Chemical vapor deposition
DLC	Diamond-like carbon
DM	Davis-Mott model
EDX	Energy-dispersive X-ray spectroscopy
EMK	Electromechanical department at the TU Darmstadt
EMT	Effective media theory
EPR	Electron paramagnetic resonance
FEM	Finite element method
FWHM	Full width half maximum
GEM	General effective media theory
GNP	Graphene nanoplatelets
Gr.	Graphite
HTT	High temperature treatment
MEMS	Microelectromechanical systems
NNH	Nearest neighbour hopping
PAH	Polycyclic aromatic hydrocarbons
PDCs	Polymer derived ceramics
PT	Percolation theory
PZR	Piezoresistive effect
RPECVD	Remote plasma enhanced chemical vapor deposition

RT	Room temperature
SEM	Scanning electron microscope
SiOC	Silicon oxycarbide
SPS	Spark plasma sintering
TEM	Transmission Electron Microscope
TEMS	Triethoxymethylsilane
TEOS	Tetraethyl orthosilicate
TEVS	Triethoxyvinylsilane
TGA	Thermogravimetric analysis
UV	Ultraviolet
VIS	Visible
VRH	Variable range hopping
XPS	X-ray Photoelectron Spectroscopy
XRD	X-ray Diffraction

List of Symbols

ν	Frequency	(Hz)
ϕ	Volume fraction	(%)
ϕ_c	Volume fraction of carbon	(%)
$\phi_{\text{cri.}}$	Critical volume fraction	(%)
\vec{E}	Electric field vector	(V·m ⁻¹)
\vec{j}	Current vector	(A·mm ⁻²)
μ	Charge carrier mobility	(cm ² /Vs)
A	Area	(m ³)
C_λ	Wavelength dependent coefficient	(nm ⁻¹)
e	Elementary charge	(C)
E	Youngs modulus	(GPa)
E_a	Activation energy	(eV)
E_F	Fermi energy	(eV)
E_g	Band gap	(eV)
F	Force	(N)
h	Planck constant	(J·s)
h_0	Initial height	(m)
l_c	Interplanar distance	(nm)
J	Tunnel current density	(A·mm ⁻²)
k_b	Boltzmann constant	(eV·K ⁻¹)
k_F	Fermi wavelength	(nm)
l_0	Initial length	(m)
L_a	Lateral size	(nm)
L_D	Defect distance	(nm)
m^*	Effective mass	(g)
N	Charge carrier density	(cm ³)

P	Pressure	(MPa)
R_0	Initial bulk resistance	(Ω)
R_H	Hall coefficient	(m^3/C)
s	Potential barrier width	(nm)
t	Critical exponent	(-)
T	Temperature	($^{\circ}C$)
U	Voltage	(U)
W	Hopping activation energy	(eV)
w_0	Initial width	(m)
α	Localization length	(nm)
α_T	Thermal coefficient of resistance	(K^{-1})
ε	Strain	(-)
λ	Wavelength	(nm)
π_{ij}	Piezoresistive coefficients	(-)
ρ	Density	(g/cm^3)
ρ	Resistivity	(Ω/cm^2)
σ	Conductivity	(Ω/cm^2) ⁻¹
τ	Relaxation time	(s)
φ	Barrier height	(V)
Φ	Porosity	(%)

List of Figures

Figure 2.1: Simplified structure of silicon based polymer. By substituting the polymeric backbone atom X with C, O or N different types of ceramics structures can be achieved upon pyrolysis [19].4	4
Figure 2.2: Schematic depiction of an amorphous SiOC/C network heat treated at $T < 1000\text{ }^{\circ}\text{C}$ [24].5	5
Figure 2.3: Two proposed models of the nanostructure in polymer-derived SiOC. a) Silica nanodomains are warped by layers of graphene [32]. b) O_2 -rich SiOC domains form a continuous network and encapsulate the precipitated carbon [33]......6	6
Figure 2.4: Calculated insulator-conductor transition for different values of t and ϕ_{cri} . [49].9	9
Figure 2.5: Schematic depiction of the carbon allotropes hierarchy and their corresponding conductive class. 11	11
Figure 2.6: Schematic structural model of glassy carbon by Jenkins and Kawamura [59]...... 12	12
Figure 2.7: Schematic depiction of the band structure going from metals to insulators [82]. 15	15
Figure 2.8: DM-Model, CFO-Model and a possible structure of an amorphous system. 16	16
Figure 2.9: Schematic energy-band diagram for turbostratic and graphitic carbon [90]. 19	19
Figure 2.10: Constant energy surfaces in momentum space for n-doped silicon a) Surface of the six constant energy ellipsoids in the conduction band b) The effect of stress on the valley energy depicted by asymmetric dilation or constriction of the ellipsoids, respectively [102]. 21	21
Figure 3.1: Schematic depiction of the sol-gel precursors and the preceramic polymers. 31	31
Figure 3.2: Schematic depiction of two different samples geometries with a) the rectangular and b) the cylindrical shape used during the electrical investigations. 35	35
Figure 3.3: Developed experimental setup to determine the piezoresistive effect. The enlarged area represents the measurement chamber. 36	36
Figure 4.1: Schematically depiction of the sol-gel process and the derived organosiloxane network. 38	38
Figure 4.2: Si-O-C phase diagram including the compositions of silicon oxycarbide ceramics pyrolysed at $T = 1600\text{ }^{\circ}\text{C}$. The green dots represent synthesised compositions, while the red dots are derived from commercially available preceramic polymers..... 39	39
Figure 4.3: Evolution of SiO_2 and SiC as a function of the segregated carbon phase. 41	41
Figure 4.4: Density and residual open porosity of C-11 and C-17 heat treated at various temperatures. 42	42
Figure 4.5: SEM images of different SiOC/C samples prepared at $T = 1600\text{ }^{\circ}\text{C}$ under $P = 50\text{ MPa}$ 43	43
Figure 4.6: XRD patterns of C-17, C-11 and C-1 synthesized at temperatures between $1200 - 1800\text{ }^{\circ}\text{C}$... 44	44
Figure 4.7: A schematic of the five mixed silicon tetrahedra units found in silicon oxycarbide materials.46	46
Figure 4.8: Experimental Si(2p) spectrum for C-1, C-11 and C-17 all prepared at $T = 1600\text{ }^{\circ}\text{C}$ 47	47
Figure 4.9: Experimental C(1s) spectrum for C-1, C-11 and C-17 all prepared at $T = 1600\text{ }^{\circ}\text{C}$ 47	47
Figure 4.10: Experimental O(1s) spectrum for C-1, C-11 and C-17 all prepared at $T = 1600\text{ }^{\circ}\text{C}$ 48	48
Figure 4.11: The course of the electrical resistivity of C-17 heated up to $T = 500\text{ }^{\circ}\text{C}$ in air..... 49	49
Figure 4.12: TGA-FTIR spectrum of a) C-11 and b) C-17 in the temperature range of $25 - 1000\text{ }^{\circ}\text{C}$ 50	50
Figure 4.13: Carbon vibration in the G and D modes. The G vibration is not strictly related to aromatic structures and can also be found in polyacetylenes. 52	52
Figure 4.14: Schematically depiction of the lateral crystal size L_a 53	53
Figure 4.15: Comparison of the UV Raman spectra of C-1 and C-11 sample prepared at $T = 1000\text{ }^{\circ}\text{C}$ 54	54

Figure 4.16: Comparison of the UV Raman spectra of C-1 and C-11 sample prepared at $T = 1400\text{ }^{\circ}\text{C}$	55
Figure 4.17: UV Raman spectra of sample C-11 prepared at $1600\text{ }^{\circ}\text{C}$. The inset shows the second order UV Raman spectrum.....	56
Figure 4.18: Evolution of the Raman spectrum obtained at $\lambda = 514\text{ nm}$ for C-11 samples heat-treated at different temperatures ($1000 < T < 1800\text{ }^{\circ}\text{C}$).	57
Figure 4.19: Progressive change of the FWHM of the D and G band upon thermal treatment.	59
Figure 4.20: Dependency between the lateral crystal size L_a and the thermal treatment. The open data points in the inset represent the work of Ref. [215].....	60
Figure 4.21: Plot of the lateral crystal size L_a as a function of the amount of carbon.....	61
Figure 4.22: Evolution of the average distance between defects L_D within the carbon of SiOC/C synthesized at different temperatures. The empty dots represent Ar^+ ion bombarded graphene [223].....	62
Figure 4.23: I_D/I_G versus ratio I_D/I_G . Data from literature is represented by open symbols [224].....	63
Figure 4.24: Schematic depiction of a nano-crystalline cluster taken from Ref. [226].	64
Figure 4.25: Effect of heat-treatment temperature on the RT-conductivity of C-11, C-17. Literature data is taken from Ref. [53, 228].	65
Figure 4.26: Schematic depiction of the carbon distribution within SiOC/C.....	66
Figure 4.27: The electrical conductivity of SiOC/C as a function of the sp^2 carbon for three different temperature series. Literature values are added for the sake of comparison.	67
Figure 4.28: Electrical conductivity as a function of sp^2 carbon concentration. The solid line represents the fit from Equation 2.9. The upper dashed line represents the universal behavior with a slope of $t = 2$	68
Figure 4.29: Schematically depiction of the electronic transport of a) electrons and b) holes within the localized states.....	69
Figure 4.30: Electrical conductivity of C-11 as a function of temperature.	70
Figure 4.31: E_a of the different conduction mechanism in SiOC/C derived from dc conductivity in the temperature regime of $200 \leq T \leq 800\text{ }^{\circ}\text{C}$ as a function of the sp^2 carbon.	70
Figure 4.32: Schematically depiction of the shallow traps within the conjugated π -system.	71
Figure 4.33: Hall density and mobility of SiOC/C prepared at $T = 1600\text{ }^{\circ}\text{C}$. SiOC/C literature values and calculated densities are shown for comparison.	73
Figure 4.34: Variation of the Hall coefficient with carbon concentration for SiOC/C samples synthesized at $T = 1600\text{ }^{\circ}\text{C}$. Glassy carbon is depicted as reference [237].....	73
Figure 4.35: Schematic depiction of the developed setups, a) bending beam and b) measurement chamber.	75
Figure 4.36: FEM simulation of the present stresses within the bending beam and the SiOC/C sample.	76
Figure 4.37: Piezoresistive measurement of a SiOC/C sample using the developed stress pattern.	76
Figure 4.38: Determination of the GF value by plotting the relative resistance change against the strain.	77
Figure 4.39: Correlation of Raman and piezoresistivity data for SiOC/C. The dashed area represents literature values for GF and Raman linewidth of highly ordered carbon (HOPG, graphene).	78
Figure 4.40: Gauge factor as a function of the sp^2 content in carbon allotropes [107, 108, 112].....	79
Figure 4.41: Course of the piezoresistive behavior of SiOC/C as a function of the carbon content.	79

Figure 4.42: The average defect distance L_D plotted against the carbon concentration.....	80
Figure 4.43: Natural logarithm of the conductivity as a function of $V^{-1/3}$	80
Figure 4.44: GF (at the respective ϕ_{cri}) of inorganic nano-composites, with $\square = [140]$, $\Delta = [120, 121]$, $\triangleright = [46]$, $\nabla = [149, 151]$ and $\circ = [108, 109]$	82
Figure 4.45: Arrhenius plot of GF for a C-11 sample within the range of $25 < T < 400$ °C.	83
Figure 4.46: Arrhenius plot of GF of a C-11 sample in the range of $1000 < T < 1200$ °C. Literature values (empty and filled circles) of SiOCN/C ($\phi_c = 8.8$ vol.%) are presented for comparison [166]..	83
Figure 4.47: GF values of the two temperature regimes. Literature values (empty and filled circles) of SiOCN/C ($\phi_c = 8.8$ vol.%) are presented for comparison [165].	84
Figure 4.48: Schematic depiction of the local strain at the sample/electrode interface during loading..	84
Figure 4.49: Gauge factor as a function of the applied pressure of a C-11 sample.....	86
Figure 4.50: Schematic depiction of the piezoresistive SiOC/C sensor prototype for RT measurements.	87
Figure 4.51: Experimental setup of the planetary gear along with the two compared sensors.	88
Figure 4.52: Natural frequency of the ring gear measured at 88 and 120 rpm using the SiOC/C prototype and a commercially available PIC 255 sensor.	89

List of Tables

Table 2.1: Comparison of the RT conductivity, the band gap, the lateral crystal size L_a and the interplane distance of the different carbon allotropes.	14
Table 2.2: Resistivity and piezoresistive coefficients for p- and n-doped Si and Ge [8].....	22
Table 2.3: Piezoresistive behavior of Al_2O_3 and MgO reinforced with carbon (at RT).....	25
Table 2.4: Piezoresistive behavior of carbon-reinforced cement composites at RT.	27
Table 2.5: Piezoresistive behavior of polymer-derived-ceramics.	28
Table 3.1: Ratio of the sol-gel derived polymers and the commercially available preceramic polymers with the corresponding ceramic yield after pyrolysis.	30
Table 4.1: Elemental analysis of selected samples after pyrolysis at $T = 1600$ °C for 15 min in Argon.	40
Table 4.2: Elemental analysis of sample C-11 pyrolysed at temperatures between $T = 1000 - 1800$ °C. .	43
Table 4.3: Summary of the features present in the first-order Raman spectrum of C-11.	58

Curriculum Vitae

Personal data:

Name: Felix Rosenburg né Roth
Date of birth: 2. Juli 1984
Nationality: German

Education:

since 09.2015 Cooperation with Rolls & Royce Deutschland Ltd & Co KG
Project: LuFo V - OLIAS

since 05.2013 **Technical University of Darmstadt**
PhD candidate in materials science

04.2005 - 03.2013 **Technical University of Darmstadt**
Graduation: Dipl.-Ing. of Chemistry

2001 - 2004 Technical high school Mainz
Graduation: A level

1995 - 2001 High school Mainz-Gonsenheim

1991 - 1995 Elementary school Mainz-Finthen

Qualifications:

01.2014 - 03.2016 Hochschuldidaktische Arbeitsstelle Darmstadt (HDA)
Graduation: certified university docent

07.2004 - 03.2005 German Red Cross
District chapter Mainz-Bingen
Graduation: Paramedic